Design, Fabrication, and Flight Testing of a Balloon-Launched, High-Altitude Payload Retrieval UAV

A thesis submitted in fulfilment of the requirements

for the degree of Master's of Technology

by

Karan Kumar Tiwari

22101028

DEPARTMENT OF AEROSPACE ENGINEERING

INDIAN INSTITUTE OF TECHNOLOGY KANPUR

November 2024

Certificate

It is certified that the work contained in this thesis entitled **"Design, Fabrication, and Flight Testing of a Balloon-Launched, High-Altitude Payload Retrieval UAV "** by **Karan Kumar Tiwari** has been carried out under my supervision and that it has not been submitted elsewhere for a degree.

Dr. Abhishek

Professor

Department of Aerospace Engineering

Indian Institute of Technology Kanpur

November 2024

Declaration

This is to certify that the thesis titled **"Design, Fabrication, and Flight Testing of a Balloon-Launched, High-Altitude Payload Retrieval UAV "** has been authored by me. It presents the research conducted by me under the supervision of **Dr. Abhishek**.

To the best of my knowledge, it is an original work, both in terms of research content and narrative, and has not been submitted elsewhere, in part or in full, for a degree. Further, due credit has been attributed to the relevant state-of-the-art and collaborations with appropriate citations and acknowledgments, in line with established norms and practices.

Karan Kumar Tiwari

Roll No. 22101028

Department of Aerospace Engineering

Indian Institute of Technology Kanpur

November 2024

Abstract

Name of the student: **Karan Kumar Tiwari** Roll No: **22101028**

Thesis supervisors: **Dr. Abhishek**

Degree for which submitted: **Master of Technology**

Department: **Department of Aerospace Engineering**

Thesis title: **Design, Fabrication, and Flight Testing of a Balloon-Launched, High-Altitude Payload Retrieval UAV**

Month and year of thesis submission: **November 2024**

This research addresses the design, development, and testing of a high-altitude, balloon-launched unmanned aerial vehicle (UAV) capable of autonomously retrieving meteorological sensors upon release or in the event of a balloon burst at high altitudes. The primary objective is to create a proof-of-concept (POC) UAV that ascends with a balloon and navigates back to a designated home location after release, utilizing onboard autopilot and navigation systems. The UAV utilizes both powered propulsion from batteries and stored potential energy for efficient flight, particularly during retrieval in the challenging environmental conditions typical of India.

The development of the UAV involved a comprehensive set of methodologies, including maximum takeoff weight (MTOW) estimation, constraint-based sizing, airfoil selection, wing design, tail and fuselage design, and structural analysis. The fabrication process utilized advanced composite materials and manufacturing techniques, such as vacuum bagging, to enhance structural strength while minimizing weight. Tailored modifications to the flight controller were implemented to ensure reliable autonomous navigation.

Testing of the UAV included both standalone performance evaluations to validate its characteristics and successful low-altitude flight trials, where the UAV was lifted by a hexacopter and dropped from an altitude to simulate a high-altitude retrieval mission. Key challenges addressed in this research include weight reduction, payload retrieval, and cost-effectiveness in design, resulting in a powered glider configuration that optimizes battery use while achieving a higher range of retrieval in adverse weather conditions. Initial testing demonstrated the UAV's potential for real-world applications, paving the way for advanced UAV platforms adaptable to diverse global weather stations. This study contributes a scalable, energy-efficient approach to high-altitude meteorological data retrieval.

Acknowledgements

I would like to express my sincere gratitude to several individuals who have been instrumental in completing this research.

First and foremost, I am deeply indebted to my professor, Dr. Abhishek, for his unwavering support and guidance throughout my academic journey at IIT Kanpur. Dr. Abhishek has been an exceptional mentor, offering invaluable advice not only in my research but also in personal matters, always taking the time to listen and guide me with his wealth of experience. His mentorship has been a cornerstone of my success, and I am profoundly grateful for his constant support.

My heartfelt thanks also go to Vishnu Teja, a dear friend and collaborator, who contributed significantly to the control and navigation aspects of this project. His expertise in writing custom flight modes and firmware for the UAV's navigation and control systems was indispensable.

Special acknowledgment goes to the Helicopter Lab, notably the Composite Manufacturing Lab, for assisting with fabricating multiple prototypes under tight deadlines. I am also grateful to the Assembly Room team for their help in integrating, assembling, and testing the UAV, which was crucial for meeting project milestones.

I am forever grateful to my family, especially my parents, for their unwavering support throughout my academic journey and life. I dedicate this work to them in appreciation of their encouragement and sacrifices.

Finally, I would like to thank Mr. Prameet Tiwari, Mr. Nitesh Sachan, Mr. Pranab, and many others in the lab who contributed to creating a lively work environment and assisted me during the rigorous fabrication and testing phases. Their camaraderie and help were invaluable to this journey, and I am genuinely thankful for their support.

Contents

Acknowledgements **vi**

List of Figures **x**

List of Tables **xii**

1 Introduction **1**
1.1 Background 1
1.2 Motivation 1
1.3 Problem Statement 2
1.4 Organization of the Thesis 3

2 Literature Review **5**
2.1 High-altitude Meteorological Research and Balloon Systems 5
2.2 UAV's in High Altitude Payload Retrieval 6
2.3 Technical Considerations for High-altitude Payload Retrieval UAVs 7
2.3.1 Navigation and Control Systems 7
2.3.2 Structural and Material Considerations 8
2.3.3 Energy Systems 9
2.4 Limitations and Opportunities 10

3 Preliminary Design of The HABLPR UAV **12**
3.1 Intial Maximum Take-off weight estimation 13
3.1.1 Iterative approach of MTOW Estimation 15
3.1.2 Results of Initial Weight Estimation Process 18
3.2 Wing Loading and Power Loading Estimation 22
3.2.1 Procedure to Calculate Wing Loading and Power Loading 23
3.2.2 Wing Loading and Power Loading Equation for Stall Speed 24
3.2.3 Wing Loading and Power Loading Equation for Maximum Speed . . 26
3.2.4 Wing Loading and Power Loading Equation for Rate of Climb . . . 28

3.2.5 Wing Loading and Power Loading Equation for Service Ceiling . . . 30
3.2.6 Summary of Wing Loading and Power Loading Analysis 32

4 Wing Design Process 35
4.1 Introduction 35
4.2 Design Requirements and Constraints 36
4.3 Wing Configuration Selection 37
4.4 Aerodynamic Analysis of Airfoil 39
4.4.1 Airfoil Selection Criteria 41
4.4.2 Comparison of Candidate Airfoils 41
4.5 Wing planform 46
4.5.1 Aerodynamic analysis of wing 48
4.5.2 Structural analysis of wing 51
4.5.2.1 Schrenk's method for calculation of loads 52
4.5.2.2 Structual analysis using ANSYS ACP 56
4.5.2.3 Failure analysis of composite Wing 61

5 Fuselage and Tail Design 65
5.1 Tail Design Parameters 66
5.2 Fuselage Design Parameters 71
5.3 Propulsion System Selection 73
5.3.1 Selection of Motor 73
5.3.2 Selection of Electronic speed controller 74
5.3.3 Selection of Propeller 74
5.3.4 Selection of Battery 77

6 Stability analysis 78
6.1 Static Longitudinal Stability 78
6.2 Static Margin and Neutral point Estimation 79

7 Manufacturing Process 82
7.1 Introduction 82
7.1.1 Brief Introduction to composite Material 83
7.1.1.1 Fibrous Composites 83
7.1.1.2 Particulate Composites 83
7.1.1.3 Flake/Whisker-Based Composites 84
7.1.2 Laminate Composites 84
7.2 Hand Layup Process 84
7.3 Vacuum Bagging Process 85
7.4 Manufacturing of Wing 86
7.5 Manufacturing of Fuselage 90
7.6 Manufacturing of Tail 93
7.7 Manufacturing and Assembly of 3D-Printed Parts 94

8 Testing, Electronic Component Integration, and Flight Stack Modification 97
8.1 Electronics Assembly 97
8.2 Overview of Electronic components 97
8.3 Mission Planning and Flight Testing 98
8.3.1 Initial Setup in Software in the Loop (SITL) and Hardware in the Loop (HITL) 99
8.3.2 Initial Bench Testing and Basic Air Testing 100
8.3.3 Final flight testing from lower altitude 103

9 Conclusions and future work 106
9.1 Conclusion 106
9.2 Future Scope 107

Bibliography 109

List of Figures

3.1 HiDRON Startospheric UAV Launch 14
3.2 HiDRON Startospheric UAV Launch 15
3.3 MTOW Estimation Algorithm 19
3.4 Velocity vs MTOW 20
3.5 Range vs MTOW 20
3.6 Range vs Battery Weight 21
3.7 Velocity vs Battery Mass 21
3.8 Acceptable region for $V_{\mathbf{stall}}$ 26
3.9 Acceptable region for $V_{\mathbf{max}}$ 28
3.10 Acceptable region for ROC 30
3.11 Wing Loading vs. Power Loading for Service Ceiling 32
3.12 Combined Wing Loading vs. Power Loading Plot for All Performance Criteria 33

4.1 Design velocity vs wing planform area 38
4.2 Stall velocity vs wing planform area 38
4.3 Eppler 214 Airfoil 43
4.4 Cl/Cd vs Angle of attack (α) for Airfoils 43
4.5 Cl vs Angle of attack (α) for Airfoils 44
4.6 $\frac{Cl^{3/2}}{Cd}$ vs Angle of Attack (α) for Airfoils 44
4.7 Cl vs Cd for Airfoils 45
4.8 Cm vs Angle of attack (α) for Airfoils 45
4.9 Physical representation of Wing 47
4.10 Span wise Variation of coefficient of lift 48
4.11 Coefficient of lift (Cl) vs. Angle of attack (α) for wing 49
4.12 Cl Vs Cd Variation of the wing 49
4.13 Aerodynamic efficiency (Cl/Cd) vs Velocity (V) for wing 50
4.14 Coefficient of Moment (C_m) Vs. Angle of Attack (α) 50
4.15 Schrenk's avg lift distribution 55
4.16 Ultimate Shear force diagram 55
4.17 Ultimate bending moment diagram 56
4.18 Wing surface divided into 10 segments for Analysis 57
4.19 Mesh generated on wing surface 58
4.20 Boundary conditions applied in the Structural Analysis 59
4.21 Total deformation 60

4.22 Equivalent (Von-mises) Stress . . . 61
4.23 Results of Tsai-Wu Failure Criterion Analysis . . . 63
4.24 Results of Tsai-Hill Failure Criterion Analysis . . . 64

5.1 Final Tail layout from XFLR5 . . . 69
5.2 Drag polar for Tail airfoil . . . 69
5.3 Coeff. of moment Vs α (Angle of attack) . . . 70
5.4 Coefficient of lift vs α (AOA) for Tail airfoil . . . 70
5.5 Sectional view of Front fuselage . . . 71
5.6 Front fuselage isometric view . . . 72
5.7 Complete fuselage With Tail Assembly . . . 72
5.8 Electric propulsion system . . . 73
5.9 Propeller comparison . . . 75

6.1 Cm Vs Alpha plot obtained from XFLR5 . . . 79
6.2 Variation of Cm Vs Alpha plot for UAV with CG location obtained from XFLR5 . . . 80

7.1 Hand lay-up process (Udupi,Rodrigues) . . . 85
7.2 Typical components of a vacuum bagging system. . . . 86
7.3 XPS block cross section with profile cut . . . 87
7.4 XPS foam Wing profile . . . 87
7.5 Leading Edge and Quarter Chord Patches . . . 89
7.6 Fiber Stacking in Wing Assembly . . . 89
7.7 Vaccum bagging of the wing . . . 90
7.8 XPS core foam blocks . . . 91
7.9 XPS Fuselage core . . . 91
7.10 Fiber stacking over fuselage core . . . 92
7.11 Vaccum bagging of fuselage . . . 92
7.12 Post processing of the Fuselage . . . 93
7.13 Final CAD Assembly . . . 95
7.14 Complete UAV Ready to fly 1 . . . 95
7.15 Complete UAV Ready to fly 2 . . . 96

8.1 First flight route . . . 100
8.2 Lateral and longitudinal distances . . . 101
8.3 Altitude Estimate's . . . 101
8.4 Dapron plane used for Firmware testing . . . 102
8.5 Dapron plane flight route . . . 102
8.6 Lateral and longitudinal distances . . . 103
8.7 Altitude Estimate's . . . 103
8.8 Final testing setup with Hexacopter . . . 104
8.9 Flight route over IITK Airstrip . . . 104
8.10 Lateral and longitudinal distances . . . 105
8.11 Altitude Estimate's . . . 105

List of Tables

3.1 Comparison of HiDRON and HABLEG Specifications 15
3.2 Performance requirements 23
3.3 Rate of Climb at Various Ceilings of the UAV 28

4.1 Geometric properties of the wing 37
4.2 Characteristics of Candidate Airfoils 41
4.3 Geometric properties of the wing 47
4.4 Geometric properties of the wing 51
4.5 Notable variable used in Schrenks analysis of wing 54
4.6 Material properties used in the structural analysis. 58

5.1 Horizontal tail specification 68
5.2 Vertical tail specification 68
5.3 Specifications of the propulsion system components 76

8.1 Final flight performance parameters 105

Dedicated to family.

Chapter 1

Introduction

1.1 Background

High-altitude meteorological research is crucial for understanding atmospheric conditions, weather prediction, and climate science. Weather balloons equipped with radiosondes have been used for over a century to collect valuable data on temperature, pressure, humidity, and wind velocity in the upper atmosphere [1][2][3]. These measurements are essential for predicting natural disasters and analyzing climatological patterns [1]. Despite the advancements in remote sensing satellites, weather balloons remain vital for improving the accuracy of weather predictions [4]. However, traditional weather balloon methods face challenges such as high costs, limited mobility, and labor-intensive setups [2]. Additionally, payload retrieval can be problematic due to unpredictable landing locations [5]. To address these issues, researchers have proposed innovative solutions, including the use of unmanned aerial vehicles (UAVs) for data collection and payload retrieval [5][6][7].

1.2 Motivation

The measurement of various meteorological parameters, such as pressure (P), temperature (T), relative humidity (RH), and horizontal winds, is crucial for accurate weather forecasting and for studying the thermal and dynamic states of the atmosphere.[3] In the past, multiple attempts have been made to investigate atmospheric phenomena using both remote sensing and in-situ techniques.

On any given day, nearly 1,800 weather balloons are launched worldwide [8]. Annually, approximately 75,000 meteorological sensors are deployed using high-altitude balloons; however, only around 20% (about 15,000) are successfully recovered [9].

Currently, two common methods for recovering payloads involve either regulating the balloon's pressure for a gradual descent or releasing the payload for free fall, with a parachute deployed to slow its descent. However, a significant challenge with these approaches is the unpredictability of the landing location. Sensor payloads frequently end up in hard-to-reach or undesirable locations, such as bodies of water or remote terrain, complicating recovery efforts. This low recovery rate results in a substantial loss of valuable data and equipment.

Unmanned Aerial Vehicles (UAVs) offer a more reliable and controlled method for retrieving these sensors, potentially increasing the success rate of sensor recovery and improving the overall efficiency of high-altitude operations.

In India, the challenges of sensor retrieval are even more significant. Due to frequent weather changes, balloon drift can range from 15 to 120 kilometers [3], posing a substantial challenge for manual payload recovery.

1.3 Problem Statement

High-altitude balloon-based meteorological research in India faces unique challenges, particularly in the retrieval of sensor payloads from extreme altitudes and over large distances. Current methods of payload recovery are often imprecise, time-consuming, and dependent on favorable weather conditions. This presents a significant limitation, especially when conducting high-altitude research where the sensor payload must be safely and accurately retrieved to ensure data integrity.

The specific challenge is to develop a UAV capable of autonomously retrieving a sensor payload weighing approximately 300 grams from altitudes as high as 35 kilometers, and distances of up to 120 kilometers beyond visual line of sight (BVLOS) or within line of sight (LOS)[3]. The UAV must navigate back to the balloon's launch location, even in unfavorable wind conditions, using its onboard propulsion system.

Additionally, a critical constraint in the design is that the UAV's maximum take-off weight (MTOW) must not exceed 3.2 kilograms. This is necessary to ensure compatibility with

low-lift capacity balloons, which are typically used in high-altitude operations. Achieving these specifications while maintaining precision, autonomy, and structural integrity poses a significant engineering challenge.

This research addresses these challenges by designing and developing a lightweight, autonomous UAV optimized for high-altitude payload retrieval in varying atmospheric conditions, thereby enhancing the efficiency of meteorological research in India.

1.4 Organization of the Thesis

This thesis is divided into nine chapters, each addressing key aspects of the design, analysis, manufacturing, and testing of a balloon-launched high-altitude payload retrieval (HABLPR) UAV designed for meteorological research.

Chapter 1 introduces the background, motivation, problem statement, and objectives of the research. It explains the need for a UAV capable of autonomously retrieving sensor payloads from high altitudes in challenging conditions. The chapter outlines the specific requirements and constraints, setting the foundation for the research conducted in later chapters.

Chapter 2 is dedicated to the literature review, providing a detailed examination of existing research on high-altitude balloon-launched UAVs, payload recovery technologies, and UAV design methodologies. This chapter identifies gaps in current approaches and highlights the technological innovations this thesis aims to contribute. The review establishes the context for the novel design features developed in this research.

Chapter 3 focuses on the preliminary design of the HABLPR UAV. It includes a comprehensive analysis of the maximum take-off weight (MTOW), wing loading, and power loading using the constraint-based analysis method. These calculations are essential to ensuring that the UAV meets both weight and performance requirements, providing the foundation for further aerodynamic and structural analysis.

Chapter 4 covers the wing design process, where aerodynamic and structural analyses are performed using ANSYS tools. The aerodynamic design ensures optimal performance, while structural analysis guarantees the wing can withstand operational stresses. This chapter demonstrates how the wing's geometry and material composition contribute to both efficiency and strength, aligning with the UAV's overall mission goals.

Chapter 5 discusses the design of the fuselage and tail, along with the selection of an appropriate propulsion system. The design ensures that the fuselage and tail provide stability and structural integrity, while the propulsion system is chosen to meet the requirements for range and endurance, particularly in high-altitude conditions with potential wind interference.

Chapter 6 focuses on the stability analysis of the UAV, specifically examining static stability and static margin to ensure that the UAV maintains longitudinal stability during flight. Although the analysis does not extend to dynamic stability, the chapter ensures that the UAV's static stability parameters are well within the safe limits for reliable performance under various flight conditions.

Chapter 7 details the manufacturing process, beginning with an introduction to the general fabrication techniques used in UAV construction. It then focuses on the specific manufacturing processes employed for this UAV, particularly the use of composite materials for lightweight and durable structural components. This chapter ensures that the UAV's design can be practically realized while meeting the weight constraints.

Chapter 8 discusses the testing and integration of electronic components, as well as the flight stack modifications required to make the UAV capable of autonomous navigation. This chapter highlights how these modifications enable the UAV to autonomously navigate back to the launch site, even under challenging environmental conditions, ensuring successful payload recovery.

Chapter 9 concludes the thesis by summarizing the key findings, including the UAV's design performance and its ability to meet the mission objectives. Additionally, this chapter discusses potential improvements for future work, such as increasing the payload capacity, enhanced long range (BVLOS) communication methods and further optimizing the UAV's autonomous navigation capabilities.

Chapter 2

Literature Review

2.1 High-altitude Meteorological Research and Balloon Systems

High-altitude meteorological research, initiated in the early 20th century, has undergone significant technological advancements, playing a crucial role in understanding atmospheric conditions, weather prediction, and climate science. Weather balloons equipped with radiosondes have been employed for over a century, collecting critical data on temperature, pressure, humidity, and wind velocity at high altitudes, contributing to weather observation and forecasting [1][2]. Early in this journey, the work of Dobson and Brewer (1946)[10] showcased the potential of high-altitude balloon research in advancing our understanding of the upper atmosphere. Since then, these systems have evolved, allowing scientists to gather crucial data for weather prediction, atmospheric modeling, and climate studies [4].

High-altitude balloons, capable of reaching altitudes up to 35 km or more, have been indispensable in collecting atmospheric data, providing a foundation for improving meteorological forecasting and understanding larger atmospheric phenomena. These balloon-based measurements have greatly enhanced our knowledge of the Earth's atmospheric layers, aiding both short-term weather forecasting and long-term climate modeling. However, despite the advancements, the challenge of recovering sensor payloads in a controlled manner remains a significant hurdle, particularly in unpredictable wind conditions.

Beyond traditional meteorological measurements, high-altitude balloons have also been widely adopted for aerosol sampling, which is vital for understanding global environmental

changes and air quality. Aerosols play a significant role in climate systems, influencing atmospheric chemistry and radiative forcing. However, the gathered samples in the payload were either brought down by controlling the balloon air pressure or were just dropped with a parachute to slow the descend speed to reduce the impact on landing.[6] Frequently, these drop locations are unfavorable for recovery. In the case of pressure-controlled balloon descents, the balloon may drift significantly.

2.2 UAV's in High Altitude Payload Retrieval

There have been numerous research projects initiated since the 1990s and 2000s focusing on the development of High Altitude Platforms (HAPs). A detailed review of these efforts can be found in [11], while the regulatory aspects surrounding HAPs are discussed extensively in [12]. The applications of HAPs in meteorological experiments, as well as their potential as an alternative to small satellites, are explored in [13] and [14].

Although the use of High Altitude Platforms (HAPs) is promising, their application as a replacement for high-altitude balloons in measuring atmospheric phenomena remains limited due to several factors. HAPs generally have a higher weight, cost, and operational complexity. Moreover, their energy requirements for reaching high altitudes are significant, and their operation demands skilled manpower. In addition, careful calibration is needed to ensure that the meteorological sensors are positioned in a way that avoids interference from the wake of any part of the platform.

In contrast, high-altitude balloons offer a simpler and more efficient method for atmospheric data collection. The primary measurements are typically made during the balloon's ascent, during which the surrounding air remains undisturbed by the platform, allowing for more accurate readings.

The energy requirements for balloon-based systems, especially when integrated with UAVs, are relatively low. The UAV can take advantage of its potential energy to glide back to its base location after being released from the balloon.

In response to the growing need for precise aerosol data collection and meteorological sensor recovery, recent research has focused on integrating unmanned aerial vehicles (UAVs) with high-altitude balloons to develop innovative sampling platforms. These systems, such as balloon-assisted UAVs for aerosol observation, have demonstrated improved control over

payload descent and recovery, addressing many of the logistical and recovery challenges inherent in traditional balloon-based methods [6][15].

Integrating UAVs with high-altitude balloon technology has opened new avenues for meteorological research, enabling more precise and reliable data collection while overcoming traditional recovery limitations. These advancements are especially relevant to the focus of this thesis, which seeks to design a UAV capable of retrieving sensor payloads from extreme altitudes, particularly for meteorological research applications.

2.3 Technical Considerations for High-altitude Payload Retrieval UAVs

Developing high-altitude UAVs for balloon-launched payload retrieval systems requires addressing multiple technical challenges. This section explores the navigation and control systems, structural and material considerations, and energy systems necessary for UAVs operating in extreme atmospheric conditions.

2.3.1 Navigation and Control Systems

The German Aerospace Center (DLR) developed the High Altitude Balloon Launched Experimental Glider (HABLEG), an experimental platform intended for flights up to 20 km. HABLEG incorporates avionic systems currently in development for full-scale High-Altitude Pseudo-Satellites (HAPS). Its flight control system, including navigation and control components, showcases the state-of-the-art in autonomous UAV operation at high altitudes [16].

DLR employed an in-house autopilot with specific flight modes programmed for different mission phases, enabling the UAV to operate autonomously during both ascent and descent. Additionally, a parachute system, deployed via an electromagnet, is incorporated to reduce descent speed during flight termination, ensuring a safe landing [16].

A significant challenge in high-altitude UAV operations is the occurrence of flat spin, often arising when the balloon is released from the UAV. This separation can cause inertia effects that result in reversed airflow over the UAV's lifting surfaces, leading the vehicle to assume a near-horizontal attitude with zero forward speed, making recovery from flat

spin difficult. To address this, both [16] and [17] utilized drogue chutes, which help orient the UAV in a nose-down position, enabling stabilization during descent.

For communication, [16] utilized two separate links: a primary 2.4 GHz link and a secondary 868 MHz link, ensuring reliable control even at altitudes of 30 km. This dual-link system has proven effective in maintaining robust connections over long distances, with similar configurations demonstrating stable communication up to 185 km during high-altitude tests [18].

In contrast, other research efforts in developing balloon-based UAVs for high-altitude aerosol sampling have used alternative systems. For instance, [6] employed a Pixhawk Cube as the flight controller. For recovery and tracking, this UAV uses an RFD 900+ modem radio transmitter to transmit essential flight data to the Ground Control Station (GCS) via the MAVLink protocol. This primary system enables real-time updates of coordinates and altitude, while a secondary GSM (Global System for Mobile Communication) network link transmits coordinates to the ground station in the event of an emergency or crash landing. This UAV also features a parachute mechanism to slow the descent rate, ensuring safe recovery upon completing its aerosol sampling mission [6]. Further research aimed at validating real-time Weather Research and Forecasting (WRF) modeling with a balloon-borne unmanned glider utilized the HiDRON, equipped with a commercial off-the-shelf (COTS) autopilot system [7]. The HiDRON system employs the UAVOS AP10.3 automatic control system, which manages aircraft control surfaces and an emergency parachute. Its telemetry unit operates with an integrated 928 MHz radio link, enabling real-time data processing and reliable control of the glider throughout its mission.

2.3.2 Structural and Material Considerations

The structural design of UAVs intended for high-altitude operations requires materials that offer a balance of strength, lightweight properties, and durability. These considerations are essential for enduring the extreme conditions encountered at high altitudes, including low temperatures, reduced air density, and exposure to high wind speeds.

The German Aerospace Center's (DLR) High Altitude Balloon Launched Experimental Glider (HABLEG) utilizes a combination of high-density thermocol, fiberglass, and carbon fiber for its construction [16]. High-density thermocol provides a lightweight, insulative

core that maintains structural integrity without significantly increasing the UAV's overall weight. To add durability, the outer structure incorporates fiberglass, which offers protection against environmental stresses that are typical at high altitudes.

To further reinforce the UAV, DLR employed carbon fiber tubing, known for its high strength-to-weight ratio, which enhances the overall rigidity and reduces the vehicle's weight. Additionally, carbon fiber contributes to thermal resistance, which is essential in the stratosphere where temperatures can plummet. This combination of materials enables HABLEG to withstand the physical challenges of high-altitude flight while optimizing payload capacity and energy efficiency throughout its mission.

A similar material approach is used in UAVs designed for WRF modeling validation, such as the balloon-based glider detailed in [7]. For UAVs dedicated to high-altitude aerosol sampling [6], high-density thermocol forms the primary structure, while the internal components are covered with aluminum tape. This tape prevents extreme internal temperature drops, reducing the risk of critical component failures during the mission.

2.3.3 Energy Systems

The energy systems of high-altitude balloon-based UAVs are designed to maximize efficiency while minimizing reliance on powered flight. One key advantage of these UAVs is their ability to harness potential energy during ascent. As the UAV ascends with the balloon, it stores potential energy that can be utilized during descent to control its trajectory and conserve battery power, enabling it to return to its starting location more efficiently.

In previous high-altitude UAV designs, such as the High Altitude Balloon Launched Experimental Glider (HABLEG) developed by the German Aerospace Center (DLR), onboard LiPo or Li-ion batteries provide power for the UAV's critical electronics and navigation systems [16]. These rechargeable battery systems are preferred for their high energy density and ability to supply consistent power despite altitude-related temperature fluctuations. For increased energy efficiency, HABLEG incorporates aerodynamic control surfaces and gliding techniques during descent, reducing the demand on its energy reserves and allowing it to return safely to its base with minimal power consumption.

Previous studies have also highlighted that extreme conditions at high altitudes, particularly low temperatures, can negatively affect battery performance. To address these issues, HABLEG and similar UAVs underwent rigorous thermal testing at the subsystem level.

These tests ensure that battery performance and overall energy management remain stable in the stratosphere's low-temperature environment.

In regions with challenging weather conditions, such as India during the monsoon season, increased wind speeds and turbulence may necessitate additional power for stable descent and navigation. In such cases, powered gliders are preferable as they offer the necessary thrust to counteract high winds and maintain control during the descent phase. This added capability ensures reliable and safe operation even under less favorable environmental conditions, broadening the application of balloon-based UAVs for various meteorological and atmospheric research missions.

2.4 Limitations and Opportunities

While powered gliders have demonstrated reliable performance in fulfilling mission parameters, they face several limitations that restrict their broader application. One primary challenge is their limited ability to navigate back to the home location under conditions of significant balloon drift and high wind speeds. These environmental factors, particularly common in India, can cause balloon drifts of up to 120 km, complicating retrieval and limiting the utility of current UAV systems for diverse meteorological needs across Indian weather stations.

Another limitation is the weight of existing powered gliders, which typically have a minimum weight of 4.5 kg. This exceeds the payload capacity of standard 3.2 kg weather balloons, which introduces the need to either reduce the UAV's weight or rely on larger, more costly balloons. Reducing UAV weight and size would not only make it compatible with existing balloon infrastructure but also decrease the operational cost associated with balloon launches.

Furthermore, seasonal wind patterns in India, such as those observed during monsoon months, introduce additional challenges for UAV stability and navigation. These turbulent conditions may necessitate the development of specialized powered gliders capable of withstanding high wind speeds, or alternatively, autonomous navigation systems that can adjust flight paths in real time to compensate for environmental disturbances.

Addressing these limitations opens opportunities for advancing UAV technology tailored to high-altitude atmospheric research in complex and diverse environments. Developing lighter, more cost-effective UAV designs with enhanced autonomous navigation and control

systems could make these platforms more viable for wide-scale deployment across varied meteorological stations.

Chapter 3

Preliminary Design of The HABLPR UAV

The UAV design process begins with problem identification and configuration selection, followed by the conceptual design phase. Conceptual design is the first and most crucial phase of UAV system design and development. This preliminary work has the potential to define the function, form, cost, and development timeline of the envisioned UAV system.

Identifying the problem statement and understanding the end user's needs is an essential starting point for this phase. General design requirements are formulated at this stage, and a satisfactory design configuration is developed.

The fundamental parameters determined during the conceptual design stage include:

- **Maximum Takeoff Weight (MTOW):** This parameter is critical as it influences the overall design and performance of the UAV. It dictates the size of the UAV, the required structural integrity, and the choice of materials.
- **Wing Reference Area (S):** The wing reference area is a key factor in determining the aerodynamic characteristics of the UAV. It affects lift, drag, and overall flight performance.
- **Power or thrust requirement of UAV (P):** This parameter governs the propulsion system design, affecting the UAV's ability to achieve and sustain flight. It influences the selection of engines or motors, fuel or battery capacity, and the system's overall efficiency.

These parameters not only govern the UAV's size and performance but also impact the solution's manufacturing cost and complexity. A well-conceived conceptual design will balance these factors to create an effective and efficient UAV system.

3.1 Intial Maximum Take-off weight estimation

Estimating the MTOW of a UAV is a crucial aspect of the design process, significantly influencing the overall performance and feasibility of the system. Several established methodologies for fixed-wing aircraft design provide a foundation for this estimation. However, the initial Maximum Takeoff Weight (MTOW) estimation for UAVs is inherently iterative and partially reliant on statistical data.

Raymer [19] describes an initial weight estimation technique for fixed-wing aircraft that employs empirical equations to predict weight components based on design parameters. While widely used, this method often needs adaptation for UAV applications due to scale differences and unique design considerations.

Sadraey [20] has significantly contributed to the weight estimation techniques specific to UAVs, highlighting the nuances and additional factors that must be considered in small-scale designs.

Despite these advancements, most numerical relationships in the literature tend to be less accurate for small-scale UAVs. When applied, these empirical relations can result in substantial errors. To mitigate this, a similarity method is explored where UAV parameters are selected through comparison with similar operational UAVs. This approach leverages the extensive development and testing of existing UAVs to inform the design process of new UAVs.

Operational UAVs offer valuable insights into design attributes as they have undergone rigorous conceptual design, building, and testing phases. Therefore, they represent a higher fidelity reference than simplified conceptual design tools can provide. By drawing parallels with these proven systems, more accurate and reliable weight estimations can be achieved for new UAV designs.

Selecting a similar UAV involves several considerations, including similar size, physical characteristics, technological approaches, cost factors, propulsion systems, launch and recovery methods, and mission profiles. These criteria ensure that the selected reference

UAV closely aligns with the design requirements and operational context of the new UAV, thereby enhancing the accuracy of the weight estimation process.

After thoroughly researching vehicles similar to our UAV design requirements, we identified two candidates: the HiDRON by UAVOS and Stratodynamics Inc. [21], and the DLR High Altitude Balloon Launched Experimental Glider (HABLEG) [22]. These UAVs provide valuable insights into high-altitude mission design attributes, performance, and operational capabilities.

HiDRON Stratospheric Aircraft: The HiDRON is a pioneering stratospheric glider developed by UAVOS and Stratodynamics Inc. Its recent night flight reached a new altitude record and successfully operated in beyond-visual-line-of-sight (BVLOS) mode, utilizing UAVOS' Autopilot. This flight included testing a new mini-EUSO AMON Airglow detector and advancing aspects of stratospheric flight dynamics, data links, and autonomous navigation. Despite harsh conditions, the HiDRON performed well, transmitting real-time data to the ground station during a 4-hour controlled descent.

DLR High Altitude Balloon Launched Experimental Glider (HABLEG): The HABLEG was specifically designed for high-altitude missions, offering another valuable reference for our UAV design. The development of HABLEG was meant to provide a robust framework for understanding the structural and aerodynamic requirements of a high-altitude balloon-launched UAV.

FIGURE 3.1: HiDRON Startospheric UAV Launch

FIGURE 3.2: HiDRON Startospheric UAV Launch

The capabilities of both UAVs are:

TABLE 3.1: Comparison of HiDRON and HABLEG Specifications

	HiDRON	**HABLEG**
Wingspan	3.4 m	3 m
MTOW	4.5 kg	7.4 kg
Payload Weight	1 kg	3 kg
Recorded Max Altitude	30 km	19.6 km

3.1.1 Iterative approach of MTOW Estimation

For iterative analysis, we take the HiDRON vehicle as our base vehicle and initiate the calculations. We consider the structural weight ratio $\left(\frac{W_{st}}{W_{to}}\right)$ and the propulsion system weight ratio $\left(\frac{W_{pr}}{W_{to}}\right)$ from historical data.

From historical data, we have the following ranges:

$$0.15 \leq \frac{W_{st}}{W_{to}} \leq 0.4 \tag{3.1}$$

(Structural weight ratio)

$$0.05 \leq \frac{W_{pr}}{W_{to}} \leq 0.2 \tag{3.2}$$

(Propulsion weight ratio)

Step 1: Taking the takeoff weight of the similar HiDRON vehicle as the takeoff weight of the new vehicle W_{to} to initiate the calculation:

$$W_{to} = 4.5 \text{ kg} \tag{3.3}$$

We are also aware that the payload capacity of the HiDRON vehicle is 1 kg.

$$W_{\text{payload-base}} = 1 \text{ kg} \tag{3.4}$$

Step 2: Using the payload requirement of our mission, i.e., 0.3 kg, and updating it into the formula given below, we get a new takeoff weight for the vehicle which has the same payload capacity as our vehicle.

$$W_{to} = \left(\frac{W_{st}}{W_{to}}\right) W_{to} + \left(\frac{W_{pr}}{W_{to}}\right) W_{to} + W_{\text{payload}} + W_{\text{Battery}} \tag{3.5}$$

Step 3: After updating the payload weight, our GTOW changes and necessitates the updating of the battery weight of the system. For the calculation of battery weight for the new GTOW of the vehicle, we first calculate the energy required to propel the UAV.

Energy required (ER) is given by:

$$\text{ER} = \text{Power required} \times \text{Total time of powered flight} \tag{3.6}$$

Or:

$$\text{ER} = P_r \times \Delta t \tag{3.7}$$

Here Δt is the total time during which the vehicle will be in powered glide mode.

In cruise mode:

$$L = W \tag{3.8}$$

$$T = D \tag{3.9}$$

Then, the power required for the desired flight time in powered mode is:

$$P_{\text{required}} = \frac{W_{\text{to}}}{\frac{L}{D}} \times V_{\infty} \tag{3.10}$$

Here:

- V_{∞} is the cruise velocity of the vehicle.
- $\frac{L}{D}$ is the aerodynamic efficiency of the vehicle.
- W_{to} is the takeoff weight of the vehicle.

Once we know the power required for the vehicle, we can calculate the amount of energy required to propel it. Substituting P_{required} in the energy required equation, we get:

$$\text{ER} = \frac{W_{to} \times V_{\infty}}{\frac{L}{D}} \times \Delta t \tag{3.11}$$

Once we know the amount of energy required, we calculate the weight of the battery needed to meet our propulsion requirements. For the calculation of the battery weight, we use the following formula:

$$W_{\text{Battery}} = \frac{ER}{(\prod_{i=1}^{n} \eta_i)\,\text{SED}} \tag{3.12}$$

Here:

- W_{Battery} is the weight of the battery.
- ER is the energy required for the UAV.
- $\prod_{i=1}^{n} \eta_i$ represents the product of all efficiency factors (η_i) in the propulsion system, ranging from $i = 1$ to n.
- SED is the specific energy density of the battery, defined as the amount of energy stored per unit weight of the battery.

Step 4: Once we have W_{Battery}, substitute this into the equation given for total takeoff weight calculation (Equation 3.5). By assuming that the current historical similar UAV's structure and propulsion system are sufficient to satisfy our requirement, i.e., keeping terms 1 and 2 in Equation 3.5 fixed for now, we get a new takeoff weight.

Step 5: As the takeoff weight changes as a result of Step 4, we recalculate the energy required and eventually the weight of the battery. As we change the weight of the battery, it changes the takeoff weight of the vehicle until:

$$|W_{\text{to new}} - W_{\text{to}}| \leq 10^{-5} \tag{3.13}$$

Even after Step 5, we are still assuming that the historical similar UAV's propulsion system and its structure are sufficient, which may not be true in the present case.

Step 6: Hence, in this step, we update the weight of the power plant system in Equation 3.5. We will decide the propulsion system based on the maximum power requirement. The general rule is to select the propulsion system such that it can fulfill the requirement at 50% of its maximum capacity.

During the power plant update, we assume term 1 of Equation 3.5 is constant.

Step 7: Now, as we have updated the weight of the propulsion system in the earlier step, the weight of the whole system will change, and hence we will need to update the weight of the battery again using the iterative method. We will iterate until we reach the desired minimum error (cost function).

Using the approach given above, we see that we reach a value with an error less than 20%.

Additionally, during the calculation phase, we must ensure that the value of $\frac{L}{D}$ used is achievable in the design phase.

We will also update the structural weight once we have enough information about the structure.

Note: as we have already discussed the possibility of error in our calculation we will take a margin of 20-30 % in our final MTOW calculation.

3.1.2 Results of Initial Weight Estimation Process

Using the method described above, I have developed a MATLAB code that performs an iterative analysis to estimate the maximum takeoff weight (MTOW) of a UAV. This estimation is based on historical weight ratios and specifications of a similar UAV. The process includes several steps, such as battery weight estimation, weight calculation, and

iterations to converge on a final MTOW. Additionally, the code generates plots to visualize the relationships between velocity, range, MTOW, and battery weight.

Here's a block diagram of the key steps involved in the initial weight estimation process:

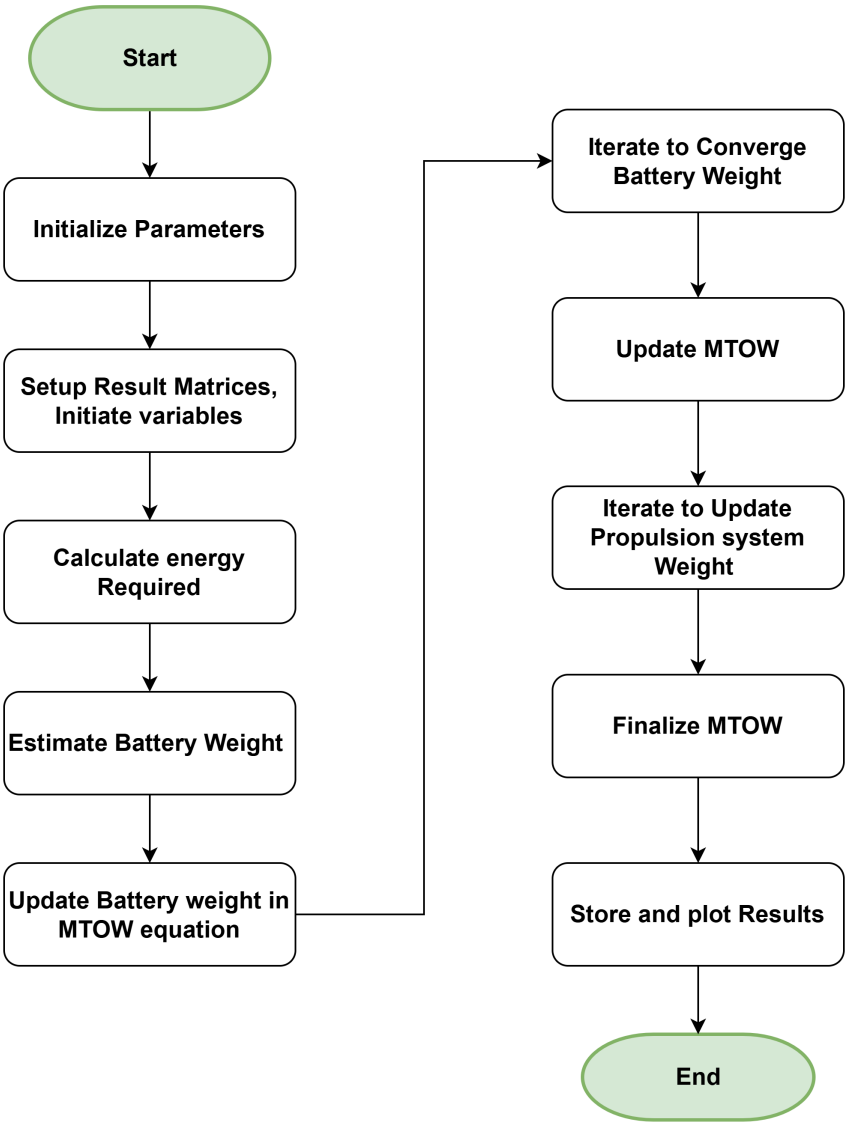

FIGURE 3.3: MTOW Estimation Algorithm

The following results were obtained from the MATLAB code:

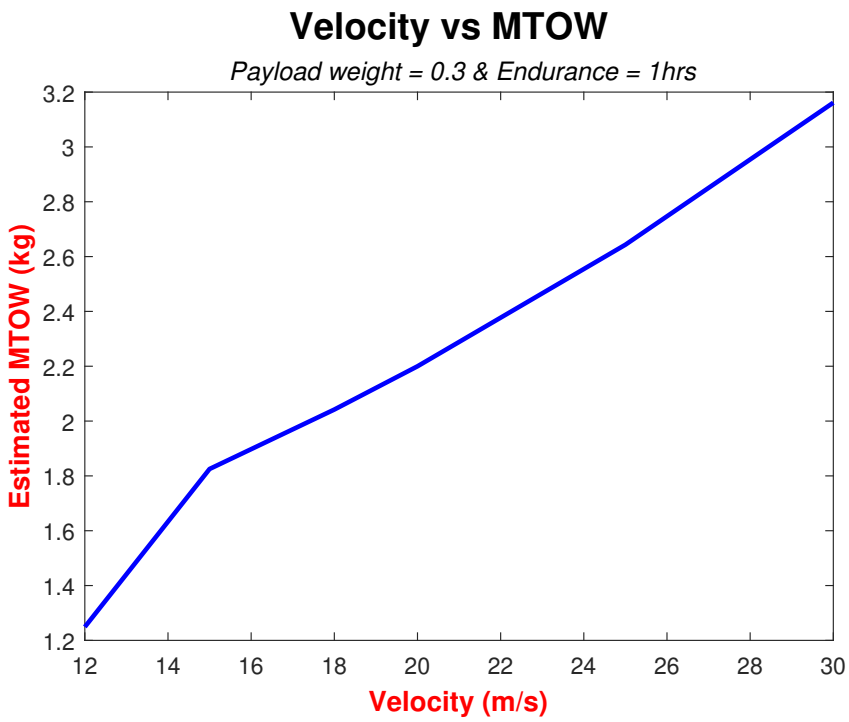

FIGURE 3.4: Velocity vs MTOW

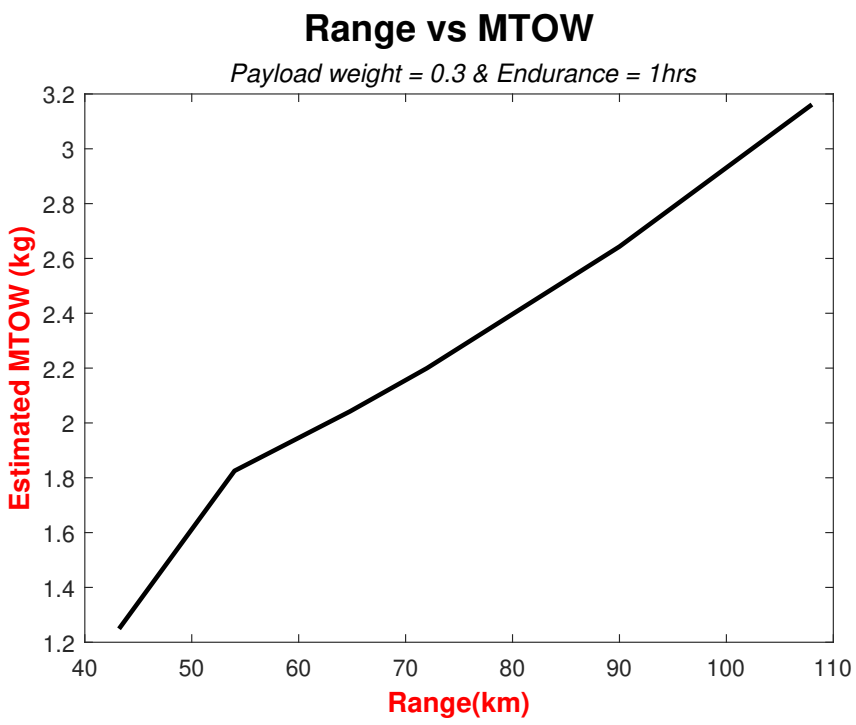

FIGURE 3.5: Range vs MTOW

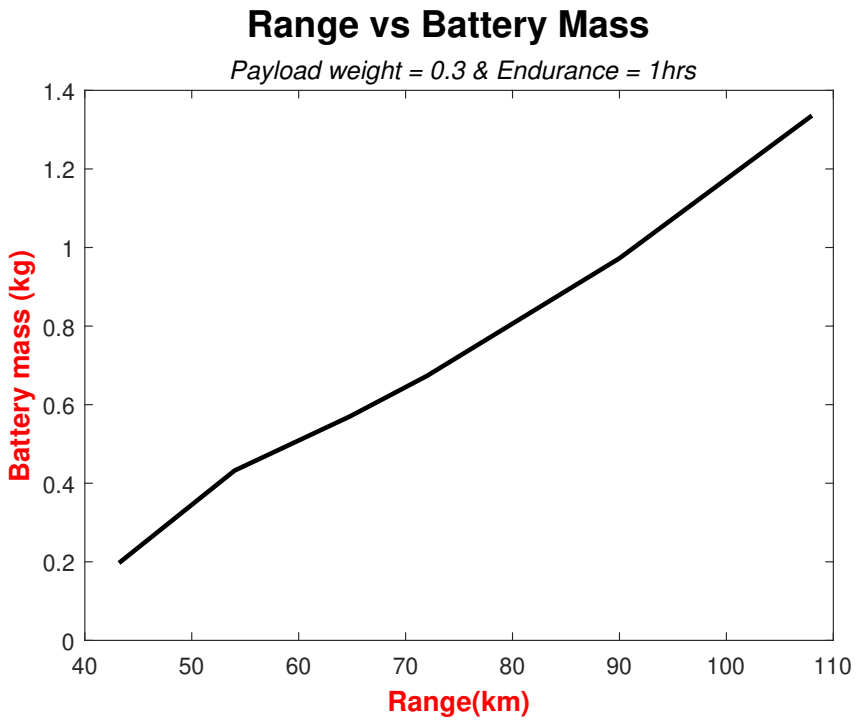

FIGURE 3.6: Range vs Battery Weight

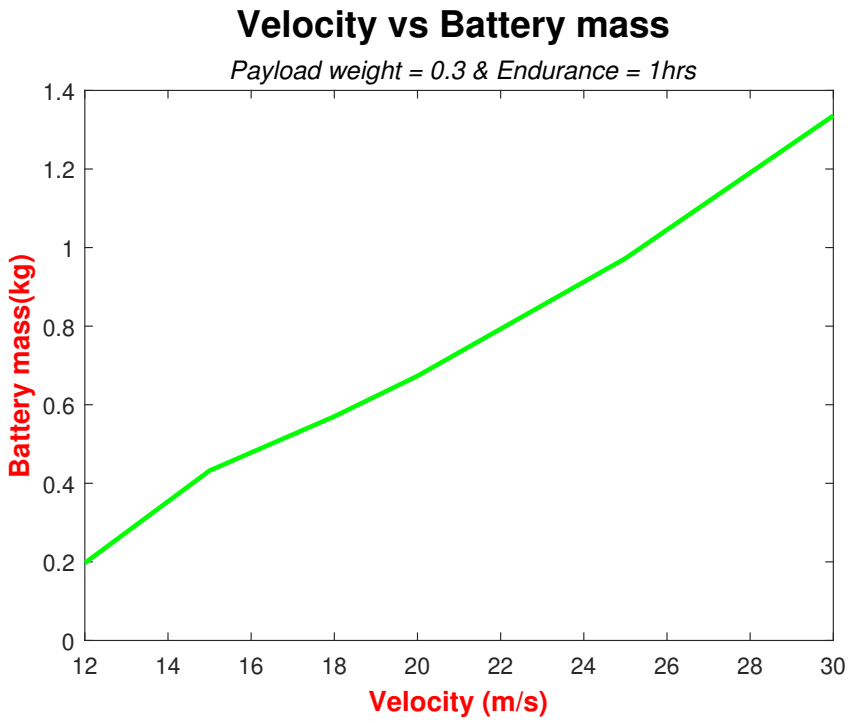

FIGURE 3.7: Velocity vs Battery Mass

Conclusion from Results: From the plots, it can be seen that our vehicle has a maximum takeoff weight of 3.2 kg in the case of a range of 108 km. Our UAV can achieve this maximum range in a powered mode flight for one hour with a cruise velocity of 30 m/s.

3.2 Wing Loading and Power Loading Estimation

This is a crucial step in the UAV preliminary design phase, where we determine the wing reference area (S_{ref}) and the propulsion system power (P). To calculate these variables, we first need to evaluate the wing loading ($\frac{W}{S}$) and power loading ($\frac{W}{P}$). This process uses a constraint-based analysis method, also known as the Matching Plot Technique.

The Matching Plot Technique was initially developed by NASA and has since been refined by various authors such as [19],[23]. Unlike the weight estimation technique, which relies on statistical methods and historical data ratios, this method utilizes vehicle performance requirements and basic flight mechanics theory.

Results obtained using this method are highly accurate and satisfy all specified vehicle performance requirements.

Performance Requirements: To determine the wing loading and power loading of the vehicle, we use the following performance requirements:

- Maximum speed (V_{max})
- Rate of climb (ROC)
- Stall velocity (V_{stall})
- Service ceiling (h_c), assuming the vehicle is launched in powered mode from sea level

In our case, there is no requirement for a takeoff run as the UAV will be launched using a balloon. Most of these parameters are determined from the problem statement, and sometimes these requirements are specified by the end user. For our design, we have used the following values to meet our mission requirements:

TABLE 3.2: Performance requirements

Performance Parameters	**Values**
Stall speed (V_{Stall})	12 m/s
MTOW	7.4 kg
Payload Weight	1 kg
Recorded Max Altitude	19.6 km

3.2.1 Procedure to Calculate Wing Loading and Power Loading

The Matching Plot Technique involves the following steps to calculate wing loading and power loading:

- For each performance requirement, derive an equation where power loading ($\frac{W}{P}$) is a function of the independent variable wing loading ($\frac{W}{S}$).The equations are in the following form:

  a) For Stall velocity, V_{stall}

$$\left(\frac{W}{P}\right)_{V_{\text{s}}} = f_a\left(\frac{W}{S}, V_{\text{s}}\right) \tag{3.14}$$

  b) For Maximum Velocity, V_{max}

$$\left(\frac{W}{P}\right)_{V_{\text{max}}} = f_b\left(\frac{W}{S}, V_{\text{max}}\right) \tag{3.15}$$

  c) For Rate of climb, ROC

$$\left(\frac{W}{P}\right)_{V_{\text{s}}} = f_c\left(\frac{W}{S}, ROC\right) \tag{3.16}$$

  d) For Service ceiling, h_{c}

$$\left(\frac{W}{P}\right)_{V_{\text{s}}} = f_d\left(\frac{W}{S}, h_{\text{c}}\right) \tag{3.17}$$

- Calculate these equations (using MATLAB in our case) and plot them on the same graph.
- Identify the acceptable region for each parameter on the plot.
- Determine the optimum design point within this region.
- Using the values at the design point, derive the optimum wing loading ($\frac{W}{S}$) and power loading ($\frac{W}{P}$).
- After obtaining the optimum wing loading and power loading, calculate the wing reference area (S) and the power requirement (P) using the maximum gross takeoff weight calculated in the previous section.

This method ensures that the design meets all specified performance requirements while optimizing the UAV's wing and power characteristics.

3.2.2 Wing Loading and Power Loading Equation for Stall Speed

Determining the stall condition of a UAV is very important as it sets the minimum speed threshold for the aircraft. At stall speed, the UAV experiences the minimum constant dynamic pressure required to maintain flight. As the UAV's speed decreases, the coefficient of lift (Cl) must increase to compensate. Therefore, for calculating the stall speed of the UAV, we consider the maximum possible coefficient of lift for the aircraft.

To derive the wing loading ($\frac{W}{S}$) equation for stall speed, we use the following relationship:

$$V_{\text{stall}} = \sqrt{\frac{2W}{\rho_s S_{\text{ref}} C_{L_{\max}}}} \tag{3.18}$$

Where:

- V_{stall} is the stall speed.
- W is the weight of the UAV.
- ρ_s is the air density at sea level.
- S_{ref} is the wing reference area.

- $C_{L_{\max}}$ is the maximum coefficient of lift.

Rearranging the equation to solve for wing loading ($\frac{W}{S}$):

$$\left(\frac{W}{S}\right)_{V_s} = \frac{1}{2}\rho_s V_{\text{stall}}^2 C_{L_{\max}} \tag{3.19}$$

This equation indicates that the wing loading at stall speed is directly proportional to the square of the stall speed and the maximum coefficient of lift, and is influenced by the air density.

For our case we are taking V_{stall} is to be equal to 12 m/s, hence we get:

$$\left(\frac{W}{S}\right)_{V_s} = 103.19\frac{N}{m^2}$$

As any Stall velocity lower than V_{stall} defined by design requirements is safe, hence the region left to the $\left(\frac{W}{S}\right)_{V_s}$ is acceptable.
Acceptable region for V_{stall} is shown in figure 3.8.

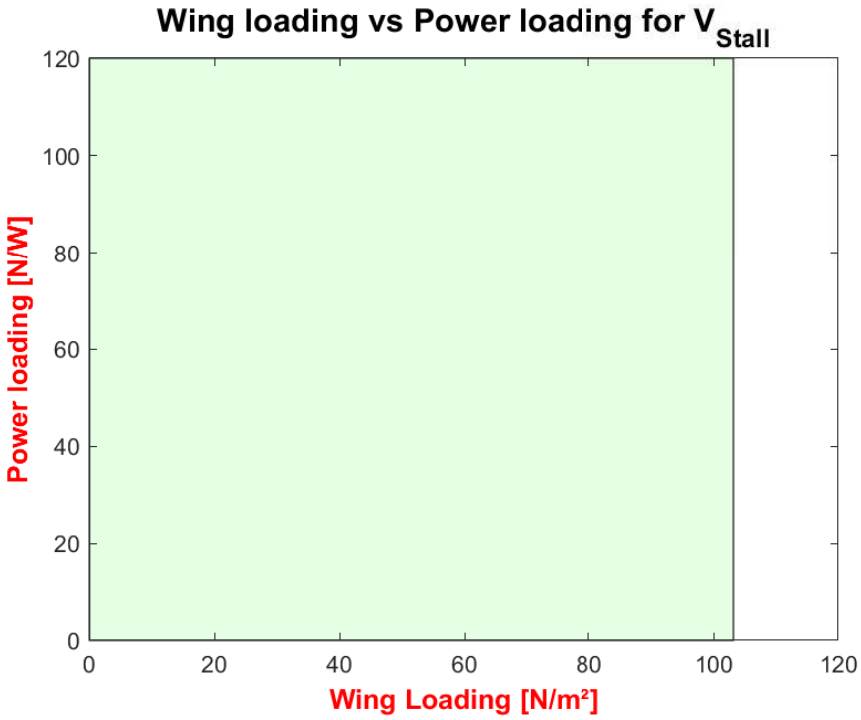

FIGURE 3.8: Acceptable region for $V_{\mathbf{stall}}$

3.2.3 Wing Loading and Power Loading Equation for Maximum Speed

The maximum speed of a UAV is determined by several critical factors, including its weight, wing area, and the power of its propulsion system. For our current UAV design, we have set a target maximum speed of 30 m/s, based on earlier analysis.

Achieving this speed involves balancing aerodynamic drag, thrust from the propulsion system, and the UAV's weight. Aerodynamic drag, which resists the UAV's forward motion, depends on air density, velocity, and the drag coefficient. To achieve maximum speed, the propulsion system must generate enough thrust to overcome this drag. This thrust is a function of the engine's power output and the efficiency of the propeller.

The power loading for maximum speed is calculated using the equation derived in [23] and given below:

$$\left(\frac{W}{P}\right)_{V_{\max}} = \frac{\eta_p}{\frac{1}{2}\rho_s V_{\max}^3 C_{D_0}\left(\frac{1}{W/S}\right) + \frac{2K}{\rho\sigma V_{\max}}\left(\frac{W}{S}\right)} \tag{3.20}$$

Where:

- η_p is the propeller efficiency at cruising altitude, which we take as 0.65 from [20].
- ρ_s is sea-level air density.
- $V_{\max}$ is the target maximum speed, set at 30 m/s.
- C_{D_o} is the drag coefficient, which we take as 0.0245 [20].
- W/S is the wing loading.
- ρ is the density at Service ceiling altitude (10000 m).
- K is the induced drag factor, which depends on the aspect ratio and Oswald efficiency factor.

$$K = \frac{1}{\pi \times e \times AR} \tag{3.21}$$

  - We are keeping the Ostwald efficiency factor as 0.8 [20].
  - Also taking the Aspect Ratio of the wing as 10.

- σ (Relative air density) equals the density density ratio at service ceiling altitude and sea level density.

Using the equation (3.20), we can calculate the variation of power loading with wing loading for the maximum velocity performance criteria. As the value of $V_{\max}$ increases, the power loading decreases. Therefore, any velocity greater than $V_{\max}$ is desirable, as it satisfies the performance requirement for maximum speed. Consequently, the region below the graph, where the power loading is lower than the required value at $V_{\max}$, is considered acceptable. Hence, the shaded region in figure 3.9 is the acceptable region for maximum speed requirement.

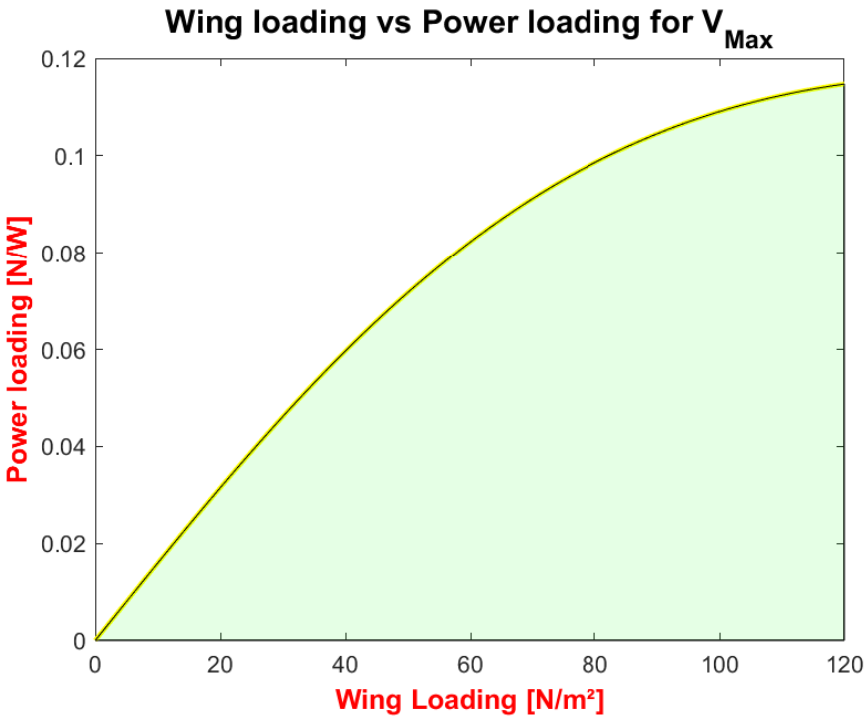

FIGURE 3.9: Acceptable region for $V_{\mathbf{max}}$

3.2.4 Wing Loading and Power Loading Equation for Rate of Climb

Rate of Climb (ROC) is an important performance measure for UAVs, indicating how quickly the aircraft can gain altitude. The ROC depends on the UAV's weight, wing loading, and the power from its propulsion system. For our UAV, we use a propeller efficiency η_p of 0.55 and a maximum lift-to-drag ratio ($\frac{L}{D}$) of 12, as referenced from [20]. These parameters ensure the UAV meets the required performance standards.

To determine the power loading ($\frac{W}{P}$) for a given wing loading ($\frac{W}{S}$) in relation to the rate of climb, we consider the following rates of climb at their respective altitudes:

TABLE 3.3: Rate of Climb at Various Ceilings of the UAV

Ceiling	**Rate of Climb**
Absolute Ceiling (V_{Stall})	0 m/s
Service Ceiling	0.5 m/s
Cruise Ceiling	1.5 m/s

The equation that relates power loading to wing loading for the rate of climb is:

$$\left(\frac{W}{P}\right)_{\text{ROC}} = \frac{1}{\left(\frac{\text{ROC}}{\eta_p}\right) + \left(\sqrt{\frac{2\left(\frac{W}{S}\right)}{\rho\sqrt{3C_{D0}/K}}} \cdot \frac{1.155}{\left(\frac{L}{D}\right)_{\max}\eta_p}\right)} \tag{3.22}$$

In this equation:

- η_p is the propeller efficiency, taken as 0.55 [20].
- ρ is the air density at the service ceiling, which is 10000 meters.
- C_{D_0} is the zero-lift drag coefficient, which is 0.0245 [20].
- K is the induced drag factor.
- $\left(\frac{L}{D}\right)_{\max}$ is the maximum lift-to-drag ratio.

By applying this equation, we can plot the variation of power loading with wing loading for the rate of climb. The acceptable region is defined by the combinations of wing loading and power loading that meet the desired rate of climb performance criteria.

Since ROC is in the denominator in equation 3.22 , an increase in ROC leads to a decrease in the overall wing loading value. Thus, any value above the ROC curve meets the design requirements, and hence the region below the ROC graph is considered acceptable. This ensures that the UAV can achieve the necessary rate of climb performance. Based on the above equations, we plot the following graph, and the acceptable region is shaded in blue.

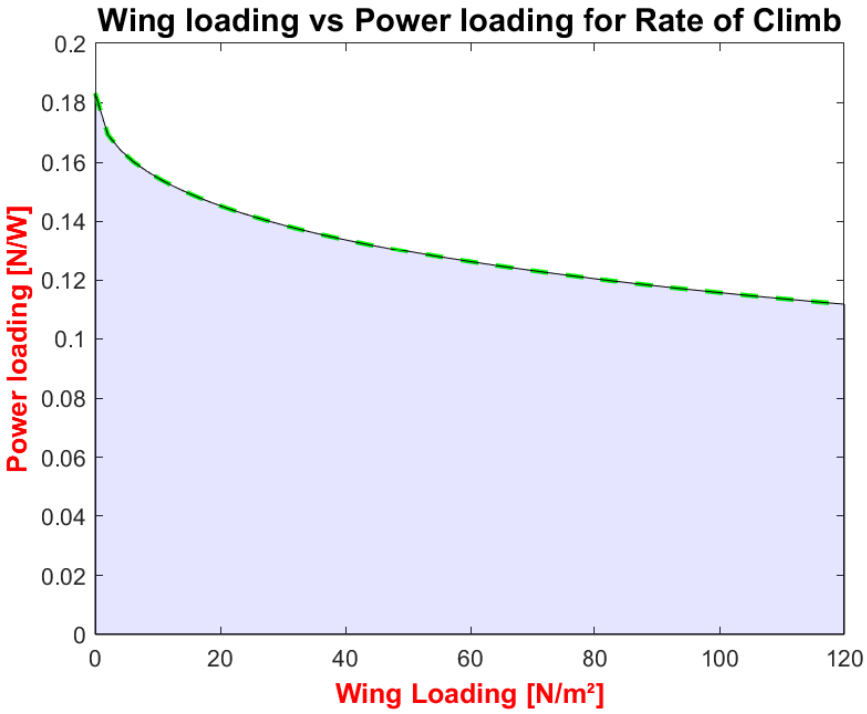

FIGURE 3.10: Acceptable region for *ROC*

3.2.5 Wing Loading and Power Loading Equation for Service Ceiling

The service ceiling is a critical performance parameter that defines the highest altitude at which our UAV can efficiently operate. Achieving the desired service ceiling is essential for our requirement. The service ceiling is influenced by factors such as the UAV's weight, wing loading, and the efficiency of its propulsion system.

For our UAV, we consider the following parameters:

- Propeller efficiency (η_p): 0.55
- Maximum lift-to-drag ratio ($\left(\frac{L}{D}\right)_{\max}$): 12, as referenced from [20]
- Air density at the service ceiling (ρ): 0.412 kg/m^3 (at 10000 meters)
- Zero-lift drag coefficient (C_{D_0}): 0.0245

- Induced drag factor (K): Calculated based on the UAV's aspect ratio and Oswald efficiency factor
- σ_{ac} is the ratio of air density at the cruise altitude to the sea level density, which is $\frac{\rho_c}{\rho_s}$.
- ROC_c is the rate of climb at the cruise ceiling.

The power loading ($\frac{W}{P}$) for a given wing loading ($\frac{W}{S}$) in relation to the service ceiling can be determined using the following equation:

$$\left(\frac{W}{P}\right)_{\mathrm{SC}} = \frac{\sigma_{ac}}{\left(\frac{\mathrm{ROC}_c}{\eta_p}\right) + \left(\sqrt{\frac{2\left(\frac{W}{S}\right)}{\rho\sqrt{3C_{D0}/K}}} \cdot \frac{1.155}{\left(\frac{L}{D}\right)_{\max}\eta_p}\right)} \tag{3.23}$$

To determine the acceptable region for wing loading and power loading, we consider various rates of climb at Service ceiling equal to 0.5 m/s, as shown in Table 3.3.
The acceptable region is defined by the combinations of wing loading and power loading that meet the desired service ceiling performance criteria.

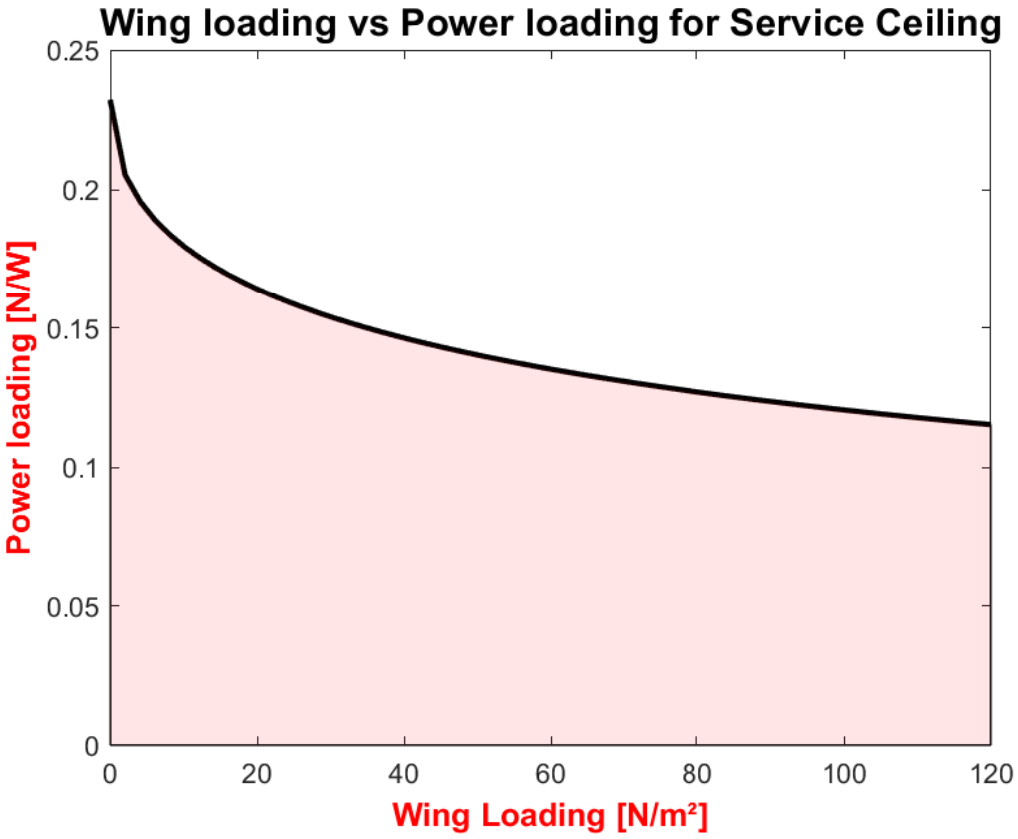

FIGURE 3.11: Wing Loading vs. Power Loading for Service Ceiling

Using the above equation, we plot the variation of power loading with wing loading for the service ceiling. Since the rate of climb appears in the denominator, an increase in the rate of climb leads to a decrease in the overall wing loading value. Consequently, any value above the service ceiling curve meets our design requirements, and the region below the service ceiling graph is considered acceptable. This ensures that the UAV can achieve the necessary performance at the desired altitude.

Based on the above equations and discussions, we plot the graph shown in Figure 3.11, with the acceptable region shaded in red.

3.2.6 Summary of Wing Loading and Power Loading Analysis

In this subsection, we summarize the results of the wing loading and power loading analysis for various performance criteria. By consolidating these findings, we aim to determine the

optimal design parameters for our UAV. The following graph represents the acceptable wing and power loading area for the design's initial iteration.

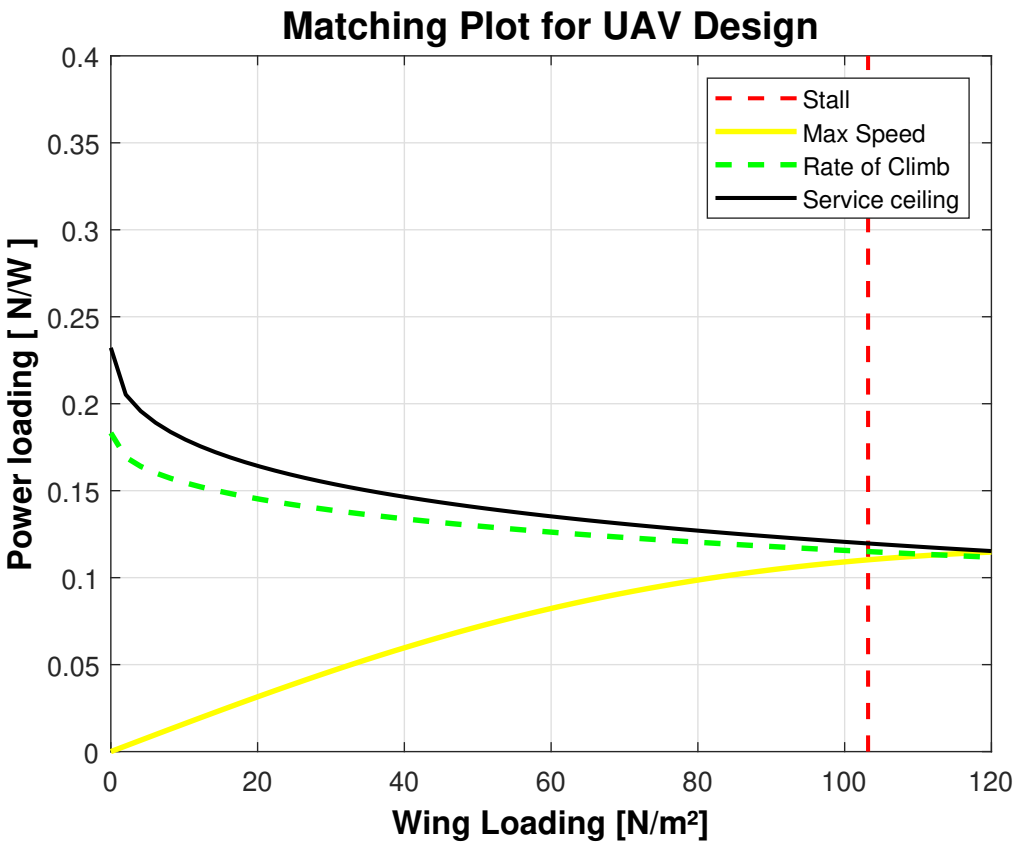

FIGURE 3.12: Combined Wing Loading vs. Power Loading Plot for All Performance Criteria

After identifying the acceptable region in Figure 3.12, we focus on determining the power loading corresponding to the smallest engine that meets our design requirements. Our goal is to identify the highest design point within the acceptable region, ensuring that the UAV can operate efficiently with the lowest possible engine power.

The process involves the following steps:

1. **Identify the Acceptable Region:** From the combined plot, we check for the area where the acceptable performance criteria for stall speed, maximum speed, rate of climb, and service ceiling overlap. This region represents the feasible combinations of wing loading ($\frac{W}{S}$) and power loading ($\frac{W}{P}$).

2. **Select the Highest Design Point:** Within the acceptable region, we look for the highest design point with some margin corresponding to the optimal engine power. For our case, a wing loading of $90\,\mathrm{N/m^2}$ and a power loading of $0.1\,\mathrm{N/W}$ seem to be a good design point.

3. **Calculate Required Power and Wing Platform Area:** Using the selected optimal wing loading and power loading values, we calculate the required power (P_{required}) and wing platform area (S_{optimal}) for the UAV:

$$P_{\text{required}} = \frac{W}{\left(\frac{W}{P}\right)_{\text{optimal}}} \tag{3.24}$$

$$P_{\text{required}} = \frac{3.2 \times 9.81}{0.1} \approx 313.92\,\mathrm{W}$$

Adding some margin, we take P_{required} as 315 W.

For the wing area:

$$S_{\text{optimal}} = \frac{W}{\left(\frac{W}{S}\right)_{\text{optimal}}} \tag{3.25}$$

$$S_{\text{optimal}} = \frac{3.2 \times 9.81}{90} \approx 0.349\,\mathrm{m^2}$$

Adding some margin, we take S_{optimal} as 0.4 m^2.

Where:

- P_{required} is the required power.
- S_{optimal} is the optimal wing area.

These values of power and wing area will serve as the starting point for our upcoming calculations. By following these steps, we ensure that our UAV is designed with the most efficient combination of wing loading and power loading. This method allows us to meet all performance requirements while minimizing power consumption and overall weight, leading to a more efficient and cost-effective UAV design.

Chapter 4

Wing Design Process

4.1 Introduction

The wing is arguably the most critical component of an aircraft, as fixed-wing UAVs cannot achieve flight without it. Due to its significant impact on the design and performance of all other UAV components, we start the detailed design process with the wing. The primary role of the wing is to generate sufficient lift (L). However, it also produces drag (D) and a nose-down pitching moment (M). While our goal is to maximize lift, it is equally important to minimize both drag and the pitching moment. Essentially, the wing functions as a lifting surface, generating lift through the pressure differential between its lower and upper surfaces [23].

In this chapter, we will discuss the wing design process for our UAV, focusing on developing a feasible and efficient wing design. This includes the selection of the wing type, mounting position, and comprehensive analysis. We will start with the only known variable, the wing plan-form area (S), as determined in Section 3.2 of Chapter 3.

We will begin by selecting the configuration of the wing, including the number of wings and their vertical location. Following this, we will compare various airfoils suitable for our application and select the optimal airfoil section. We will also determine the appropriate aspect ratio to ensure efficient aerodynamic performance.

Next, we will conduct an aerodynamic analysis using XFLR 5 software to calculate the lift, drag, and pitching moment for the chosen airfoil and wing configuration. This will be

followed by a load analysis on the wing using Schrenk's approximation [24] to understand the distribution of forces.

To ensure the structural integrity of the wing, we will perform a detailed structural analysis using Ansys Workbench. Finally, we will estimate the weight of the wing, completing the design process.

Through this detailed approach, we aim to design a wing that meets the performance requirements and operational efficiency of our UAV.

4.2 Design Requirements and Constraints

The design of our UAV is driven by the specific requirements and constraints associated with its mission of payload retrieval at high altitudes. One of the primary considerations is the wide range of Reynolds numbers the UAV will encounter, varying from as low as 20,000 to as high as 0.41 million (411,000). This wide range requires the wing to perform efficiently across different airspeeds and altitudes. Additionally, we have a constraint on the span of the wing, which is limited to 2 meters.

Given the high-altitude operation, the UAV must effectively handle varying air densities to maintain aerodynamic performance. This involves optimizing the wing design to ensure sufficient lift generation while minimizing drag and pitching moments in a low-density environment.

Weight is another critical factor in the UAV's design. Keeping the UAV's weight as low as possible is essential to maximize its efficiency and performance. A lightweight design not only enhances the UAV's flight endurance but also its ability to carry and retrieve payloads successfully.

Moreover, the wing design must ensure structural integrity to withstand the environmental stresses encountered during high-altitude flights. This includes resistance to aerodynamic loads and maintaining structural stability under different flight conditions.

Overall, the design process will balance aerodynamic efficiency, structural strength, and weight considerations to achieve an optimal wing design that meets the UAV's performance and mission requirements.

4.3 Wing Configuration Selection

The selection of wing configuration involves multiple aspects such as wing planform selection, wing mounting position, aspect ratio selection, and wing loading consideration, all of which directly influence the weight and strength requirements of the UAV.

Based on past experiences and ease of manufacturing, starting with a rectangular wing planform is a prudent choice. Rectangular wings are not only easier to manufacture but also provide favorable aerodynamic characteristics for our UAV's mission profile.

Opting for a high-wing configuration enhances stability through mechanisms such as the pendulum effect and dihedral effect. The pendulum effect occurs because the weight of the fuselage hanging below the wing creates a natural balance, reducing the tendency to roll. The dihedral effect, where the wings are slightly angled upwards, helps in correcting any roll movement by increasing lift on the lowered wing. Additionally, a high-wing configuration provides better ground clearance and simplifies handling during takeoff and landing. This configuration also contributes to improved overall performance, particularly in variable density environments typical of high-altitude operations.

To achieve optimal glide performance, a wing with a high aspect ratio is essential. Considering the constraints of a 2-meter wingspan and a maximum takeoff weight (MTOW) of 3.2 kg, selecting a chord of 0.2 meters is a prudent choice. This configuration allows us to achieve an aspect ratio of 10, calculated as

$$\text{Aspect Ratio (AR)} = \frac{\text{Wingspan}^2}{\text{Wing Area}} = \frac{2^2}{2 \times 0.2} = \frac{4}{0.4} = 10. \tag{4.1}$$

A high aspect ratio reduces induced drag, enhancing the UAV's glide efficiency and achieving the target glide ratio exceeding 10. The chosen wingspan of 2 meters and chord of 0.2 meters ensure that the UAV maintains a high aspect ratio while adhering to the weight constraint.

Table 4.1: Geometric properties of the wing

Wingspan	2 m
Wing Planform Area	0.4 m^2
Aspect Ratio	10
Mean aerodynamic chord	0.2 m
Wing loading	90 $\frac{N}{m^2}$

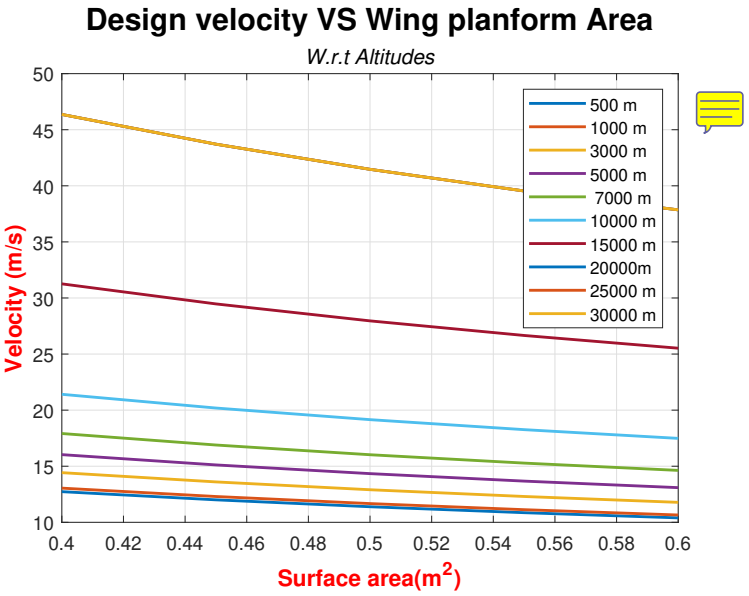

FIGURE 4.1: Design velocity vs wing planform area

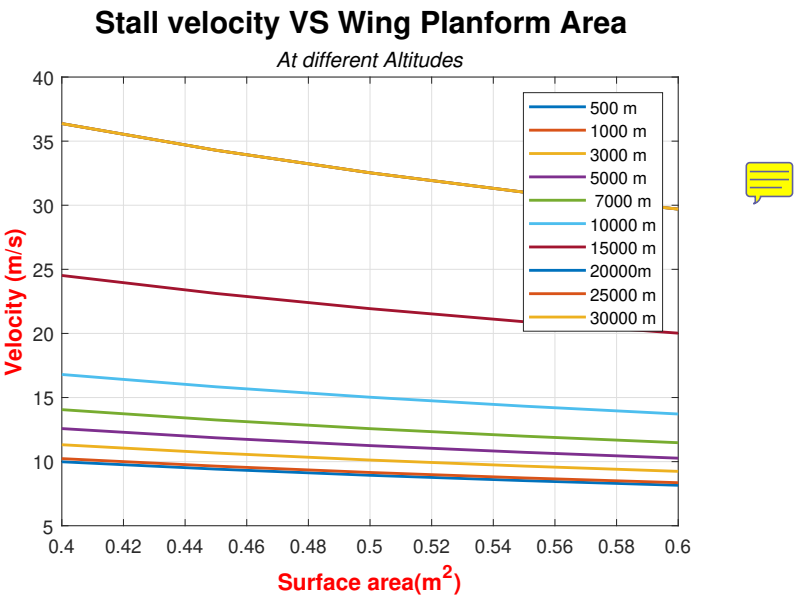

FIGURE 4.2: Stall velocity vs wing planform area

Analysis indicates that the required wing surface area increases with decreasing altitude due to denser air providing more lift per unit area (Figure 4.2 and 4.1). By selecting a wing area of 0.4 m^2, we ensure sufficient lift generation while avoiding stalling at various altitudes, supporting stable and controlled flight throughout the UAV's operational envelope.

Thus, the wing configuration, with a 2-meter wingspan and 0.2-meter chord, achieves an aspect ratio of 10, ensuring superior glide performance and structural integrity.

4.4 Aerodynamic Analysis of Airfoil

The aerodynamic analysis of the airfoil is conducted using XFLR 5 software. Initially, we need to calculate the required lift for the cruise condition, as the selection of the airfoil is based on the performance requirements of the UAV. This involves converting the performance requirements into non-dimensional lift and drag coefficients, which serve as the foundation for our analysis.

Following the methodology outlined in [23], the steps for the airfoil selection procedure are as follows:

1. **Determine the Average Weight:** The average weight of the UAV is known to be 3.2 kg.

2. **Calculate the UAV's Ideal Cruise Lift Coefficient (C_{L_c}):**

$$C_{L_c} = \frac{2 \cdot W_{\text{avg}}}{\rho \cdot {V_c}^2 \cdot S} \tag{4.2}$$

   - V_c is the cruising speed, which in our case is considered to be 20 m/s.
   - ρ is the air density at the cruising altitude (6000 m), which is 0.6596 kg/m^3.
   - S is the wing planform area, which is 0.4 m^2.

   Plugging in the values, we get:

$$C_{L_c} = \frac{2 \cdot 3.2 \cdot 9.81}{0.6596 \cdot 20^2 \cdot 0.4} \approx 0.594 \tag{4.3}$$

   Hence, the wing cruise lift coefficient comes out to be approximately 0.594.

3. **Calculate the Wing Cruise Lift Coefficient ($C_{L_{C_w}}$):** For initial calculation purposes, we use the following equation:

$$C_{L_{C_w}} = \frac{C_{L_c}}{0.95} \tag{4.4}$$

Substituting the value of C_{L_c}, we get:

$$C_{L_{C_w}} = \frac{0.594}{0.95} \approx 0.625 \tag{4.5}$$

4. **Calculate the Wing Airfoil Ideal Lift Coefficient:**

$$C_{l_i} = \frac{C_{L_{C_w}}}{0.9} \tag{4.6}$$

Substituting the value of $C_{L_{C_w}}$, we get:

$$C_{L_i} = \frac{0.625}{0.9} \approx 0.694 \tag{4.7}$$

After solving the above equation, we find the ideal lift coefficient to be approximately 0.694.

5. **Calculate the UAV Maximum Lift Coefficient ($C_{L_{\mathbf{max}}}$):** For the calculation of the UAV maximum lift coefficient, we use the following equation:

$$C_{L_{\max}} = \frac{2 \cdot W_{\text{avg}}}{\rho_0 \cdot {V_s}^2 \cdot S} \tag{4.8}$$

Here, ρ_0 is the air density at sea level, V_s is the stall speed of the UAV (considered to be 12 m/s at sea level), and S is the wing planform area. Plugging in the values, we get:

$$C_{L_{\max}} = \frac{2 \cdot 3.2 \cdot 9.81}{1.225 \cdot 12^2 \cdot 0.4} \approx 0.89 \tag{4.9}$$

6. **Calculate the Wing Maximum Lift Coefficient ($C_{L_{w_{\mathbf{max}}}}$):** Using the same logic as above:

$$C_{L_{w_{\max}}} = \frac{C_{L_{\max}}}{0.95} \approx 0.937 \tag{4.10}$$

7. **Calculate the Wing Airfoil Gross Maximum Lift Coefficient ($C_{L_{\mathbf{max_gross}}}$):**

$$C_{l_{\text{max_gross}}} = \frac{C_{L_{w_{\max}}}}{0.9} \approx 1.041 \tag{4.11}$$

These calculations will serve as the starting point for the selection of the airfoil. For our analysis, the requirement is to achieve an ideal lift coefficient of $C_{l_i} \approx 0.7$ and a gross maximum lift coefficient of $C_{l_{\text{max_gross}}} \approx 1.05$.

4.4.1 Airfoil Selection Criteria

The selection of the airfoil involves several criteria to meet our design objectives. Based on our design calculations, we need an ideal lift coefficient (C_{l_i}) of approximately 0.7 and a gross maximum lift coefficient ($C_{l_{\text{max_gross}}}$) of around 1.05.

In addition to these primary requirements, we consider several other important factors recommended by multiple sources such as [22], [23], and [25]. First, the airfoil should have a high lift-to-drag ratio and a steep slope for the lift curve ($C_{l\alpha}$), which contributes to overall aerodynamic efficiency. Additionally, a low (ideally near zero) pitching moment coefficient is crucial for maintaining stability and ease of control during flight.

Gentle stall characteristics are also essential; the airfoil should exhibit smooth performance changes near the stall region, avoiding any sharp variations that could affect flight stability. Structurally, the airfoil should not be too thin, allowing sufficient space for reinforcements like spars, which are vital for maintaining the structural integrity of the wing.

Furthermore, the airfoil should provide a high maximum lift coefficient and a low drag coefficient, ensuring optimal performance across different flight conditions. Finally, an effective drag bucket in the C_d vs. C_l plot is desirable, indicating minimal changes in drag with varying lift within this range, thus enhancing aerodynamic efficiency.

4.4.2 Comparison of Candidate Airfoils

Airfoil design is a tedious job; hence, based on our requirements, we have shortlisted a number of pre-existing airfoils from a range of possible options that were used in similar applications.

TABLE 4.2: Characteristics of Candidate Airfoils

Airfoil	**Thickness (t/c %)**	**At (x/c %)**	**Camber (y/c %)**	**At (x/c %)**
AG35	8.72	28.01	2.38	37.01
E214	11.1	33.1	3.7	56.9
S1223	15.3	19.9	8.3	55.2

The AG35 airfoil is known for its balanced aerodynamic performance, providing a good mix of lift and low drag, suitable for UAV applications requiring moderate lift coefficients and stable flight characteristics.

The E214 airfoil is characterized by its relatively high camber and thickness, making it suitable for applications where higher lift is needed at the cost of increased drag. This airfoil is often used in gliders and other light aircraft.

The S1223 airfoil is designed for applications requiring very high lift coefficients. It has a significant camber and thickness, which makes it suitable for low-speed, high-lift applications such as in RC aircraft and small UAVs designed for high-lift conditions.

A comparison of the airfoil is shown in the figures 4.4, 4.5, 4.6, 4.8, 4.7.

As shown in Figure 4.4, the E214 airfoil exhibits the highest aerodynamic efficiency among all airfoils, Also performing very well at low Reynolds numbers. This characteristic makes it an excellent candidate for our UAV, which requires efficient operation across various flight conditions.

Similarly, Figure 4.6 illustrates the loiter efficiency parameter ($\frac{Cl^{3/2}}{Cd}$). The E214 airfoil also shows the highest loiter efficiency among other potential candidates, indicating its capability to sustain prolonged flight durations with minimal energy consumption.

Furthermore, as seen in Figure 4.7, the E214 airfoil demonstrates stable behavior, with the drag coefficient (Cd) remaining constant over a significant range of lift coefficient (Cl) variations forming a proper drag bucket. This stability is crucial for maintaining consistent performance and efficiency. In contrast, the S1223 airfoil shows more erratic behavior at lower Reynolds numbers, and the AG35 airfoil has a somewhat limited range for Cl variation.

In Figure 4.5, we observe that while the S1223 airfoil has impressive lift characteristics, its abrupt stall behavior could pose stability issues for the UAV. The E214 airfoil, on the other hand, displays a more gradual and controlled stall behavior, which enhances flight stability and safety.

Lastly, Figure 4.8 shows that the pitching moment characteristics of the E214 airfoil are more favorable, ensuring better stability and control during flight. This is critical for maintaining the UAV's intended flight path and overall performance.

In summary, the E214 airfoil stands out as the most suitable option for our UAV. It offers high aerodynamic efficiency, excellent loiter efficiency, stable lift-to-drag behavior, and controlled stall characteristics.

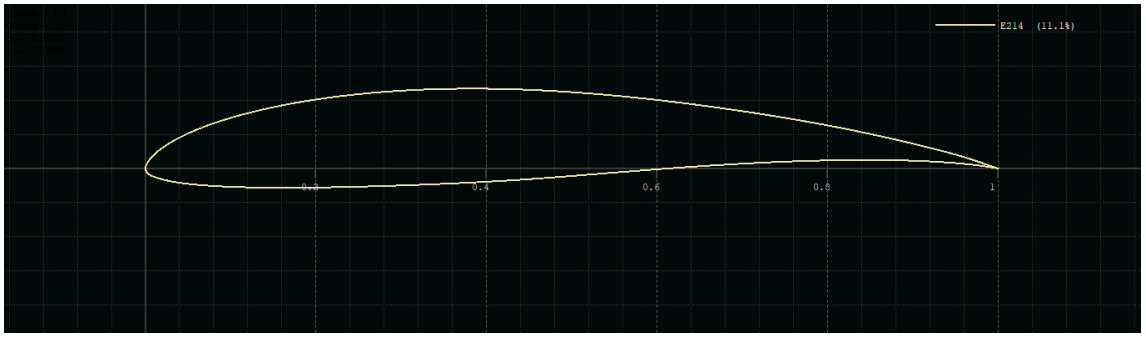

FIGURE 4.3: Eppler 214 Airfoil

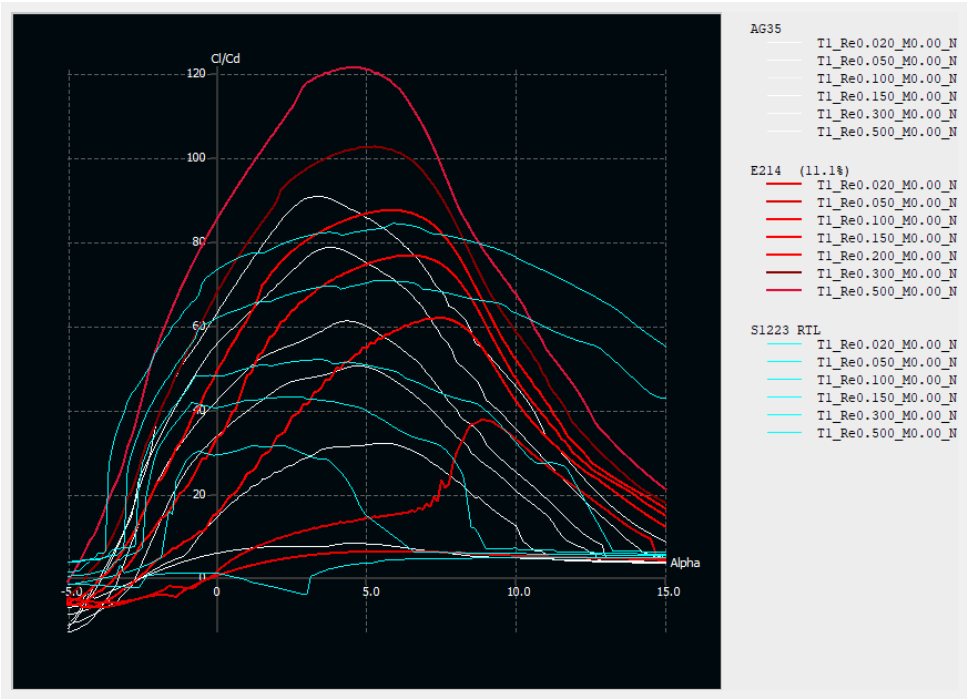

FIGURE 4.4: Cl/Cd vs Angle of attack (α) for Airfoils

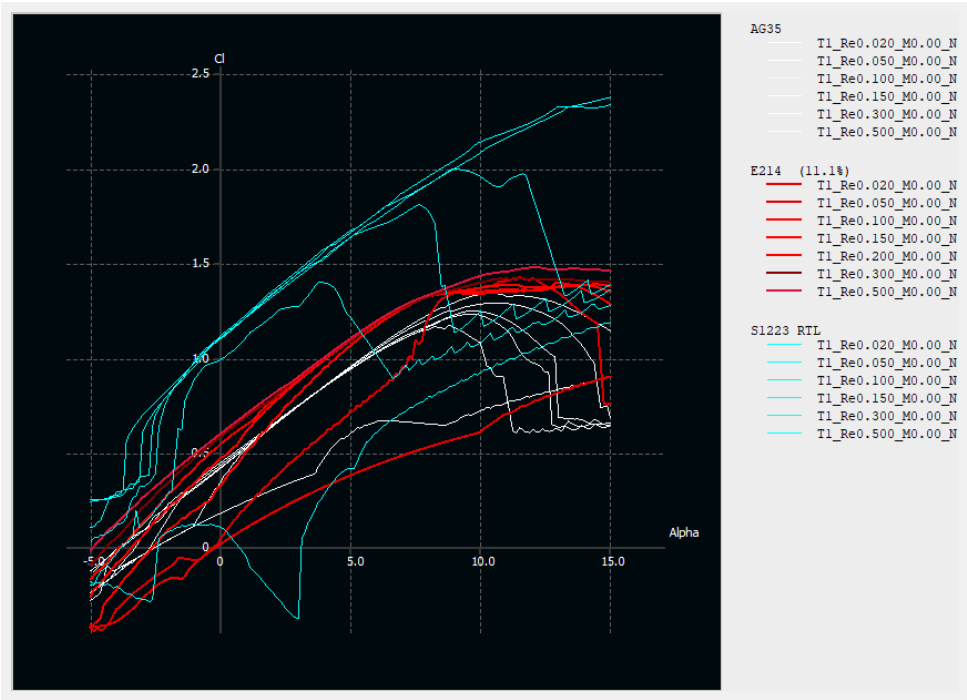

FIGURE 4.5: Cl vs Angle of attack (α) for Airfoils

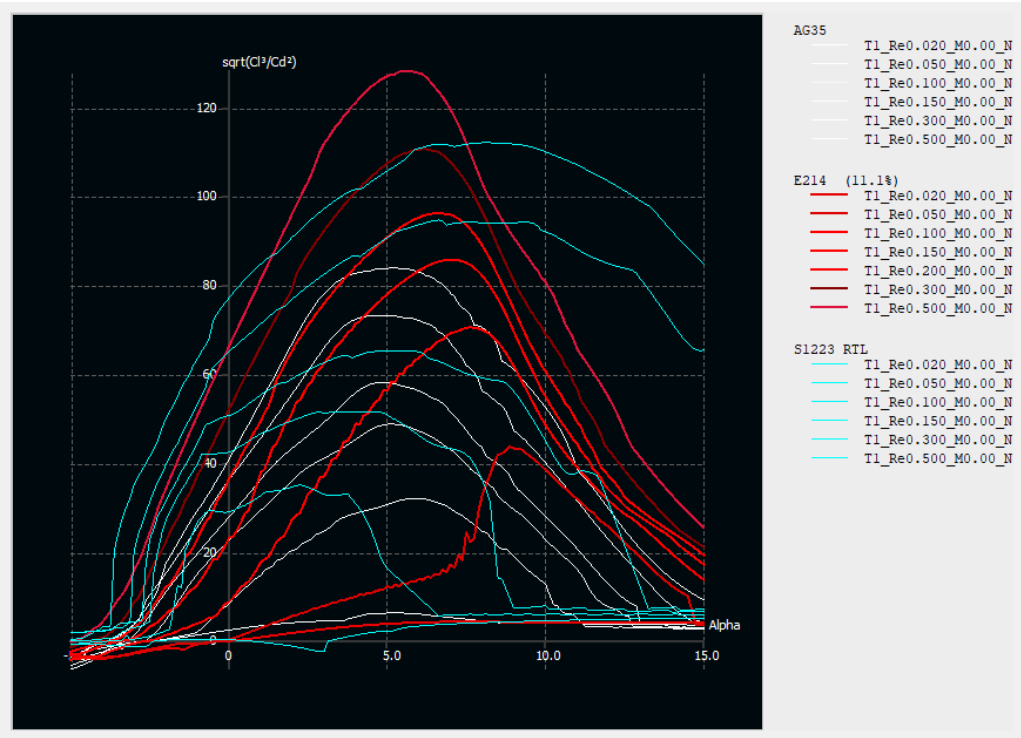

FIGURE 4.6: $\frac{Cl^{3/2}}{Cd}$ vs Angle of Attack (α) for Airfoils

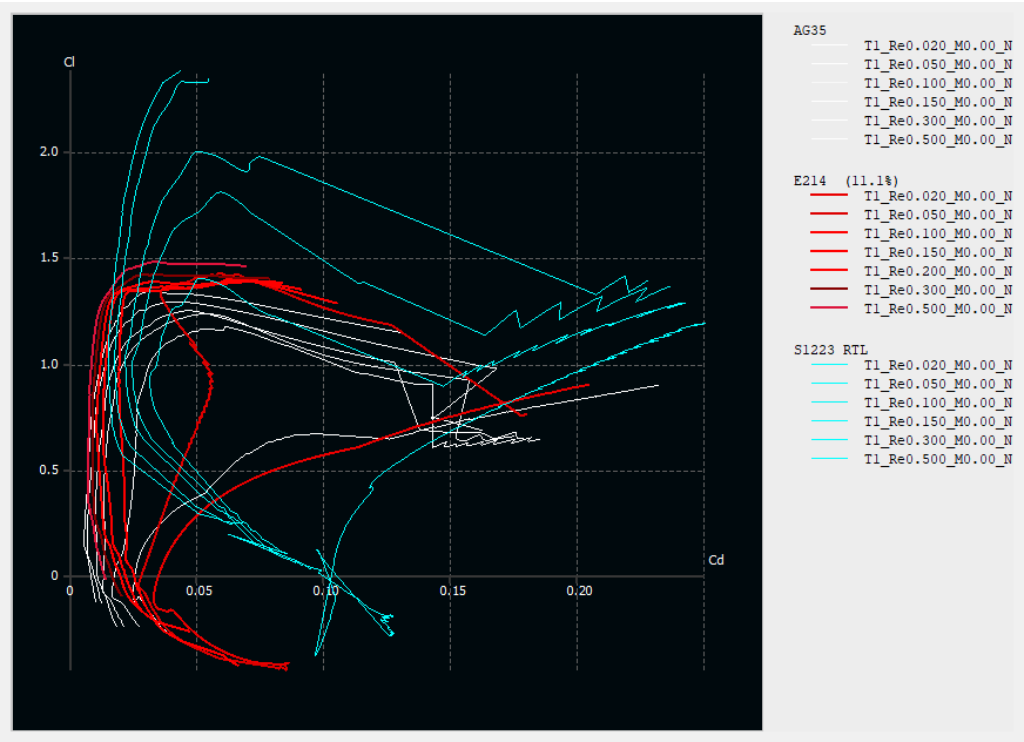

FIGURE 4.7: Cl vs Cd for Airfoils

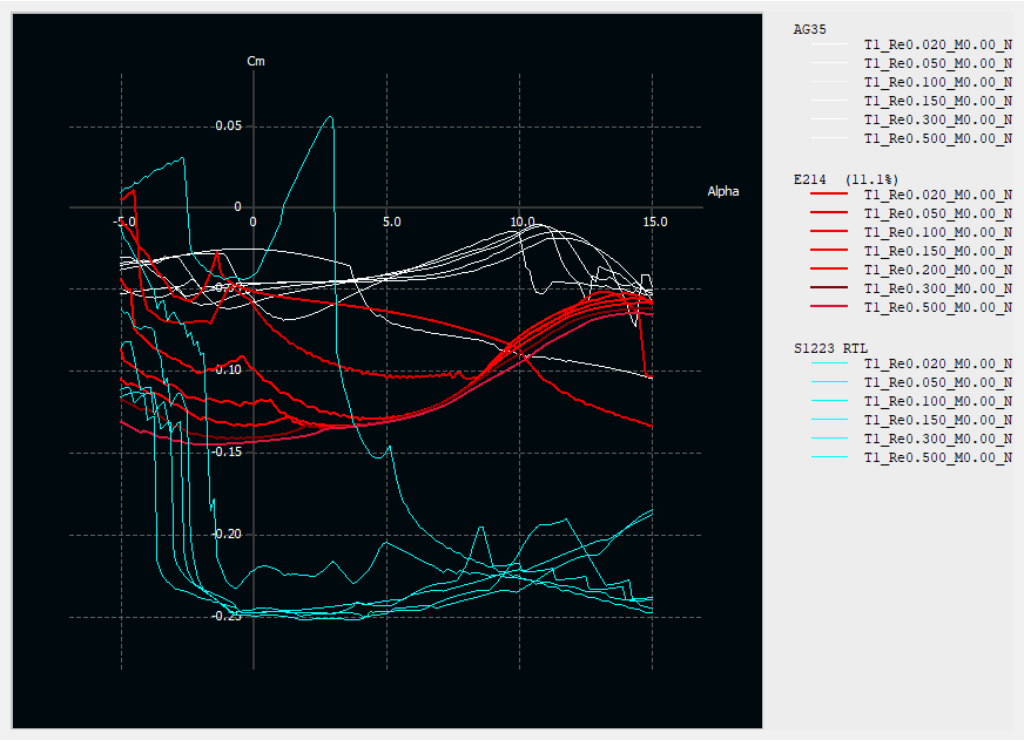

FIGURE 4.8: Cm vs Angle of attack (α) for Airfoils

4.5 Wing planform

According to Prandtl's wing theory, an elliptical wing shape is ideal for minimizing lift-induced drag and reducing stall speed. However, producing elliptical wings is both costly and time-consuming.

For our design, we have chosen to use a rectangular wing to keep the design simpler and more cost-effective. To mitigate tip stall and enhance control during stall conditions, we employ wing twist. This twist also helps in approximating an elliptical lift distribution. Raymer highlights that optimizing lift distribution through wing twist is effective only at a specific lift coefficient. Currently, we have set the geometric twist to zero and are using the same airfoil along the entire span to avoid complex designs and computational challenges.

The wing incidence angle, which is the pitch angle of the wing relative to the fuselage, is crucial for minimizing drag during specific flight conditions, typically during cruise. In an untwisted wing, this angle is simply the angle between the airfoil chord lines and the fuselage axis. The chosen incidence angle ensures that the wing operates at the optimal angle of attack for minimal total drag.

The Geometric properties and physical representation are given in Table: 4.1 and Figure 4.9 Respectively.

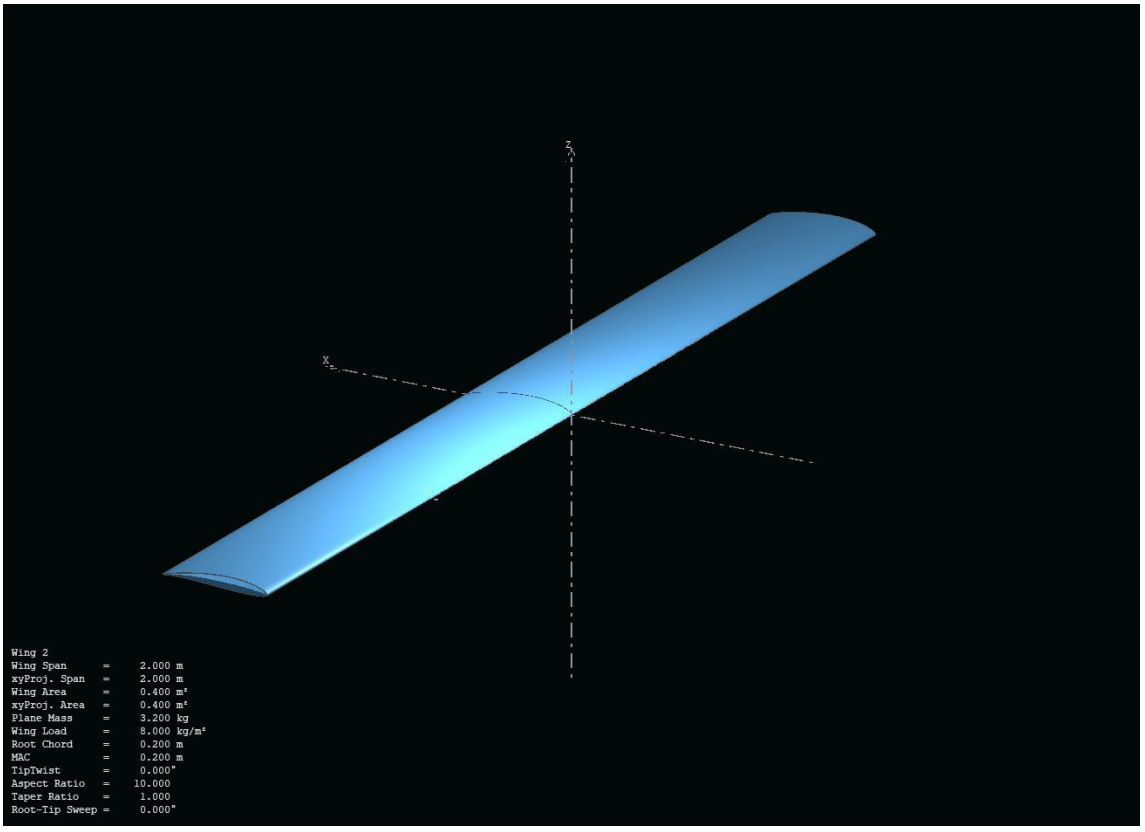

FIGURE 4.9: Physical representation of Wing

TABLE 4.3: Geometric properties of the wing

Wing Span	2 m
Root chord	0.2 m
Wing Area	0.4 m^2
Mean Aerodynamic chord (MAC)	0.2
Tip twist	0.0°
Aspect Ratio	10
Taper Ratio	1
Airfoil	E214
Dihedral Angle	0 °

4.5.1 Aerodynamic analysis of wing

The aerodynamic analysis of our wing design is conducted using XFLR5 software, employing the Vortex Lattice Method (VLM2) with ring vortices. This computational approach allows us to predict the lift distribution and overall aerodynamic characteristics of the wing. By discretizing the wing into a lattice of vortex rings, we can accurately model the circulation distribution over the wing surface and solve the governing equations to understand the wing's aerodynamic performance.

In our analysis, we utilize the Fixed Lift Polar type, which iteratively determines the dynamic pressure or angle of attack required to achieve a specified lift coefficient. This method is particularly useful for ensuring the wing can generate the necessary lift to balance the aircraft's weight under specific flight conditions. By leveraging this approach, we can optimize our wing design to meet performance requirements while considering manufacturing constraints and cost-effectiveness.

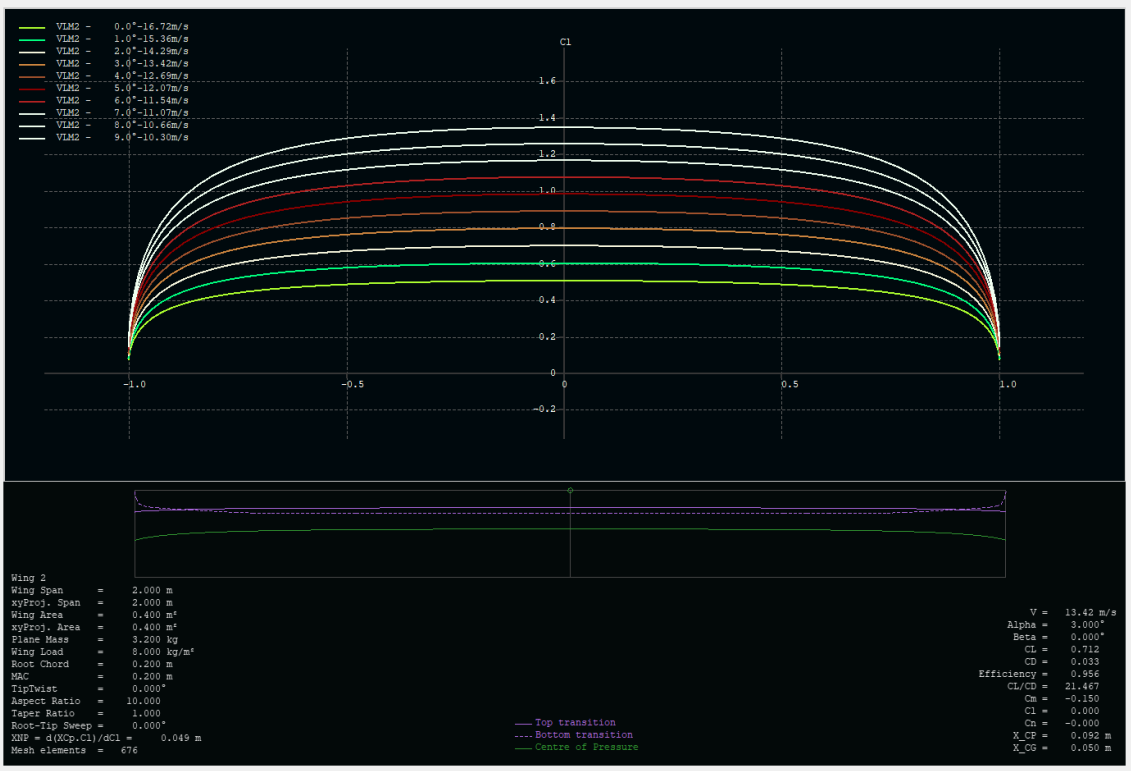

FIGURE 4.10: Span wise Variation of coefficient of lift

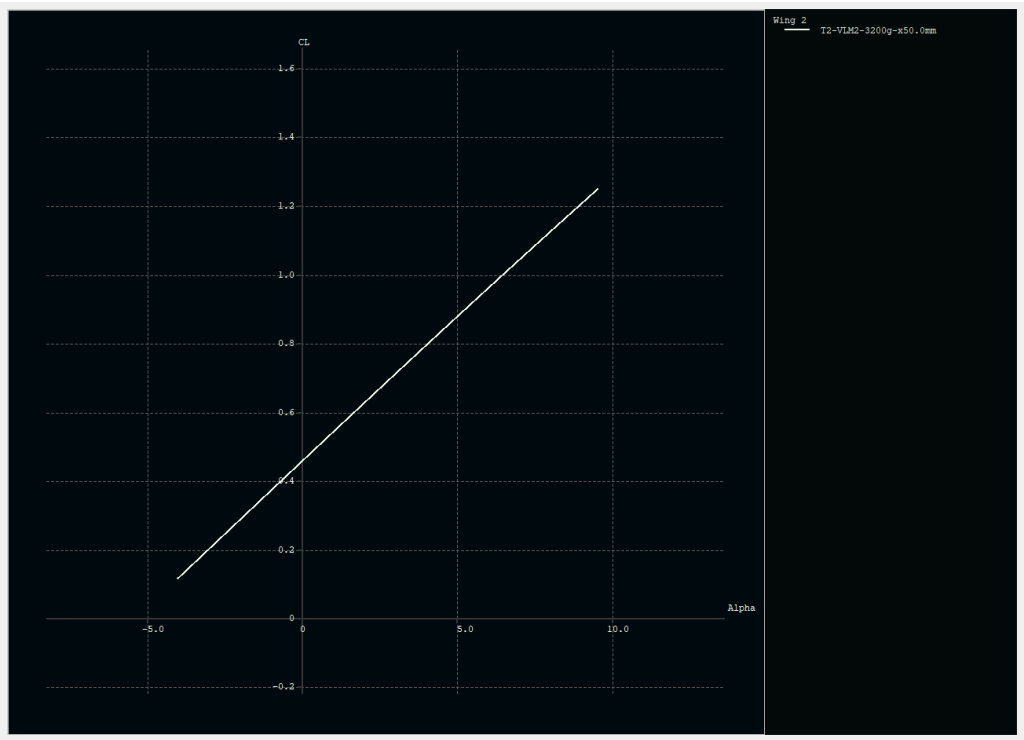

FIGURE 4.11: Coefficient of lift (Cl) vs. Angle of attack (α) for wing

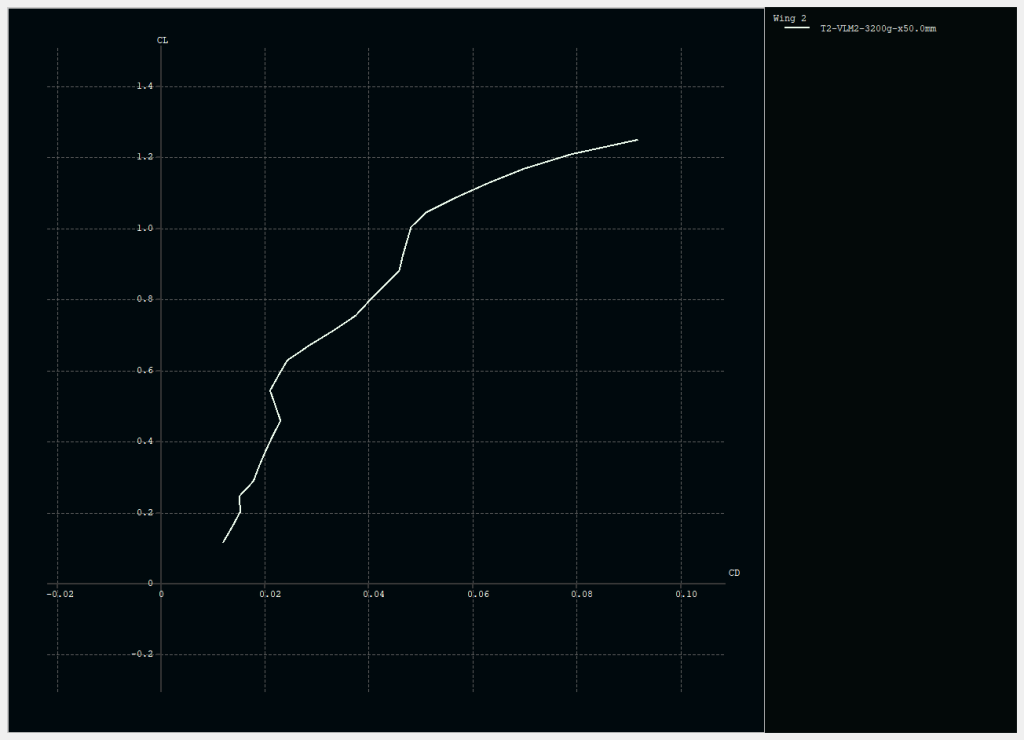

FIGURE 4.12: Cl Vs Cd Variation of the wing

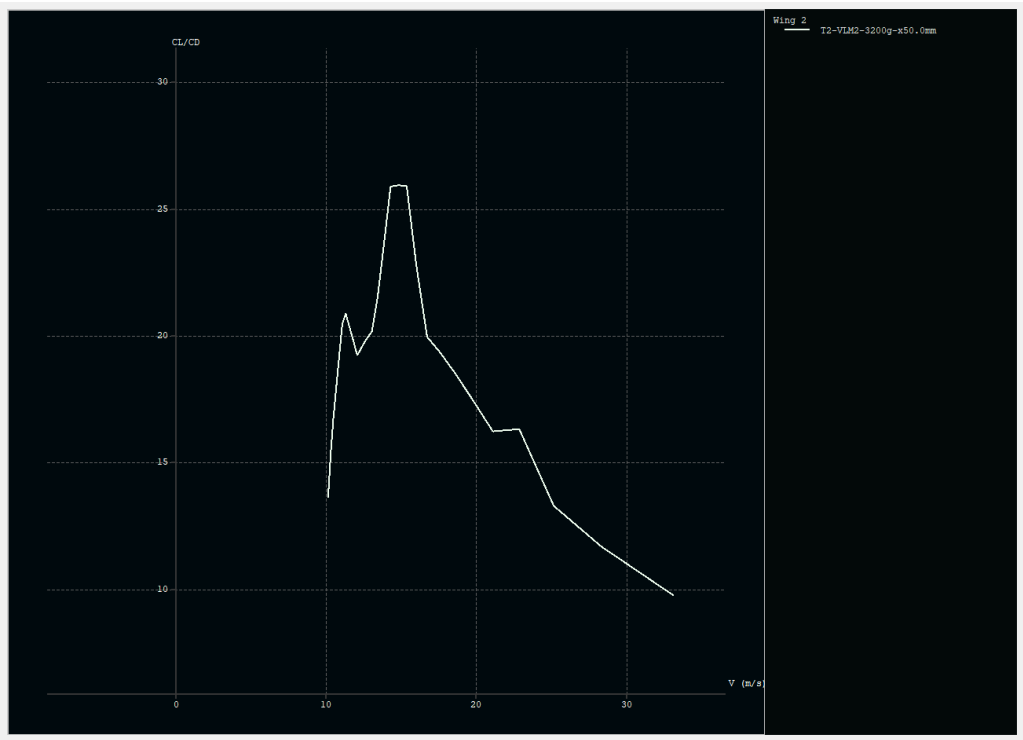

FIGURE 4.13: Aerodynamic efficiency (Cl/Cd) vs Velocity (V) for wing

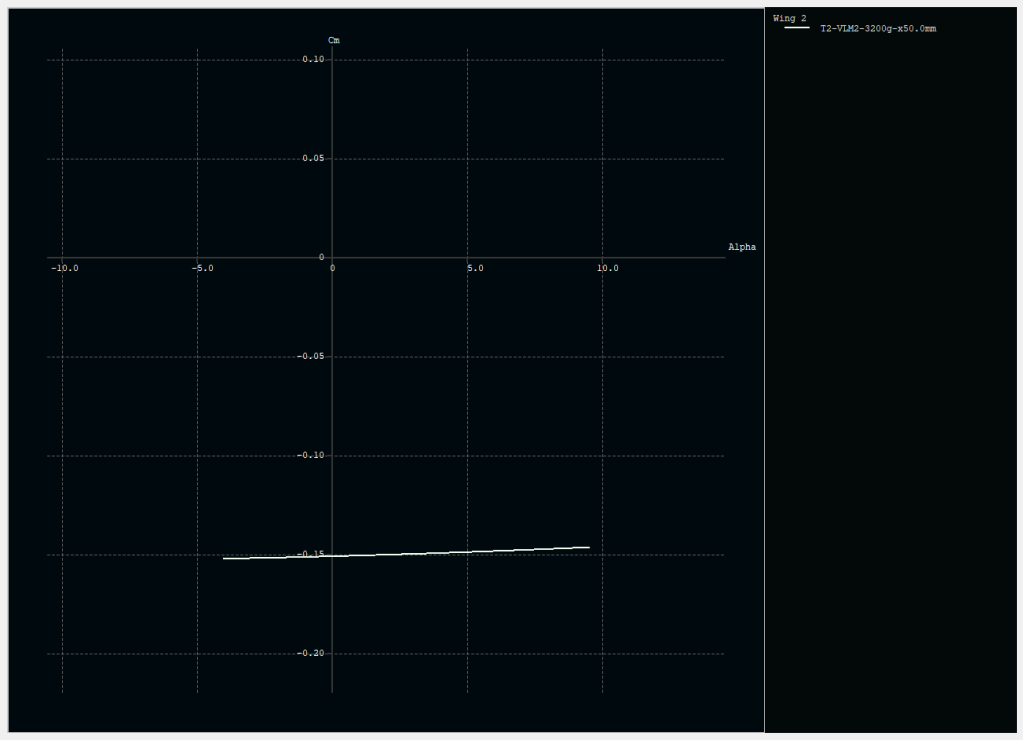

FIGURE 4.14: Coefficient of Moment (C_m) Vs. Angle of Attack (α)

TABLE 4.4: Geometric properties of the wing

Analysis Type	Viscous
Analysis Method	Vortex Lattice Method (Ring vortices)
Type of Polar	Fixed lift
Coefficient of lift	0.0833°or 4.773°
V_{cruise} for best cruise efficiency	15 m/s

4.5.2 Structural analysis of wing

An essential task in UAV design is calculating the wing's bending strength to appropriately size the wing and determine how to support the loads and moments acting on it. This process involves creating shear force and bending moment diagrams. Shear force refers to the vertical load on the wing, arising from both lift and the wing's weight. The bending moment represents the moments generated along the spar (a virtual line in our case) due to these shear forces acting at various points along the wing, such as the wing root and other relevant span stations.

An assumption about the lift force distribution along the wingspan is necessary to calculate these loads. The most efficient wing shape, minimizing induced drag, has an elliptical lift distribution, with zero lift at the wingtips and maximum lift at the centerline. In reality, most wings have a near-elliptical lift distribution with slight variations due to the wing's shape. Factors like wing twist, planform geometry, and changes in airfoil sections along the span also impact lift distribution and should be considered.

Selecting the right lift distribution approximation is crucial. A common method is the Schrenk approximation [24], which assumes a spanwise lift distribution that varies elliptically. This method will be explained further. It is important to consider the type of UAV structure before applying the Schrenk approximation. In our case, a cantilever monoplane, the Schrenk distribution method is typically suitable. Numerous applications and research have highlighted the utility and accuracy of Schrenk's approximation in comparison to CFD for estimating the loads and moments on the wing of a UAV [26][27][28]. This method provides insights into the lift distribution over a wing and demonstrates high accuracy.

Our wing is a sandwich structure, where an XPS foam core is covered with three layers of glass fiber using a wet hand lay-up process. The outermost layer is 50 GSM glass fiber woven fabric, and the two inner layers are 200 GSM glass fiber woven fabric.

Eventually, we will use advanced composites such as prepregs and carbon fiber woven fabric. In future versions of our UAVs, we plan to adopt more advanced manufacturing techniques, such as conventional thin-structure wings with carbon fiber cloth skins, and utilize the internal space for integrating avionics and actuators.

4.5.2.1 Schrenk's method for calculation of loads

Method:
In this section, we outline Schrenk's method for estimating the lift coefficient distribution along the span of a UAV wing. This method begins with an assumed UAV lift coefficient of 1.0, which is later adjusted to the actual lift coefficient to obtain the true lift distribution.

Schrenk's method is based on the principle that the spanwise lift distribution is proportional to the circulation at each span station. For an elliptical planform, the lift distribution is elliptical. Schrenk's method combines the actual wing planform shape with an ideal elliptical distribution to better approximate the load distribution.

The steps to apply Schrenk's method are as follows:

1. **Construct a Quarter Ellipse:**

$$\text{Ellipse height} = \frac{4S}{\pi b}\sqrt{1-\left(\frac{2y}{b}\right)^2}$$

   Begin by constructing a quarter ellipse with a length equal to the semi-span of the wing. The height of the ellipse at any spanwise station y is calculated using the equation above.

2. **Plot the Ellipse and Wing Chord:** Draw this quarter ellipse against span location y on a graph and add a plot of the wing's local chord at each span station.

3. **Average the Two Plots:** Draw a line averaging the two plots. This will generate a curve showing the parameter $c \cdot cl_\alpha$, where c is the local wing chord and cl_α is the local lift coefficient, keeping in mind these calculations are for a global lift coefficient $C_L = 1.0$.

4. **Calculate Local Lift Coefficient:** Divide the resulting Schrenk distribution $c \cdot cl_\alpha$ for the untwisted wing by the local chord c to obtain the local lift coefficient along the span for an aircraft lift coefficient $C_L = 1.0$ with no washout.

5. **Calculation of Other Relevant Quantities:** To calculate the shear force and bending moment along the semi-span, we first calculate some relevant quantities using the following equations:

$$L = 1.05nW - L_t$$

Where:

- n = Positive limit maneuver load factor
- W = UAV weight
- L_t = Tail load (+ive Upward)
- 1.05 is a factor to ensure a conservative estimate and to account for tail loads if $L_t = 0$.

Also:

$$L = qSC_L$$

Where:

- q = UAV dynamic pressure
- S = Wing area
- C_L = Overall wing lift coefficient

Therefore:

$$q \cdot C_L = \frac{L}{S}$$

6. **Determine Average Lift Coefficient:** From the data (chord and local lift coefficient) generated so far, find the average lift coefficient between each station.

7. **Calculate Average Lift Force:** Calculate the average lift force between each station based on the area of each spanwise element.

8. **Start at the Centerline:** Average the chord and lift coefficient values between two adjacent stations starting at the centerline.

9. Calculate the distance between each station, which we call the spanwise element width.

10. Calculate the area of each spanwise element δS.

11. Then, find the lift force generated by each spanwise element using the equation:

$$\text{Element lift} = q \cdot C_L \cdot \delta S \cdot C_{l\alpha}$$

    Where:

    - q = Dynamic pressure
    - C_L = Coefficient of lift
    - δS = Element area
    - $C_{l\alpha}$ = Average unit lift coefficient for an element

12. **Calculate Limit Shear Force:** Sum all the lift forces up to each element from the wingtip to calculate the limit shear force at each spanwise station.

13. **Calculate Limit Bending Moment:** Integrate the shear force curve from the wingtip, where the bending moment is zero (unless a winglet is present), to calculate the limit bending moment at each spanwise station.

14. **Calculate Ultimate Shear and Bending Moment:** Determine the ultimate shear and bending moments by applying appropriate safety factors to the limit values obtained in the previous steps.

By following these steps, Schrenk's method allows for an estimation of the lift distribution along the wing span, which is crucial for designing an efficient and structurally sound wing.

Table 4.5: Notable variable used in Schrenks analysis of wing

Maximum lift coefficient	1.3
Speed (m/s)	40
Weight of the UAV (kg)	3.2
Maximum positive limit load factor	3.2

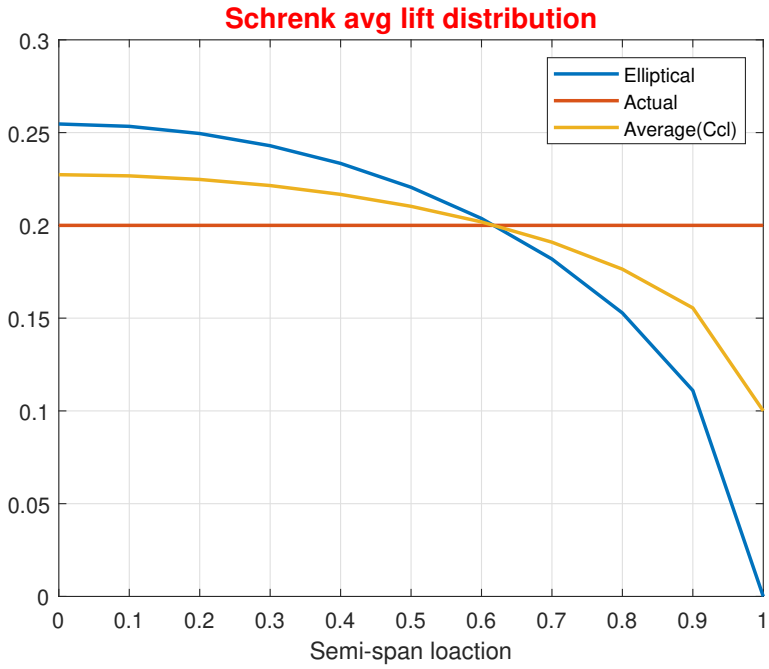

FIGURE 4.15: Schrenk's avg lift distribution

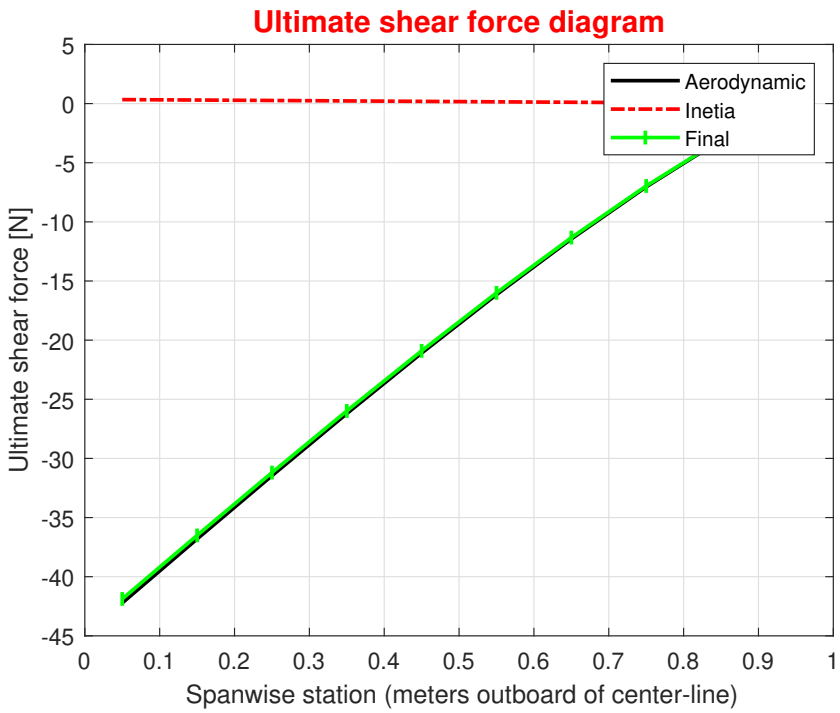

FIGURE 4.16: Ultimate Shear force diagram

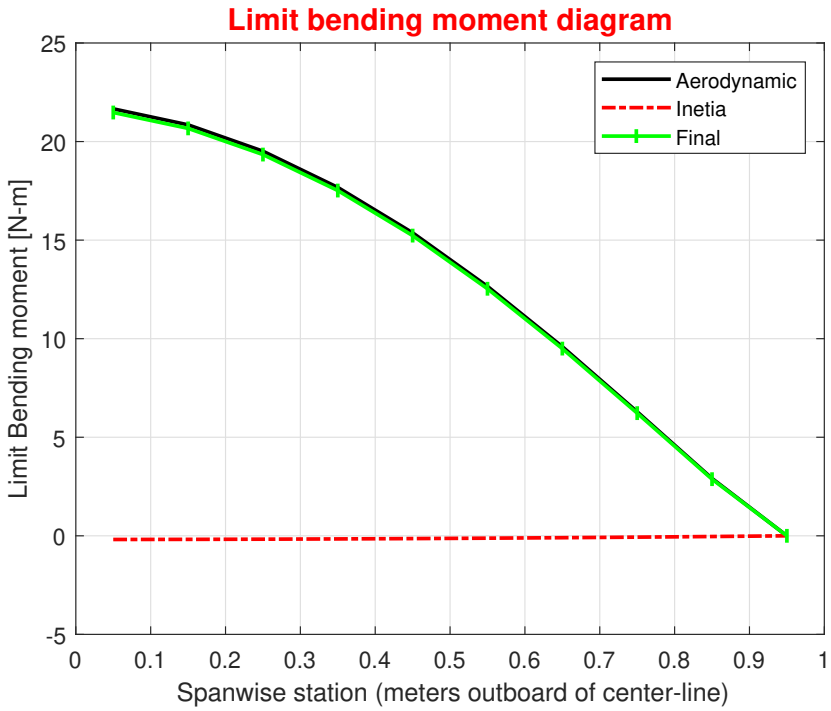

FIGURE 4.17: Ultimate bending moment diagram

4.5.2.2 Structual analysis using ANSYS ACP

The use of composite structures in UAV design is well-known for significantly reducing weight by 30–50%. By selecting different materials and lamination configurations, it is possible to tailor the strength and stiffness properties of composite structures to meet specific design requirements.

Our UAV wing utilizes a sandwich structure with XPS foam as the core material, three layers of glass fiber fabric as the composite layers, and a patch of carbon fiber at 25% of the chord. This design eliminates the need for traditional spars and ribs for our application, relying instead on the inherent high stiffness-to-weight ratio of the composite materials.

We investigated different ply configurations of glass fiber-reinforced plastic (GFRP) and carbon fiber-reinforced plastic (CFRP) to determine the most efficient configuration for weight reduction while maintaining structural integrity. The FEM analysis of the entire wing structure, including the XPS foam core and glass fiber layers, indicated superior stiffness compared to conventional designs. The wing redesign led to significant weight reduction, which will be detailed in a later section.

The optimized composite wing structure, comprising an XPS foam core and three layers of glass fiber fabric, demonstrates a high stiffness-to-weight ratio, making it an ideal choice for the fixed-wing UAV. The effect of various lay-up configurations on performance was also studied, confirming the advantages of the composite materials used in this design. Additionally, we checked for failure criteria of the wing using composite failure criteria such as the Tsai-Hill and Tsai-Wu criteria.

Initially, the wing geometry was imported into ANSYS ACP (Pre). Using SpaceClaim, a mold representing the wing surface was created. The wing structure was then segmented into 10 sections to facilitate the application of loading conditions. The load distribution across these segments was derived using Schrenk's approximation, providing a more realistic representation of aerodynamic loading for analysis.

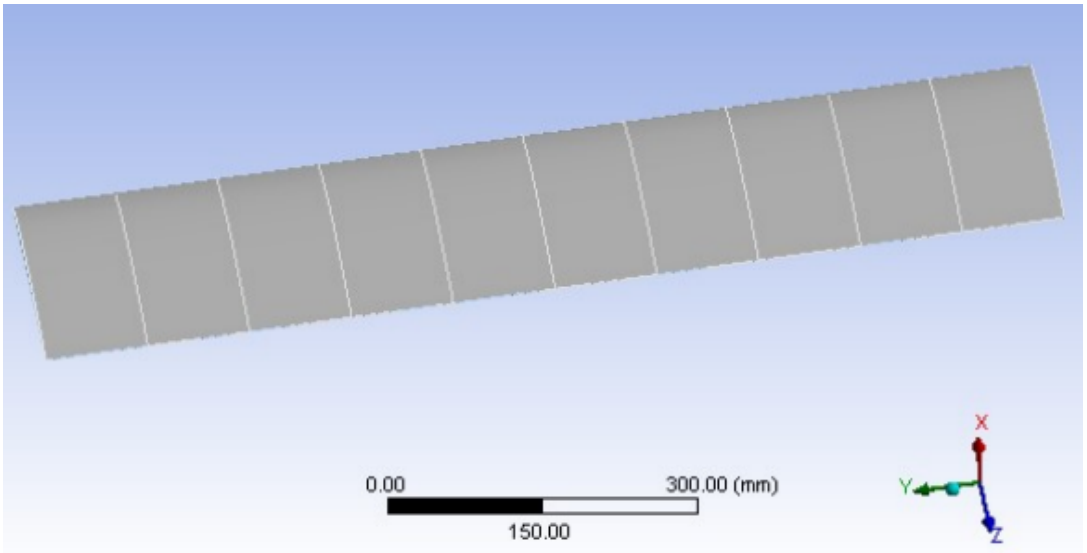

FIGURE 4.18: Wing surface divided into 10 segments for Analysis

For this analysis, we used two layers of wet epoxy carbon woven fabric (with an elastic modulus of 230 GPa) with a thickness of 0.5 mm, and one layer of wet epoxy E-glass fabric with a thickness of 0.3 mm. Additionally, a PVC foam core with a density of 60 kg/m^3 was incorporated in the analysis for inner core support. The key properties of the materials used are summarized in the table below.

Table 4.6: Material properties used in the structural analysis.

Sr.	**Material**	**Density** (**kg/m**^{3})	E_x, E_y, E_z **(GPa)**	$\nu_{xy}, \nu_{yz}, \nu_{zx}$
1	Epoxy Carbon Woven (230 GPa)	1451	59.16, 59.16, 7.5	0.04, 0.3, 0.3
2	Epoxy E-Glass Wet	1850	35, 9, 9	0.28, 0.4, 0.28
3	PVC Foam	60	0.07	0.3

Then a structured mesh was generated for the wing model with an element size of 15 mm, balancing computational efficiency and accuracy. The meshing process included adaptive sizing and high smoothing to effectively capture the wing's geometry. To further enhance the quality of the simulation, two inflation layers were applied with a smooth transition, ensuring proper resolution near the surface. The mesh underwent quality checks to verify its suitability for the analysis.

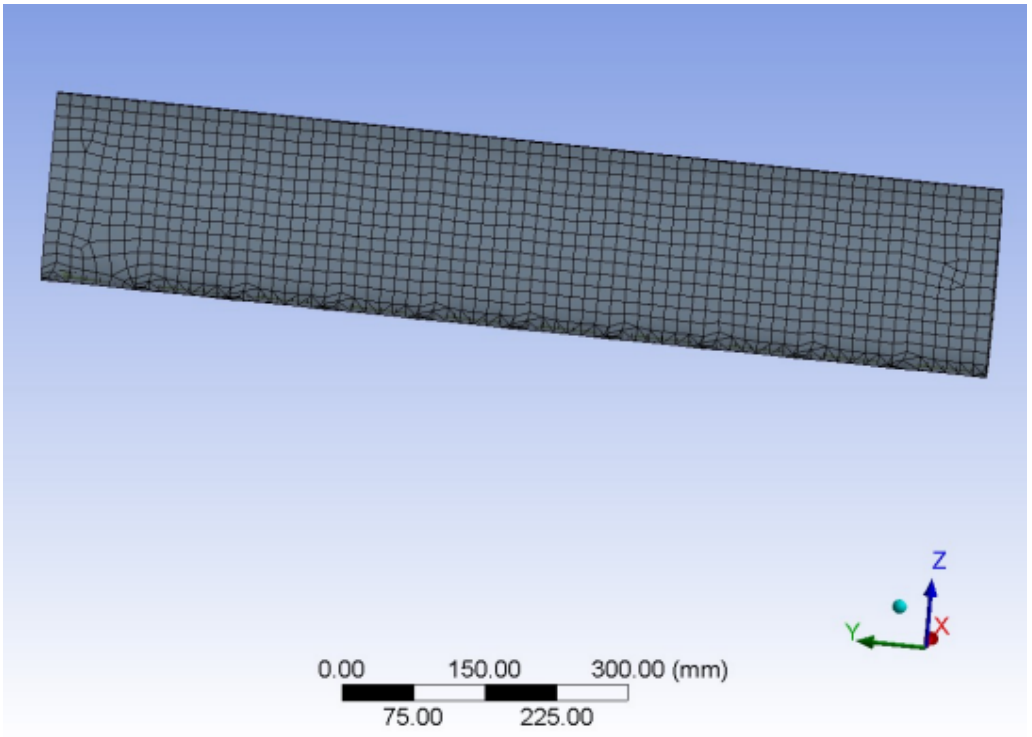

Figure 4.19: Mesh generated on wing surface

The elemental pressure distribution along the span of the wing, obtained from Schrenk's analysis, is illustrated in the figure below. This figure demonstrates the pressure variation applied to each segment along the wing's span, providing a detailed representation of the aerodynamic load distribution for further analysis.

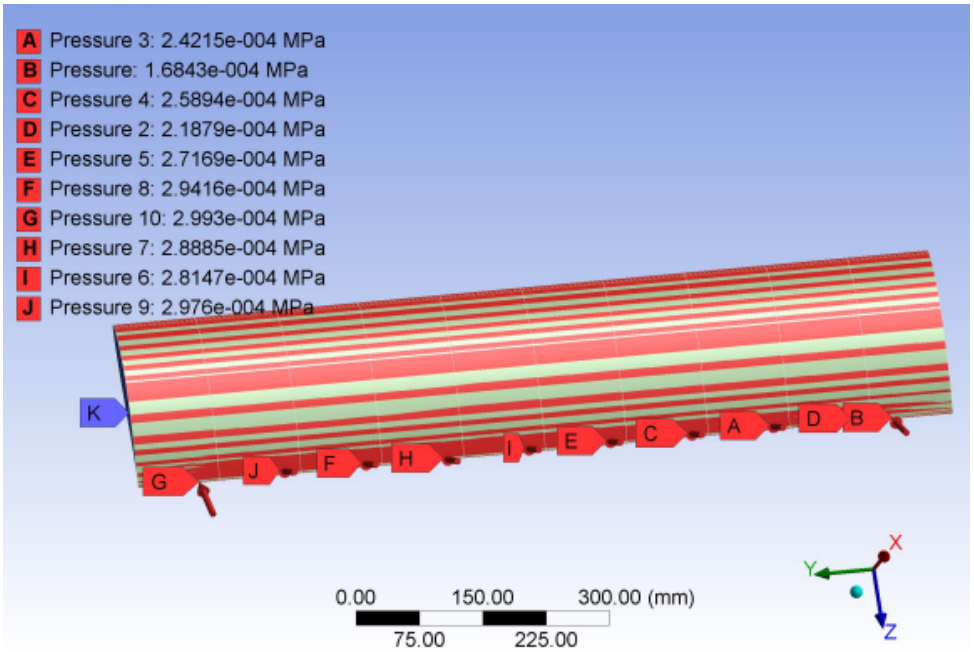

FIGURE 4.20: Boundary conditions applied in the Structural Analysis

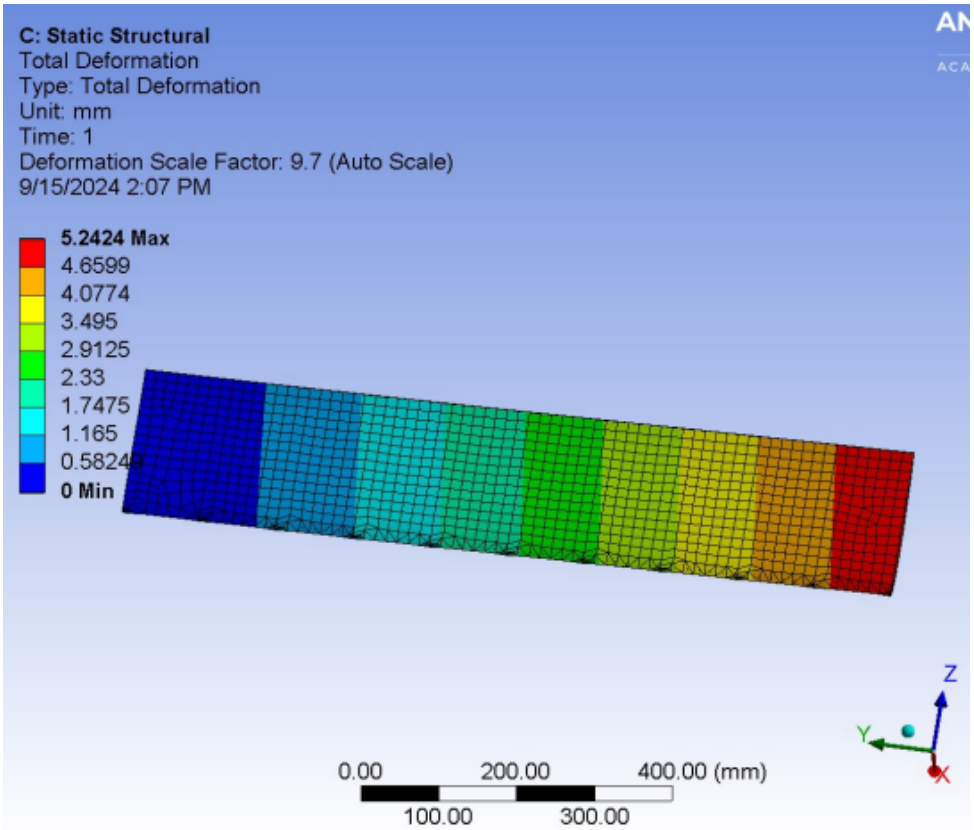

FIGURE 4.21: Total deformation

Using the specified constraints and boundary conditions, the analysis was performed, resulting in the following outcomes. The maximum total deformation observed was 5.24 mm, indicating the extent of displacement under applied loads. The maximum von Mises calculated was 22.36 MPa, which is significantly below the material's yield strength. This suggests that the design is structurally sound and well within the safety limits for the given loading conditions.

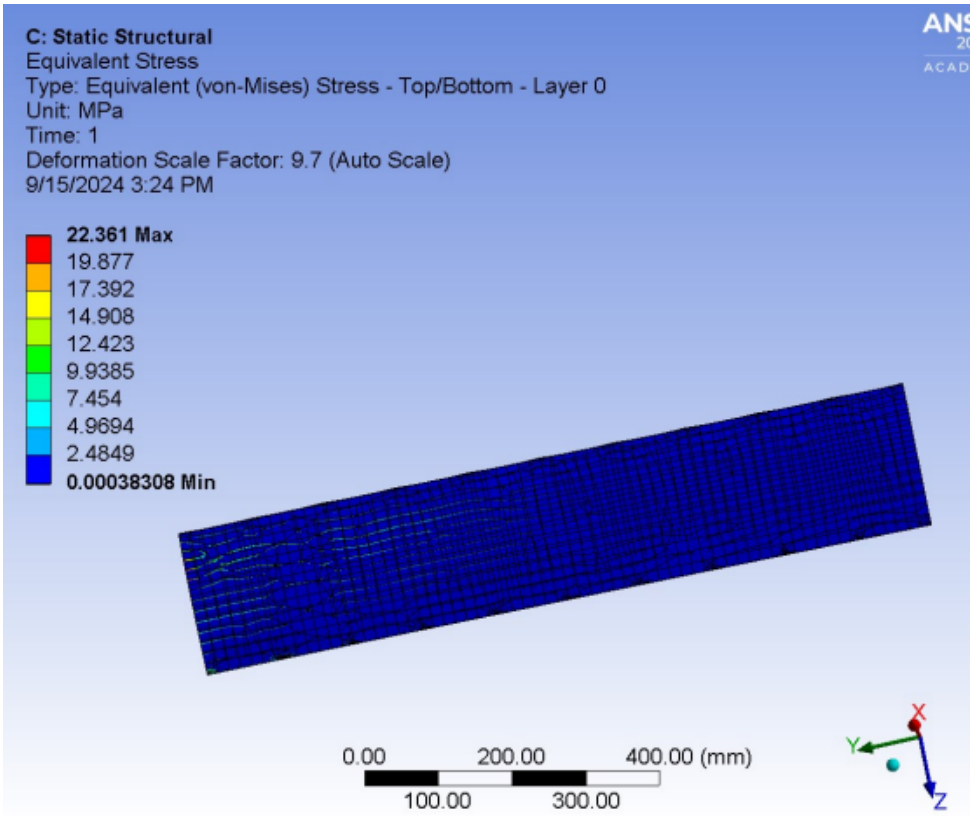

FIGURE 4.22: Equivalent (Von-mises) Stress

4.5.2.3 Failure analysis of composite Wing

Accurate prediction of failure in composite materials is essential due to their complex stress interactions. Two prominent failure criteria used for composite analysis are the **Tsai-Wu** and **Tsai-Hill** failure criteria. These criteria address the anisotropic nature of composites, which have different strengths in various directions due to their layered structures.

1. Tsai-Wu Failure Criterion

The Tsai-Wu failure criterion offers a comprehensive approach to predicting failure in composites by considering the interactions between different stress components. This criterion extends beyond traditional maximum stress and maximum strain theories to account for both tensile and compressive strengths in different directions.

The Tsai-Wu failure criterion is expressed as:

$$F_1\sigma_1 + F_2\sigma_2 + F_1\sigma_1^2 + F_2\sigma_2^2 + F_{11}\sigma_1^2\sigma_2^2 + 2F_{12}\sigma_1\sigma_2 + F_{66}\tau_{12}^2 \leq 1 \tag{4.12}$$

where:

- σ_1 and σ_2 are the normal stresses in the fiber and transverse directions.
- τ_{12} is the shear stress.
- F_1, F_2, F_{11}, F_{12}, and F_{66} are material constants derived from experimental data.

2. Tsai-Hill Failure Criterion

The Tsai-Hill failure criterion is a specific adaptation of Hill's criterion for composites. It provides a measure of failure based on the interaction of normal and shear stresses and is designed to predict failure when the combined stress state reaches a critical value.

The Tsai-Hill failure criterion is formulated as:

$$\frac{\sigma_1^2}{X_t^2} + \frac{\sigma_2^2}{Y_t^2} - \frac{\sigma_1\sigma_2}{X_tY_t} + \frac{\tau_{12}^2}{S_{12}^2} \leq 1 \tag{4.13}$$

where:

- σ_1 and σ_2 are the normal stresses.
- τ_{12} is the shear stress.
- X_t and Y_t are the tensile strengths in the fiber and transverse directions, respectively.
- S_{12} is the shear strength.

Analysis Results

In the FEM analysis conducted using ANSYS ACP, the Tsai-Wu and Tsai-Hill failure criteria were applied to the composite materials. The calculated values were **0.0986** for Tsai-Wu and **0.09585** for Tsai-Hill. Both values are significantly below 1, indicating that the stress states are well within safe limits. This confirms the structural integrity of the design under the applied loading conditions.

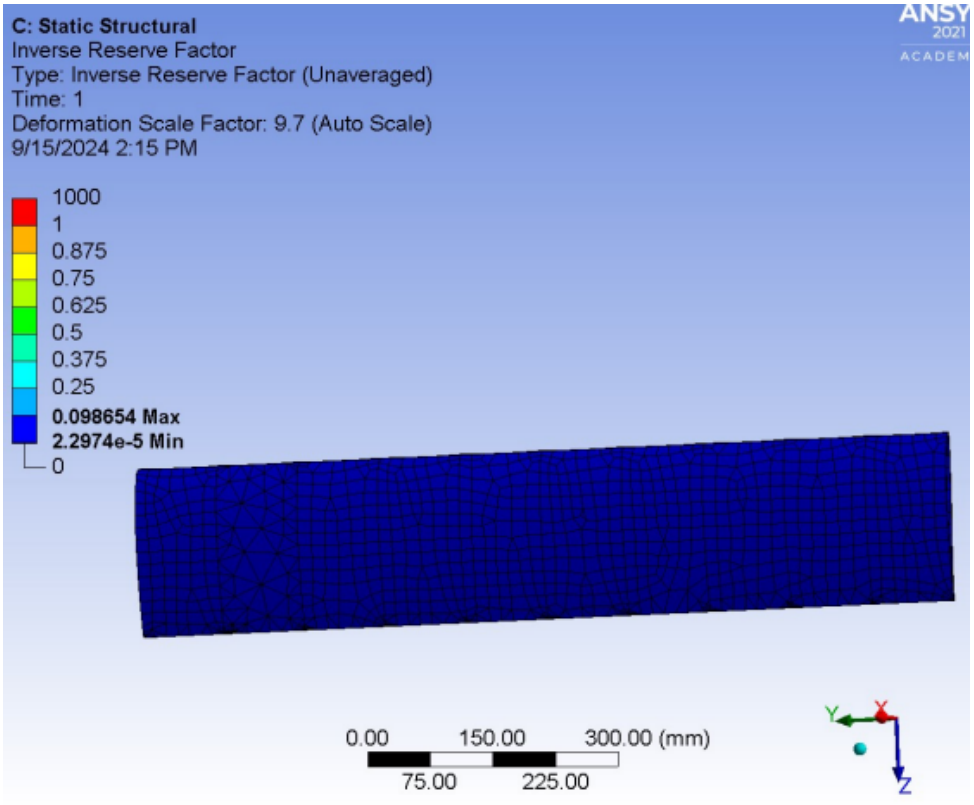

FIGURE 4.23: Results of Tsai-Wu Failure Criterion Analysis

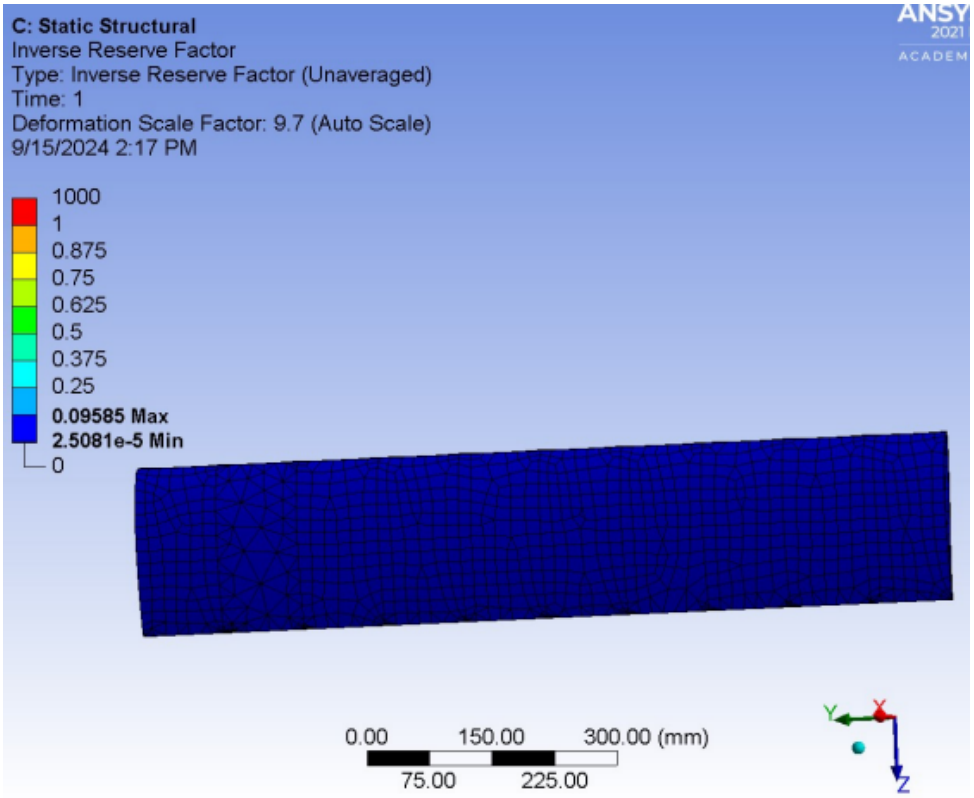

FIGURE 4.24: Results of Tsai-Hill Failure Criterion Analysis

In conclusion, the UAV wing design utilizing an XPS foam core, combined with layers of glass fiber and carbon fiber fabric, achieves significant weight reduction while enhancing structural integrity. This composite structure meets the necessary performance criteria for our UAV applications, providing a balance of lightweight characteristics and durability.

Chapter 5

Fuselage and Tail Design

Introduction to UAV Tail Design

In the realm of UAV design, the horizontal and vertical tails, along with the wing, are classified as lifting surfaces. However, the design philosophy for tails differs significantly from that of wings due to their distinct primary functions. While the wing's primary role is to generate maximum lift, the tail's function is to generate only a fraction of its potential lift. If a tail reaches its maximum angle of attack during any flight mission, it indicates a fundamental flaw in the tail design process.

A conventional UAV tail typically consists of two components: the horizontal tail and the vertical tail. These components fulfill three main functions:

1. **Trim (longitudinal and directional):** The horizontal tail ensures longitudinal trim, which refers to the UAV's balance or equilibrium, while the vertical tail provides directional trim.

2. **Stability (longitudinal and directional):** The horizontal tail contributes to longitudinal stability, and the vertical tail enhances directional stability.

3. **Control (longitudinal and directional):** The elevator, part of the horizontal tail, offers longitudinal control, whereas the rudder, part of the vertical tail, facilitates directional control.

The primary role of the horizontal tail is to maintain longitudinal trim, balancing the pitching moments generated by the wing's lift, aerodynamic pitching moment, and sometimes the engine thrust's longitudinal moment. Typically, these moments are negative, necessitating the horizontal tail to produce negative lift to counteract them.

Conversely, the vertical tail's primary function is to ensure directional stability, which is crucial due to the UAV's symmetry about the xz plane. The vertical tail balances the yawing moments about the UAV's center of gravity.

Control is another vital function of the tail. The elevator provides longitudinal control, allowing the UAV to change pitch, while the rudder offers directional control, enabling changes in yaw. The tail must be robust enough to manage these controls, allowing the UAV to transition smoothly between different flight conditions, such as from cruise to take-off or landing.

Our UAV employs a conventional tail configuration, often referred to as an inverted T-shape. This configuration is efficient in fulfilling all tail functions—trim, stability, and control. The horizontal tail, comprising two sections, is mounted on the aft fuselage and primarily addresses longitudinal trim and stability. The vertical tail, a single section also located on the aft fuselage, ensures directional trim and stability.

In summary, the design of the UAV's tail is driven by the need to achieve trim, stability, and control. The conventional tail configuration used in our UAV is straightforward to analyze and evaluate, providing a reliable and efficient solution for meeting these requirements.

5.1 Tail Design Parameters

After selecting the tail design configuration, the horizontal and vertical tail design parameters can be determined independently based on some statistical parameters, such as the horizontal tail volume ratio and vertical tail volume ratio, depending on the design configuration and requirements. These volume ratios are functions of the geometries of the respective parts of the tail.

The horizontal tail volume ratio, $\bar{V}_{\mathrm{H}}$, is crucial for ensuring longitudinal stability and trim. It influences the ability of the horizontal tail to balance pitching moments and provide adequate control authority for pitch maneuvers. In contrast, The vertical tail volume ratio, $\bar{V}_{\mathrm{V}}$, is important for directional stability and control. It affects the vertical

tail's ability to counteract yawing moments and provide sufficient control authority for yaw maneuvers.

Increasing the horizontal and vertical tail volume ratios generally enhances longitudinal and directional stability. However, this also tends to decrease the controllability of the respective axes.

The horizontal and vertical tail volume ratios are defined as follows:

$$\bar{V}_{\mathrm{H}} = \frac{l}{\bar{C}} \frac{S_{\mathrm{H}}}{S} \tag{5.1}$$

Here, $\bar{V}_{\mathrm{H}}$ denotes the horizontal tail volume ratio, l is the distance from the wing/fuselage aerodynamic center to the aerodynamic center of the horizontal tail, $\bar{C}$ is the mean aerodynamic chord of the wing, S_{H} is the area of the horizontal tail, and S is the wing area.

Similarly, the vertical tail volume ratio is defined as:

$$\bar{V}_{\mathrm{V}} = \frac{l_{\mathrm{V}}}{b} \frac{S_{\mathrm{V}}}{S} \tag{5.2}$$

Here, $\bar{V}_{\mathrm{V}}$ denotes the vertical tail volume ratio, l_{V} is the distance from the wing/fuselage aerodynamic center to the aerodynamic center of the vertical tail, b is the wingspan of the UAV, S_{V} is the area of the vertical tail, and S is the wing area.

The above aerodynamic center of the wing/fuselage combination refers to the wing's aerodynamic center, taking into account the aerodynamic effects of the fuselage.

For our application, we have chosen a horizontal tail volume ratio of 0.81 and a vertical tail volume ratio of 0.048. These parameters are referenced from [23].

The calculation of the tail moment arm and horizontal tail surface area is based on the following formulas from [23] and [19].

For the tail moment arm, which is the same for both the horizontal and vertical tails in this instance, we use:

$$l_{\mathrm{opt}} = K_{\mathrm{c}} \sqrt{\frac{4\bar{C}S\bar{V}\mathrm{H}}{\pi D \mathrm{f}}} \tag{5.3}$$

Here, K_c is the correction factor depending on the shape of the aft portion of the fuselage, which we have taken as 1.2 in our case, and D_f is the maximum diameter of the aft portion of the fuselage, which we have taken as 0.2 m. The other variables are self-explanatory.

Using Equation for moment arm calculation, we obtained the optimum tail moment arm as 0.78 m.

To calculate the tail surface area, we used the following formulas:

For the horizontal tail:

$$S_{\mathrm{h}} = \frac{\bar{V}_{\mathrm{H}}\bar{C}S}{l} \tag{5.4}$$

For the vertical tail:

$$S_{\mathrm{v}} = \frac{b \cdot S \cdot \bar{V}\mathrm{v}}{l\mathrm{v}} \tag{5.5}$$

After calculating the surface area and tail moment arm, we obtained the required geometric parameters.

Table 5.1: Horizontal tail specification

Span	0.60 m
Aspect Ratio	4.3
Airfoil	NACA 0009
Plan-form area	0.08 m^2
Volume ratio	0.81
Taper Ratio	0.56

Table 5.2: Vertical tail specification

Surface Span	0.32 m
Aspect Ratio	8
Airfoil	NACA 0009
Plan-form area	0.05 m^2
Volume ratio	0.048
Taper Ratio	0.45

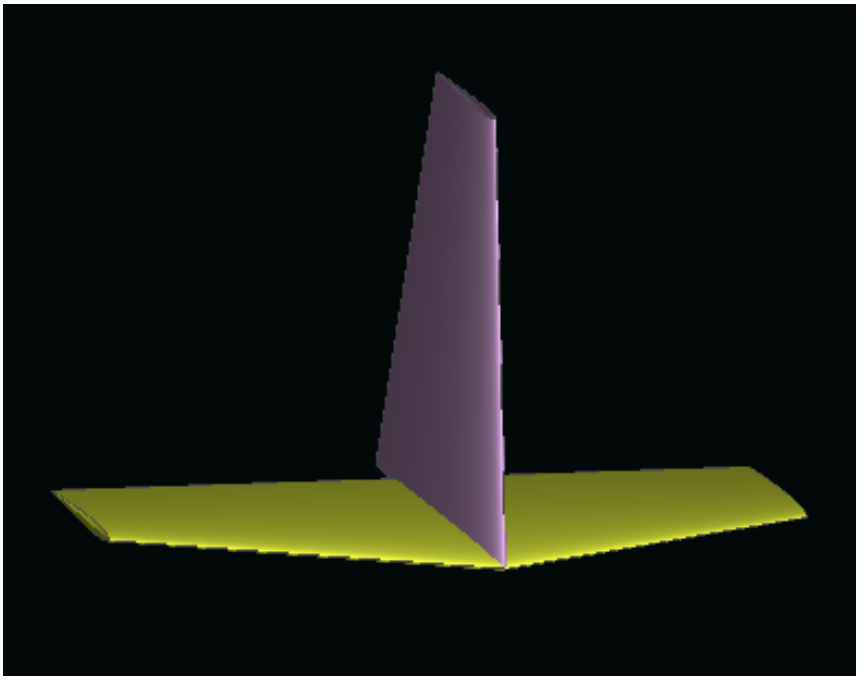

FIGURE 5.1: Final Tail layout from XFLR5

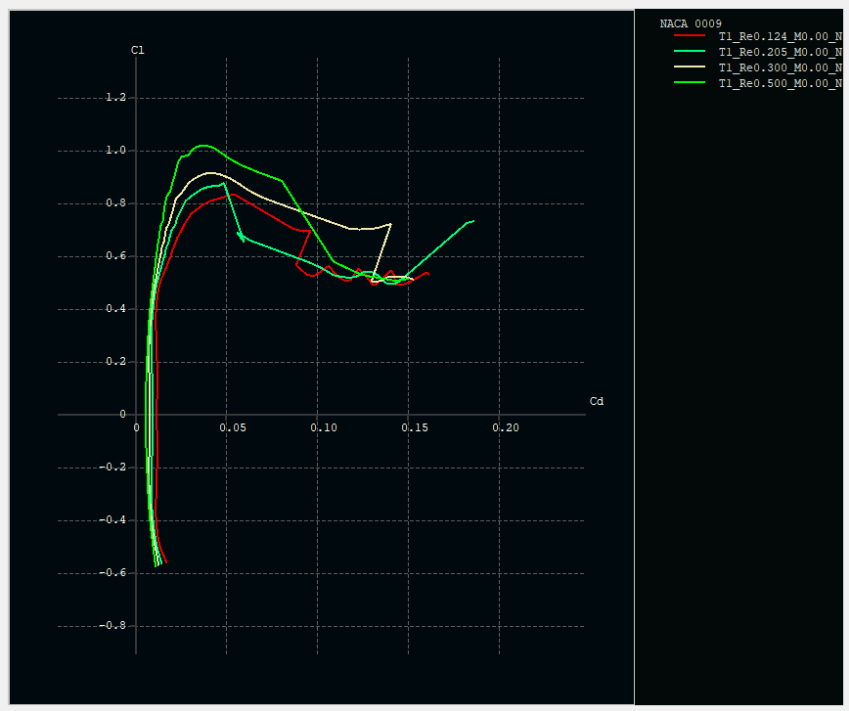

FIGURE 5.2: Drag polar for Tail airfoil

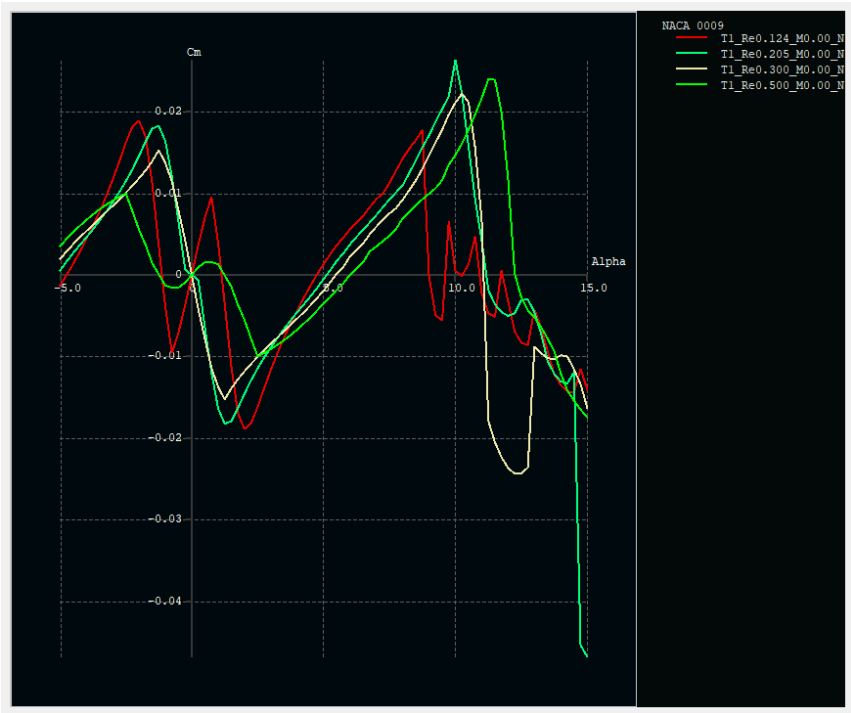

FIGURE 5.3: Coeff. of moment Vs α (Angle of attack)

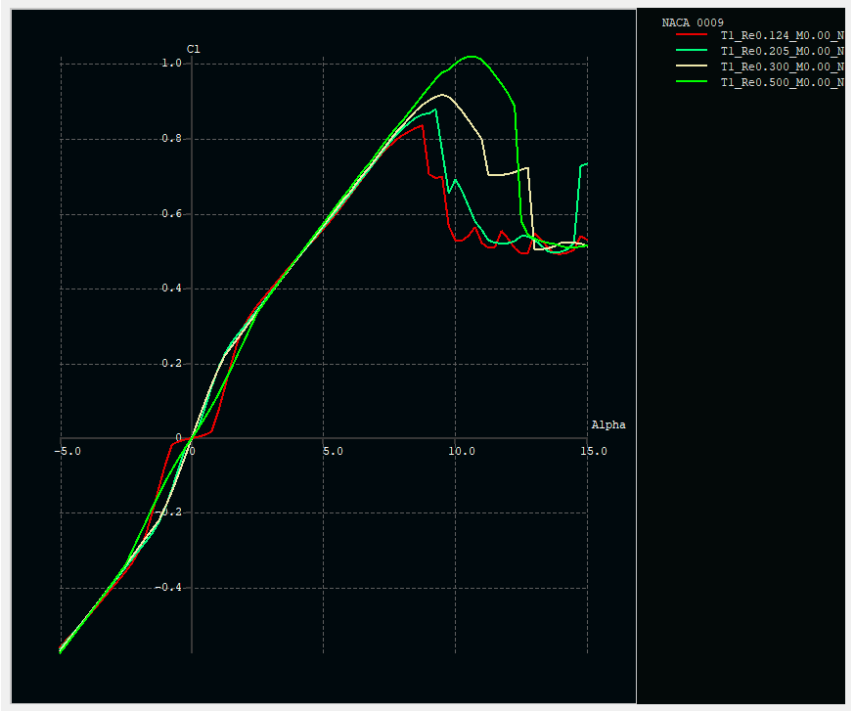

FIGURE 5.4: Coefficient of lift vs α (AOA) for Tail airfoil

5.2 Fuselage Design Parameters

For our application, the fuselage needs to be as streamlined and lightweight as possible. To achieve this, the front portion of the fuselage is used for the placement of the battery, avionics, and other related components. The rear part of the fuselage utilizes a carbon fiber tube with a diameter of 16 mm.

The aerodynamic requirements for the external fuselage shape are:

- Low aerodynamic drag
- Zero rolling and yawing moments
- Low pitching moment
- Maximizing lift generation

To start the construction, we calculated the length of the fuselage based on the ratio of the tail moment arm to the total length of the fuselage, denoted as $\frac{l}{L}$. For our design, this ratio is 0.6.

The calculation is as follows:

$$L = \frac{l}{0.6} \tag{5.6}$$

Given that the tail moment arm (l) is 0.78 m:

$$L = \frac{0.78}{0.6} = 1.3\,\mathrm{m} \tag{5.7}$$

Based on the requirements for battery, avionics box, and payload accommodation, we have selected the following geometry for the fuselage, which is illustrated in the following figure.

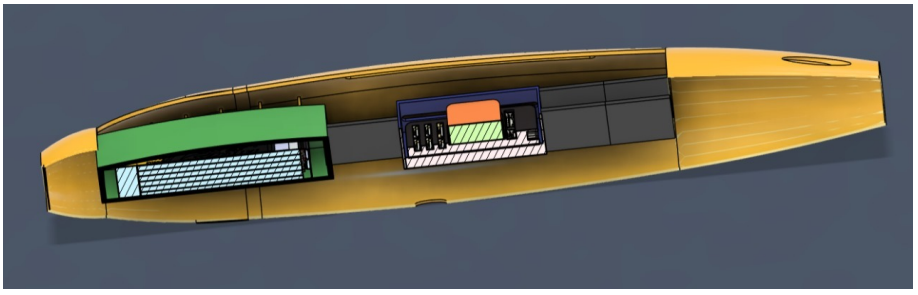

FIGURE 5.5: Sectional view of Front fuselage

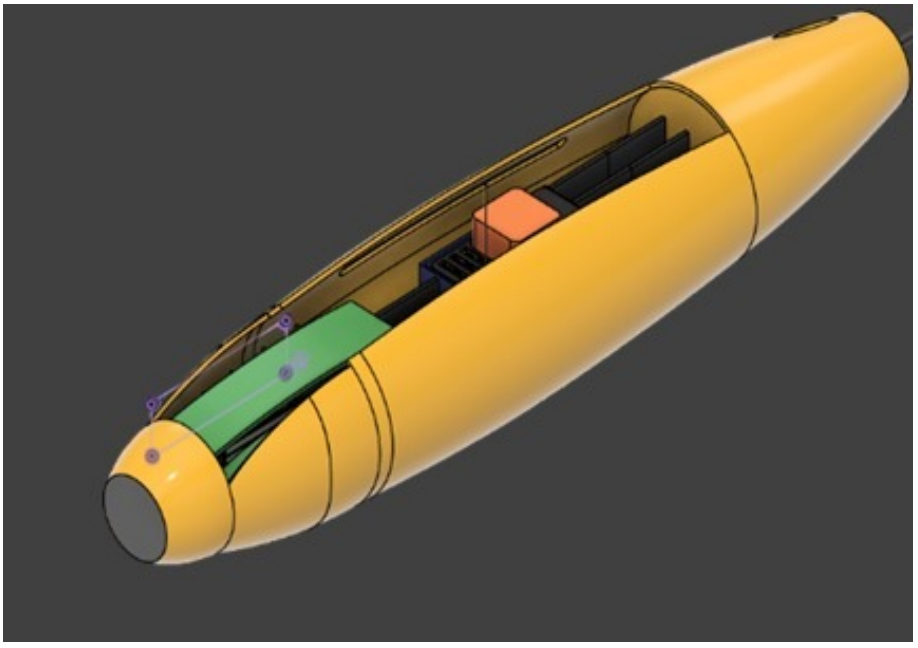

FIGURE 5.6: Front fuselage isometric view

FIGURE 5.7: Complete fuselage With Tail Assembly

5.3 Propulsion System Selection

Based on our calculations for power loading and wing loading in Chapter 3, we can now select the appropriate propulsion system for our UAV.

As observed in Figure 3.12, the power loading $\left(\frac{W}{P}\right)$ for our UAV is $0.1\frac{N}{W}$, and our calculated power requirement is 315 Watts.

Historically, a general rule of thumb is to account for all idealized variables in the design by multiplying the power requirement by a factor of 2. This means our propulsion system should be capable of generating at least 315 Watts at 50% of its capacity.

The above propulsion requirement is the theoretical power requirement; however, in practice, the components of the propulsion system have their respective component-level efficiencies.

Therefore, our propulsion system must be designed to produce a minimum of 630 Watts to ensure optimal performance and reliability under various conditions.

Based on our mission requirements and given weight constraints, electric propulsion emerged as the best possible choice. The figure below illustrates the schematics of the electric propulsion system in our UAV design.

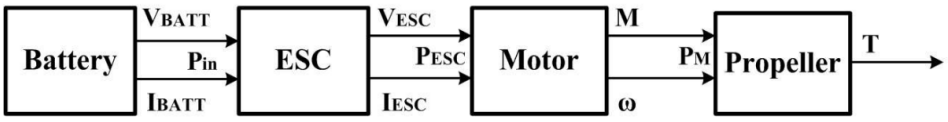

FIGURE 5.8: Electric propulsion system

The figure above presents the four major components of the electric propulsion system: the Battery, Electronic speed controller (ESC), Electric motor, and Propeller.

5.3.1 Selection of Motor

Two types of electric motors are commonly used in UAV applications: 1) Brushed DC motors and 2) Brushless DC motors. Brushless DC motors are generally preferred in UAV applications where the thrust requirement exceeds 50 grams.

Brushless DC motors are favored due to their operational efficiency and low internal friction. In BLDC motors, the stator comprises wire coils that induce magnetic fields, while the rotor holds permanent magnets. Because the polarity of the stator coils is phased electronically, metal brushes are not needed to phase the current, thereby mechanically reducing friction [29].

Based on our requirements, the specifications of the selected motor are given in the Table 5.3.

5.3.2 Selection of Electronic speed controller

The Electronic Speed Controller (ESC) plays a crucial role in linking the motor with the onboard autopilot system [29]. It interprets digital signals from the autopilot to regulate the motor's power, speed, and direction, and can also function as a dynamic brake. While both BLDC and brushed motors use ESCs, their operation differs slightly. For BLDC motors, the ESC is responsible for converting DC voltage into three-phase power using a series of MOSFETs and diodes, which manage the power switching between phases. This switching process can cause electrical losses, primarily as heat, which reduces the system's efficiency [30].

Since our motor has a peak current value of 57 amperes, we chose an ESC with a maximum current rating higher than the motor's peak current capacity. The AT Series ESCs have demonstrated reliability over the years, making the AT 75 ESC a suitable choice for our application. Again the specification of the selected Electronic speed controller is gievn in the Table 5.3.

5.3.3 Selection of Propeller

A UAV propeller is essentially a series of rotating wings or airfoils that converge at a central point called the hub. The hub is connected to the motor shaft, which converts electrical energy into mechanical energy. The propeller then converts the motor's torque into thrust by utilizing the incoming airflow.

The combination of the aircraft's forward velocity and the rotational velocity of the propeller creates a relative wind, which is encountered by the propeller blades. As the propeller rotates, each blade follows a spiral path, resulting from the simultaneous forward

and rotational motion—similar to the movement of a screw. Notably, a point near the tip of a blade covers a larger distance than a point near the shank due to this motion.

Propeller selection is based on the power generation capability and the specific performance requirements of the vehicle. The propeller serves as the interface that transfers the motor's power to thrust, which is crucial for the UAV's performance.

A total of three propellers were compared at the same RPM for use with our UAV, ensuring that all propellers met the thrust requirement at 8000 RPM. The propellers' efficiencies, measured in grams per watt ($\frac{Gram}{Watt}$), were compared at the same advance ratio and RPM. The results showed that as the diameter and pitch of the propellers increased, their efficiency decreased. Additionally, the power requirement increased with the size of the propeller.

Our motor can produce the required thrust and power with all these propellers at 7000 RPM hence will compare these propellers at this particular RPM.

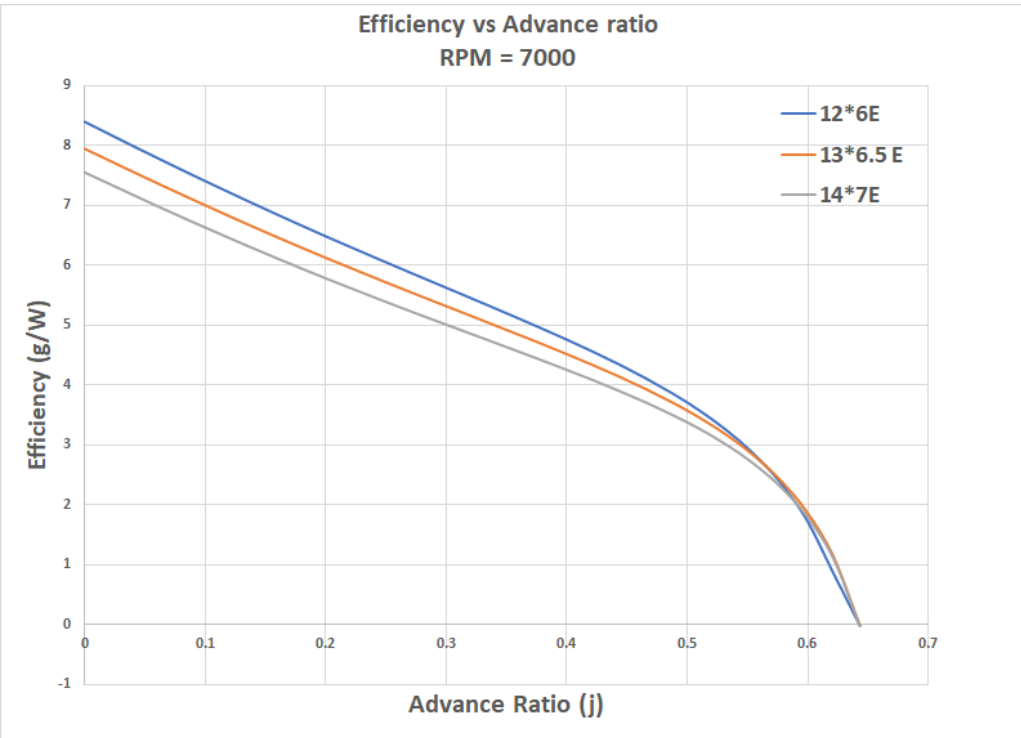

FIGURE 5.9: Propeller comparison

TABLE 5.3: Specifications of the propulsion system components

Component	Image	Specifications
Motor		**Model**: AT 2826 **KV rating**: 900 kv **Weight**: 175 grams **Shaft diameter**: 5 mm **No of cells**: 3 – 4 S **Maximum power**: 820 W
ESC		**Model**: AT 75 ESC **Max. cont. Current**: 75 A **Burst Current**: 95 A **Weight**: 82 grams **Number of cells**: 2-6 S
Propeller		**Model**: APC Thin electric **Weight**: 45 grams **Diameter**: 12” **Pitch**: 6”
Battery		**Model**: Maxamps LiPo **Cells**: 4S **Volts**: 14.8 V **Capacity**: 1100 mAh **Weight**: 850 grams **Energy density**: 192 Wh/kg

5.3.4 Selection of Battery

Due to the high endurance and range requirements of our mission, the onboard energy demand was also significant. Therefore, we needed a battery with high energy density to provide the desired flight time and range.

In UAVs, LiPo (Lithium Polymer) and Li-ion (Lithium-ion) batteries are commonly used because of their high energy density and performance in high amp draw applications. We chose a LiPo battery for our specific needs, as it can deliver the necessary power and energy capacity to meet our flight duration and range objectives. LiPo batteries are particularly advantageous in scenarios where weight is a critical factor, as they offer a favorable energy-to-weight ratio, making them an ideal choice for UAV applications. Specifications of the battery is given in the Table 5.3.

Chapter 6

Stability analysis

In this chapter, we will focus on the UAV's static stability analysis, particularly addressing static longitudinal stability and the static margin. Static stability is essential for ensuring that the aircraft can return to equilibrium after a disturbance without requiring constant control inputs. The static margin provides a measure of how stable or unstable the UAV is.

6.1 Static Longitudinal Stability

Static longitudinal stability refers to the aircraft's tendency to restore itself to a trimmed flight condition after a disturbance in pitch. The fundamental equation governing static longitudinal stability is given by:

$$C_m = C_{m_0} + \frac{dC_m}{d\alpha} \cdot \alpha \tag{6.1}$$

here

$$C_{m_0} = C_{m_{0_w}} + C_{m_{0_f}} + \eta V_H \cdot C_{L_{\alpha_t}}(\epsilon_0 + i_w - i_t) \tag{6.2}$$

and

$$C_{m_\alpha} = C_{L_{\alpha_w}} \left(\frac{X_{cg}}{\bar{c}} - \frac{X_{ac}}{\bar{c}} \right) + C_{m_{\alpha_f}} - \eta V_H \cdot C_{L_{\alpha_t}} \left(1 - \frac{d\epsilon}{d\alpha} \right) \tag{6.3}$$

For static longitudinal stability, the stability derivative $\frac{dC_m}{d\alpha}$ must be negative, and C_{m_0}, the coefficient of moment at zero angle of attack, must be positive.

After doing the analysis using XFLR5 software we have found the following.

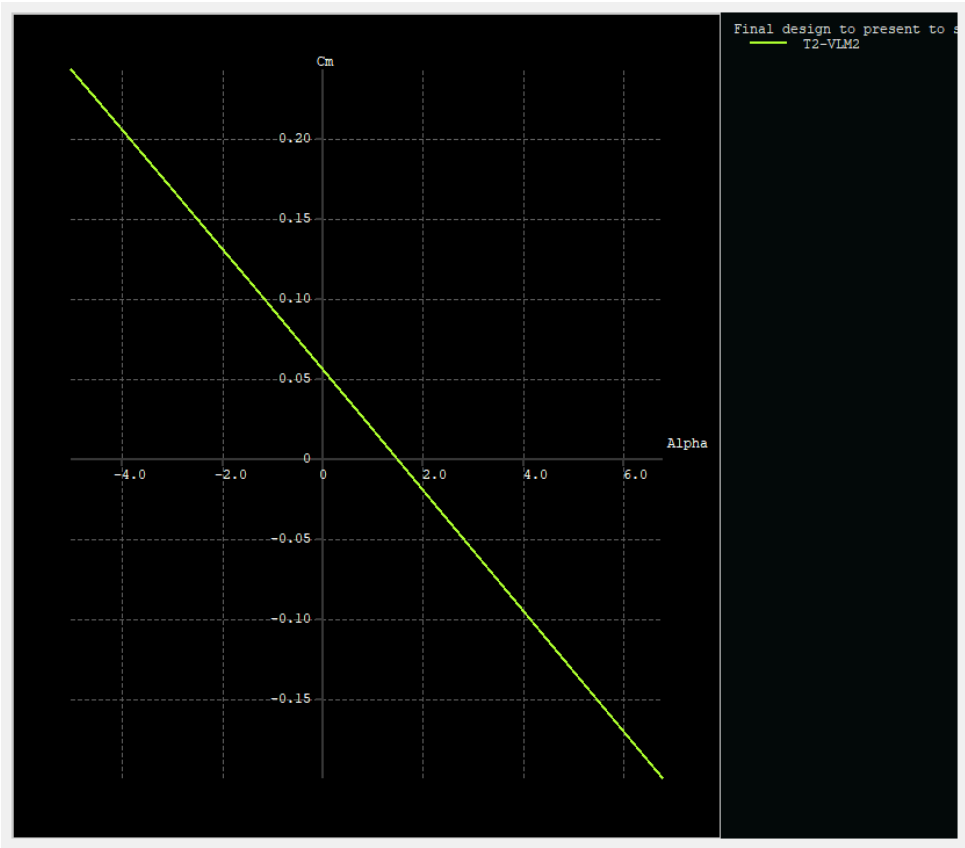

FIGURE 6.1: Cm Vs Alpha plot obtained from XFLR5

In the graph presented earlier, it can be observed that the slope of the plot is negative, while the intercept on the Y-axis is positive, satisfying the condition for longitudinal stability.

6.2 Static Margin and Neutral point Estimation

The static margin is a dimensionless parameter that quantifies the stability margin of the UAV. It is expressed as:

$$\text{Static Margin} = \frac{X_{cg} - X_{np}}{c} \tag{6.4}$$

Where:

- X_{cg}: Location of the center of gravity (CG)
- X_{np}: Neutral point, the aerodynamic center where the pitching moment is zero
- c: Mean aerodynamic chord

A positive static margin indicates a stable configuration, while a negative value suggests instability.

Using XFLR5 software, we calculated the center of gravity (CG) to be located at 100 mm, and the neutral point (NP) at 137 mm from the wing's leading edge. With the mean aerodynamic chord (MAC) of 200 mm, we can determine the static margin using the formula:

$$\text{Static Margin} = \frac{X_{NP} - X_{CG}}{\bar{c}} \times 100$$

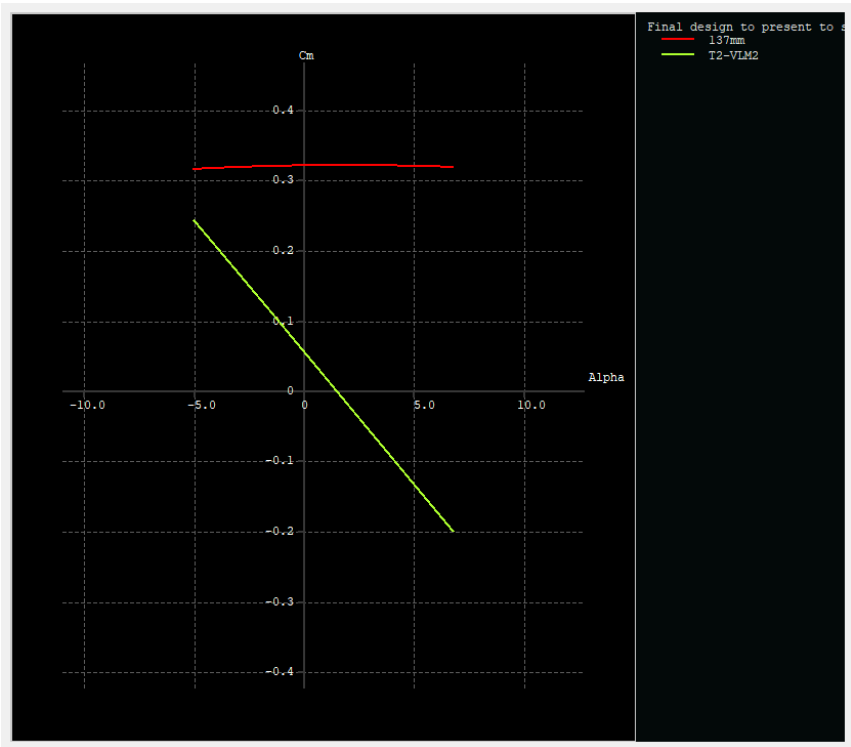

FIGURE 6.2: Variation of Cm Vs Alpha plot for UAV with CG location obtained from XFLR5

Substituting the values:

$$\text{Static Margin} = \frac{137\,\text{mm} - 100\,\text{mm}}{200\,\text{mm}} \times 100 = 18.5\%$$

The static margin is approximately 18.5%, which is favorable for longitudinal stability, as a positive static margin ensures that the aircraft will exhibit stable behavior.

Chapter 7

Manufacturing Process

7.1 Introduction

In this chapter, we detail the manufacturing processes employed for fabricating the UAV components using composite materials. Composites were selected for their ability to create lightweight structures while offering a high strength-to-weight ratio.

The fuselage is composed of a combination of glass fiber and carbon fiber, with the aft section utilizing a carbon fiber tube to significantly reduce weight. The wing structure is similarly constructed from glass fiber and carbon fiber, ensuring both strength and structural stability. Carbon fiber fabric is strategically placed at the quarter-chord (C/4) section of the wing to enhance strength for screw attachments and to function as a spar across the span.

For the tail, a combination of glass fiber and XPS foam was used. The XPS foam serves as the core in a sandwich structure, while glass fiber forms the outer skin, providing the necessary strength to the tail and wing components.

Manufacturing processes were carried out at the Composite lab in the Helicopter building facility at IIT Kanpur. A gravity-fed hot wire cutter was used to shape the XPS foam into the desired wing and tail profiles. The hand lay-up method was employed for constructing the wing and tail sections, while vacuum bagging was used to cure these parts, ensuring optimal material consolidation and strength.

Additionally, 3D printing technology was utilized to produce various smaller and customized parts, such as the GPS mount, aft tail boom joint, antenna mounts, and other

components. These were printed using ABS and PLA materials, contributing to the overall efficiency and customization of the UAV's design.

7.1.1 Brief Introduction to composite Material

Composite materials are engineered materials made from two or more constituent materials with significantly different physical or chemical properties. When combined, they produce a material with characteristics different from the individual components. Composites are particularly valued in industries where strength-to-weight ratio, durability, and resistance to environmental factors are crucial. The fibers in a composite material provide the primary structural strength, carrying the load and giving the material its high tensile strength and stiffness. The matrix binds these fibers together, transferring loads between them, protecting them from environmental damage, and maintaining the material's shape. Composite materials are categorized based on the type of reinforcement used. The primary classifications include fibrous composites, particulate composites, flake-based composites, and whisker-based composites.

7.1.1.1 Fibrous Composites

Fibrous composites consist of fibers embedded within a matrix material. The fibers can be either short, chopped fibers or continuous fibers. Short fibers provide ease of processing and are often used in applications where complex shapes are required, but they typically offer lower mechanical properties compared to continuous fibers. Continuous fibers, on the other hand, are long and unbroken, providing superior mechanical strength and stiffness.

In our UAV's manufacturing process, we employed long continuous bidirectional fibers with a 0/90-degree orientation, specifically carbon and glass fibers. These fibers, available in weights of 50, 100, and 250 GSM, were chosen for their exceptional strength-to-weight ratio and their ability to provide structural stability across the UAV components.

7.1.1.2 Particulate Composites

Particulate composites consist of particles dispersed within the matrix. These particles can be metals, ceramics, or polymers, providing enhanced properties such as increased stiffness or wear resistance.

7.1.1.3 Flake/Whisker-Based Composites

Flake-based composites involve the use of flake-shaped particles as the reinforcement within the matrix, while whisker-based composites utilize tiny, hair-like structures called whiskers. Both flakes and whiskers improve mechanical properties by enhancing dimensional stability and offering high strength and stiffness.

7.1.2 Laminate Composites

Laminate composites are made by bonding multiple layers of material, known as laminates, with a matrix to enhance mechanical properties. In our UAV, we used laminate composites by stacking bidirectional woven fabric, with each layer oriented to optimize strength and stiffness.

For our UAV, we employed the laminate composite technique in constructing the wing, tail, and fuselage. The bidirectional woven fabric was sequentially stacked using the hand layup process, with the matrix acting as the binding agent between layers.

7.2 Hand Layup Process

The hand layup process is a critical step in the manufacturing of composite parts for our UAV. Achieving the correct ratio of resin to hardener at a specific temperature is essential, but equally important is the skill of the technician applying these materials.

In this process, fibers are first placed in a mold, followed by resin layup over the woven fabric using a paintbrush, and then resin impregnation is performed using a roller. For our application, we use epoxy resin, specifically diglycidyl ether of bisphenol-A (DGEBA), combined with a hardener, methyl tetrahydrophthalic anhydride (MTHPA), in a 1:3 ratio.

One of the main challenges of the hand layup process is ensuring uniform distribution of the resin and hardener, which largely depends on the expertise of the technician. Generally, after the hand layup process, the composite is cured under standard atmospheric conditions. However, in our case, to remove excess matrix material, we employ vacuum bagging to cure the composite, ensuring a more consistent and high-quality final product.

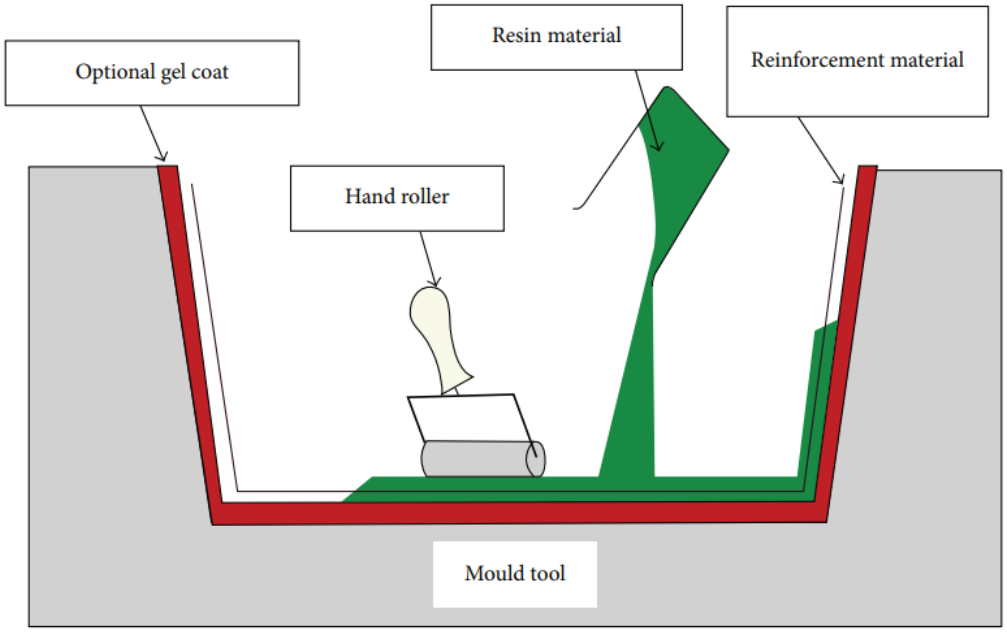

FIGURE 7.1: Hand lay-up process (Udupi,Rodrigues)

7.3 Vacuum Bagging Process

The vacuum bagging process is an advanced extension of the wet layup technique, widely used in composite manufacturing to improve the quality and performance of laminated parts. In this method, the laminated composite part is first wraped using some release fabric or thin mylar sheet then a perforated Film is wrapped over the release filem or sheet which is then again wrapped with a Breather material and then it is sealed within a nylon or plastic bag to create a controlled vacuum environment.

Initially, the fiber and matrix materials are laid up using a brush to ensure thorough impregnation of the resin. Once the layers are appropriately arranged, the lamination area is enclosed using silicone tape, and a vacuum pump is used to evacuate the air via a hose connected to the sealed bag. Before sealing the composite, a thin release film is wrapped around the laminated part to prevent the resin from sticking to the bagging material. A breather cloth is then applied over the entire wrapped part to allow for even air distribution during the vacuum process.

The vacuum pump removes trapped air from within the laminate, reducing voids and ensuring a uniform resin distribution. This process not only enhances the strength and

structural integrity of the composite material by eliminating air bubbles and ensuring consistent laminate thickness, but also results in a higher fiber content, leading to improved mechanical properties. However, vacuum bagging involves increased complexity, higher costs, and longer setup times compared to wet layup.

A schematic view of the vacuum bagging process and its components is given below,

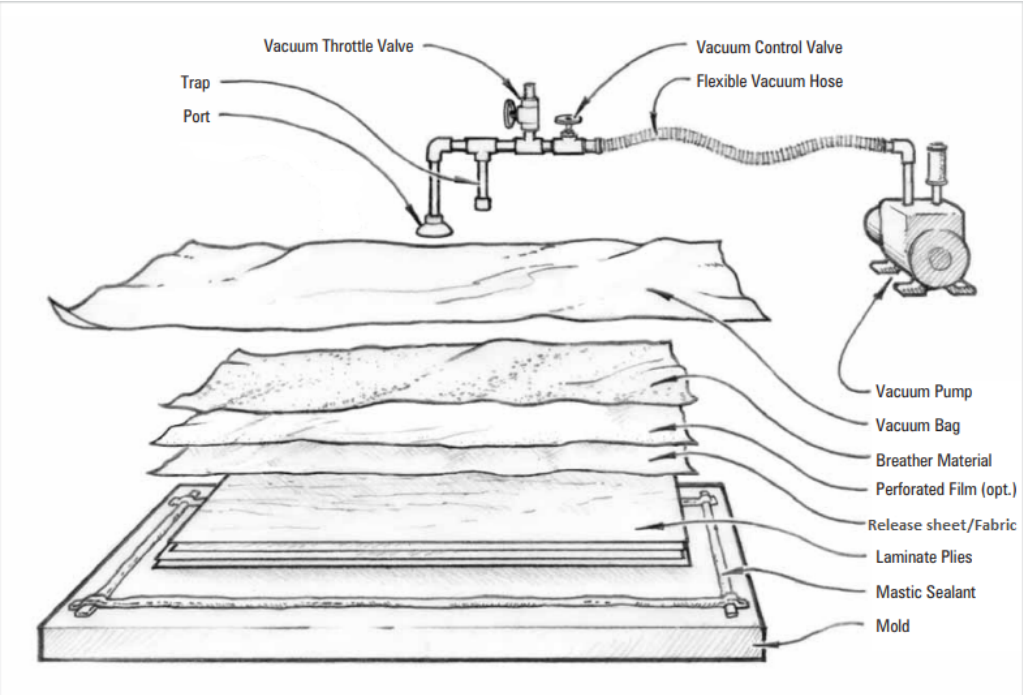

FIGURE 7.2: Typical components of a vacuum bagging system.

7.4 Manufacturing of Wing

In this section, we describe the manufacturing process of the wing, which is composed of glass fiber, carbon fiber, and XPS foam as the core material.

The process begins by cutting a thick paper sheet into the shape of the E214 airfoil profile. This paper template is then adhered to both sides of the XPS foam block. The adhesive secures the template, allowing for precise cutting using a hot wire cutter. The hot wire cutter is guided along the template edges, shaping the foam into the desired wing profile.

This step provides the basic shape of the wing. To achieve the full span of the wing, the core is initially cut into smaller sections. These sections are easier to handle and shape

individually. During the subsequent stages of manufacturing, these smaller sections are carefully joined together to form the complete wing structure.

The wing will be further refined and strengthened in the later stages, incorporating layers of glass fiber and carbon fiber to enhance its structural integrity and performance.

FIGURE 7.3: XPS block cross section with profile cut

FIGURE 7.4: XPS foam Wing profile

The wing manufacturing process begins with the preparation of the XPS core Fig[7.4], followed by composite lamination. The first step is to cut a mylar sheet, ensuring its width matches or exceeds the length of the airfoil curve, and its length covers the entire span of the wing. This sheet will wrap around the entire XPS core, providing a smooth surface for the lamination process.

Before starting the lamination, wax is applied to the mylar sheet to act as a release agent. After waxing, the desired color spray is applied, which will give the wing its final appearance.

Next, the lamination process begins directly on the mylar sheet. A 50 GSM bidirectional glass fiber woven fabric is placed first. The matrix, consisting of epoxy resin and hardener, is then applied using a brush and nip roller to ensure thorough impregnation of the fabric. This process is repeated for two additional layers of glass fiber woven fabric, with the subsequent layers being 100 GSM and 250 GSM, respectively.

After the glass fiber layers are stacked, a carbon fiber patch is applied along the span of the wing at the leading edge and at the quarter chord point. This patch enhances the structural integrity of the wing, particularly where the highest bending stresses occur.

The entire span, along with the mylar sheet, is then wrapped with the composite fabric. This assembly is followed by the application of a perforated release film and a breather cloth to facilitate the vacuum bagging process.

During vacuum bagging, the composite assembly is cured under controlled conditions. Once the curing process is complete, the breather cloth and mylar sheet are removed, revealing the finished wing with the desired surface finish and structural properties.

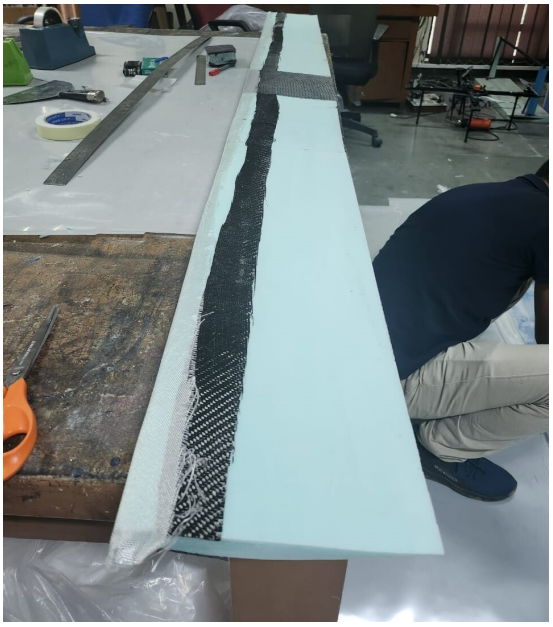

FIGURE 7.5: Leading Edge and Quarter Chord Patches

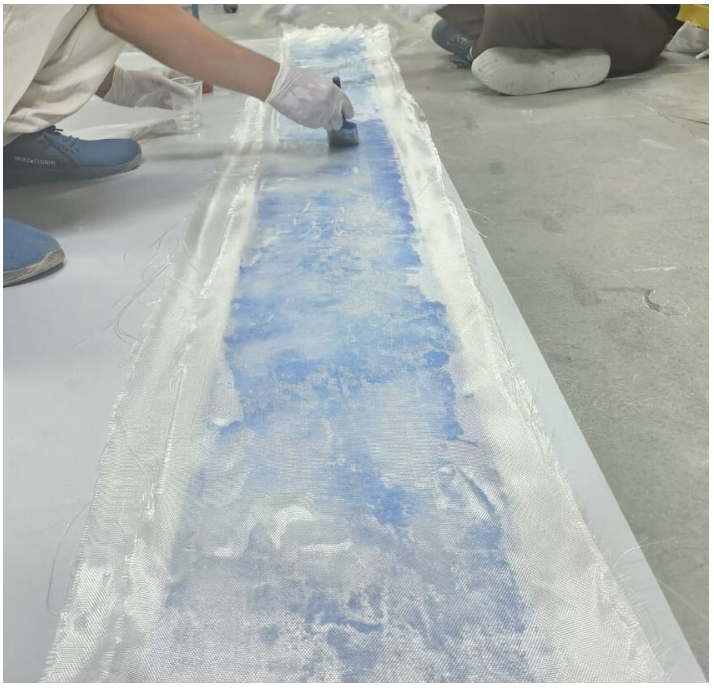

FIGURE 7.6: Fiber Stacking in Wing Assembly

FIGURE 7.7: Vaccum bagging of the wing

7.5 Manufacturing of Fuselage

The manufacturing process begins by cutting a series of conical pieces from XPS foam, each with a different diameter on either side. These pieces are then arranged and assembled sequentially, using CAD software to guide the creation of the desired fuselage shape. Once the arrangement is completed and verified for accuracy, the conical pieces are carefully stacked together to form the full fuselage structure.

After shaping the XPS foam core, the next step involves precisely measuring the required length and width of the glass fiber needed for stacking. A mylar sheet is prepared by applying a uniform layer of wax, followed by the desired color spray to achieve the final appearance. The glass fiber is meticulously stacked on the mylar sheet according to the design specifications, ensuring alignment and consistency. The entire assembly is then subjected to the vacuum bagging process to ensure proper lamination, consolidation, and curing under controlled conditions.

Once the curing process is complete, post-processing is carried out on the cured part to refine the fuselage shape and achieve the desired surface finish. The final result is a completed fuselage, ready for further assembly and integration into the UAV's structural framework.

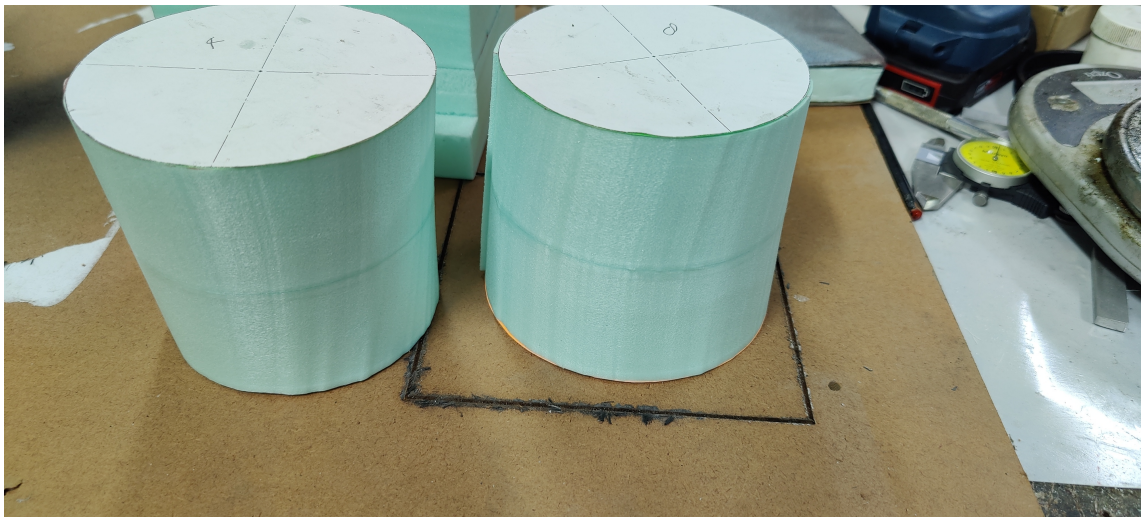

FIGURE 7.8: XPS core foam blocks

FIGURE 7.9: XPS Fuselage core

FIGURE 7.10: Fiber stacking over fuselage core

FIGURE 7.11: Vaccum bagging of fuselage

FIGURE 7.12: Post processing of the Fuselage

7.6 Manufacturing of Tail

Similar to the wing, the manufacturing of the tail parts also involves the use of a hot wire cutter to shape the airfoil and the core of the tail. Once the core is shaped, the stacking of layers is carried out using the same materials and thicknesses as in the wing construction. This is followed by the vacuum bagging process, which ensures proper lamination and curing. The result is a finished tail part, ready for assembly.

7.7 Manufacturing and Assembly of 3D-Printed Parts

Our UAV incorporates several 3D-printed components, primarily made from PLA (Polylactic Acid) material due to its lightweight and durable properties. These parts include the tail and wing components, GPS mount, antenna mount, and the Pixhawk mount box embedded within the fuselage.

The tail and wing parts are printed to precise aerodynamic profiles, ensuring they are both lightweight and structurally sound. The 3D printing process allows for the creation of complex geometries that enhance the UAV's flight performance.

The GPS and antenna mounts are designed to securely house navigational equipment while minimizing weight, ensuring they do not disrupt the UAV's center of gravity. Their accurate design contributes to the overall balance and stability of the aircraft.

The Pixhawk mount box, embedded within the fuselage, is crafted to securely hold the flight controller and associated electronics. The precision offered by 3D printing ensures a snug fit, protecting these critical components from vibrations and external forces.

After printing, the parts undergo light post-processing, such as sanding or coating, before assembly. The modular design of these 3D-printed components allows for straightforward assembly using screws, adhesives, or snap-fit mechanisms, as well as easy replacement or upgrades, enhancing the UAV's maintainability.

In summary, the use of 3D printing in our UAV's construction enables rapid prototyping, precise manufacturing, and the flexibility to meet specific design requirements, all of which contribute to the UAV's overall performance and adaptability.

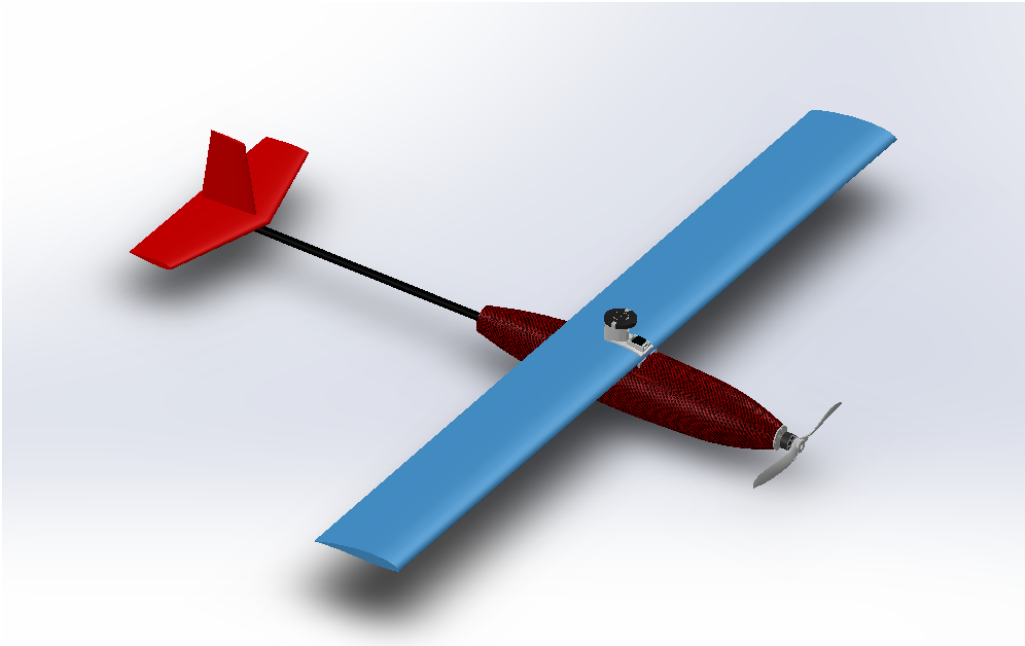

FIGURE 7.13: Final CAD Assembly

FIGURE 7.14: Complete UAV Ready to fly 1

FIGURE 7.15: Complete UAV Ready to fly 2

Chapter 8

Testing, Electronic Component Integration, and Flight Stack Modification

8.1 Electronics Assembly

The electronic assembly of our UAV is a critical phase in its construction, involving the precise integration of various systems that enable stable flight, accurate navigation, and effective communication. This process requires meticulous attention to detail, ensuring that each component is properly installed, connected, and tested to work harmoniously within the UAV's overall architecture.Components were strategically positioned to minimize interference and optimize functionality, guided by a combination of practical intuition and community-recommended best practices. This approach ensures that the electronic systems work harmoniously within the UAV, allowing it to meet its operational requirements effectively.

8.2 Overview of Electronic components

The electronic system of our fixed-wing UAV is designed for precision and reliability in flight control, propulsion, and communication. Central to this system is the Pixhawk flight

controller, responsible for processing sensor data and executing commands to maintain the UAV's stability and control.

The control surfaces, including the ailerons, elevator, and rudder, are actuated by durable and precise metal gear servos. Propulsion is provided by an AT2826 brushless DC motor, controlled by an AT 75 electronic speed controller (ESC), which also supplies a 5-volt output to the Pixhawk's servo rail.

To ensure reliable power distribution, a power module is used between the MaxAmps 11000mAh 4-cell battery and the ESC, powering the Pixhawk and other critical electronics.

The UAV features a Metek MS4525DO Airspeed sensor for accurate airspeed measurement, crucial for maintaining flight stability. Additionally, the Pixhawk is configured to autonomously detect a drop from a balloon and guide the UAV back to its home location, ensuring safe recovery.

The HerePro GPS module enhances the UAV's navigation capabilities, providing RTK (Real-Time Kinematic) positioning with a range of up to 40 km in line of sight (LOS). Communication with the ground control station (GCS) is facilitated by the RFD 868 telemetry system, operating on the MavLink protocol, ensuring robust and reliable data transmission during missions.

8.3 Mission Planning and Flight Testing

Due to regulatory and logistical constraints, we initially faced challenges in testing our UAV using a balloon launch system. As a result, we began our testing process using a Hexacopter with a 10 kg payload capacity. This Hexacopter, assembled using an off-the-shelf EFT Hexacopter frame and propulsion system, provided us with a reliable test bed for evaluating our firmware and UAV capabilities.

We planned and executed multiple missions using a Dapron fixed-wing plane to validate our firmware and to preliminarily assess the Hexacopter's ability to lift our UAV to the required altitude.

Subsequently, we conducted a mission with our fixed-wing UAV designed for real-world applications. Unfortunately, the initial test was not successful. After performing a thorough root cause analysis, we identified the need to enlarge our control surfaces. Following this modification, our UAV successfully completed the mission.

8.3.1 Initial Setup in Software in the Loop (SITL) and Hardware in the Loop (HITL)

Initially, using the custom development support of the PX4 flight stack, we built a version of the PX4 firmware capable of detecting a launch event as soon as the UAV is released from a hexacopter or balloon. Upon detecting this launch or release, the modified firmware is designed to autonomously navigate the UAV to its designated home location.

To optimize our development process and conserve resources, we initially conducted tests within Gazebo, a 3D dynamic simulator that allows for efficient UAV testing in a virtual environment. Gazebo is particularly advantageous because it closely adheres to real-world physics and provides a variety of sensors and interfaces for both user interaction and programmatic control.

In Gazebo, we created and customized the simulation environment to reflect the standard atmospheric conditions that our UAV would encounter during its actual operation. This simulation setup enabled us to fine-tune the PX4 flight stack by adding additional flight modes tailored for launch/release detection, followed by the triggering of the Return to Launch (RTL) mode.

The initial testing phase involved Software in the Loop (SITL) simulations, where both the PX4 flight stack and Gazebo ran on the same computer. This allowed us to rigorously test and validate the launch detection and RTL features in a controlled, simulated environment, ensuring that the UAV responded correctly to the launch and executed the return to home sequence as intended.

Following the successful SITL tests, we proceeded to Hardware in the Loop (HITL) testing. In HITL, the PX4 flight stack ran on the actual flight hardware, while Gazebo continued to simulate the flight environment. This step was crucial in verifying that the UAV's onboard systems interacted properly with the firmware, ensuring reliable performance during the real-world deployment.

By progressing through these stages, from SITL to HITL, we were able to confidently move towards the final field tests with a well-tuned and robust UAV flight control system, ready for its intended mission profile.

We also developed a custom mode within the PX4 flight stack that activates as soon as the flight controller detects a freefall, significant acceleration, or a timer-based free fall. This mode is crucial for ensuring that the UAV correctly identifies the moment of release,

whether it's from a hexacopter or a balloon. Upon activation, the mode triggers the necessary flight actions, such as initiating the Return to Launch (RTL) sequence, thereby allowing the UAV to autonomously navigate back to its home location.

8.3.2 Initial Bench Testing and Basic Air Testing

During this phase, we focused on validating that the Return to Launch (RTL) mode was correctly triggered as soon as the UAV detected a free fall. Additionally, we verified that all subsystems were functioning as required.

In the initial flight test, the UAV was flown in stabilized mode to assess its basic stability and response. This allowed us to perform preliminary PID tuning to ensure the aircraft could maintain controlled flight. Once we confirmed that the plane was sufficiently stable, we initiated the PX4's Autotune functionality. This process automatically fine-tuned the UAV's control parameters, optimizing its stability and performance.

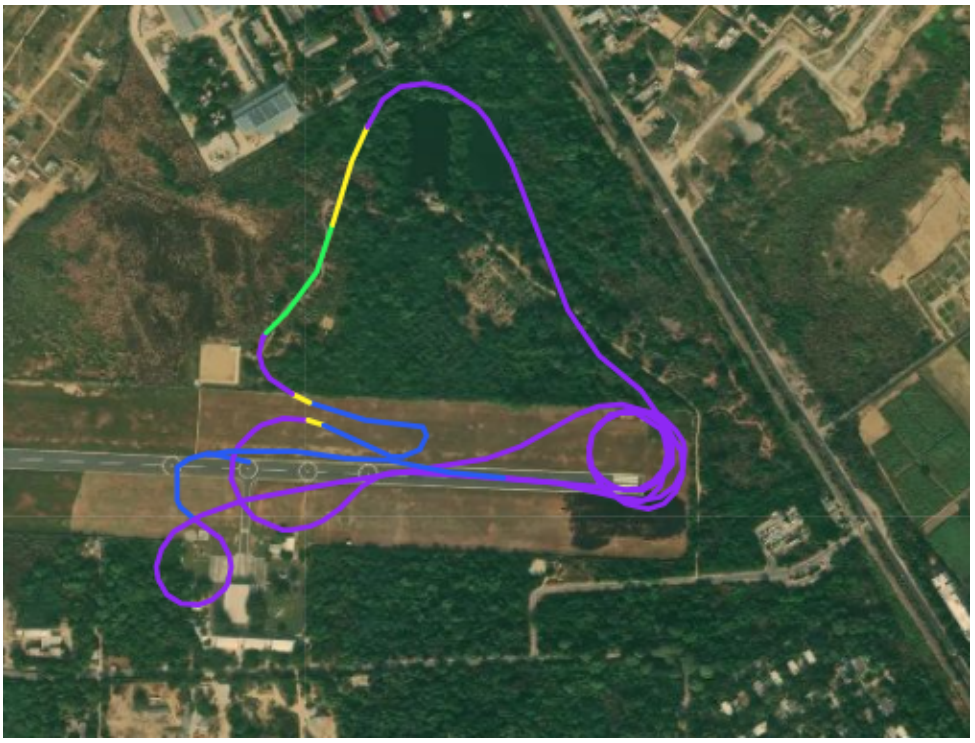

FIGURE 8.1: First flight route

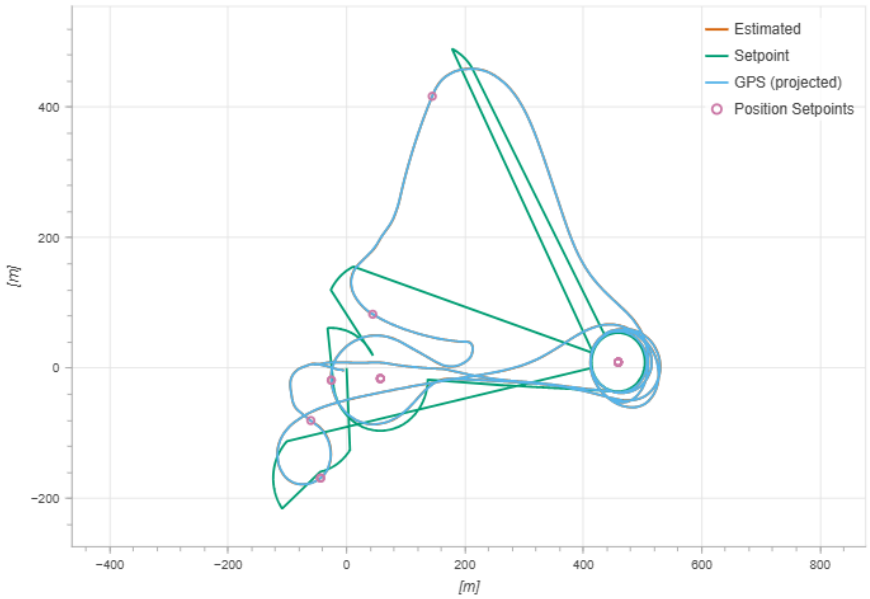

FIGURE 8.2: Lateral and longitudinal distances

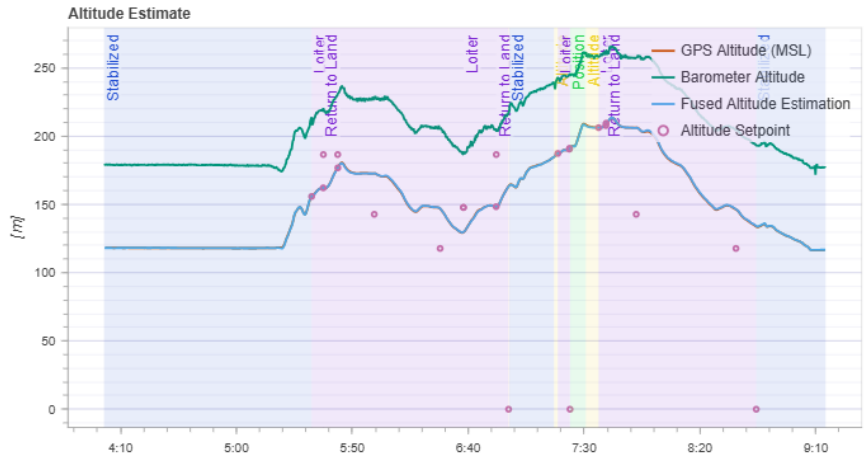

FIGURE 8.3: Altitude Estimate's

To safely test the in-flight code trigger, we initially used a relatively inexpensive Depron plane on the IITK airstrip. The purpose of this test was to ensure that the code executed as expected under real-world conditions. The test was successful, with the code triggering precisely as anticipated, confirming the effectiveness of our system.

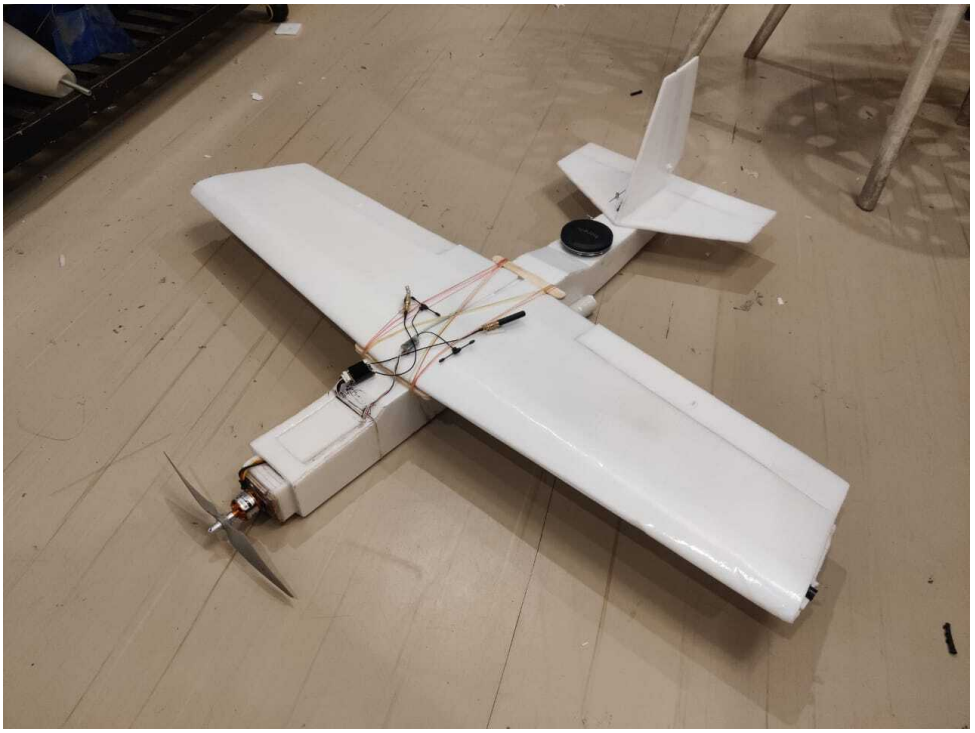

FIGURE 8.4: Dapron plane used for Firmware testing

FIGURE 8.5: Dapron plane flight route

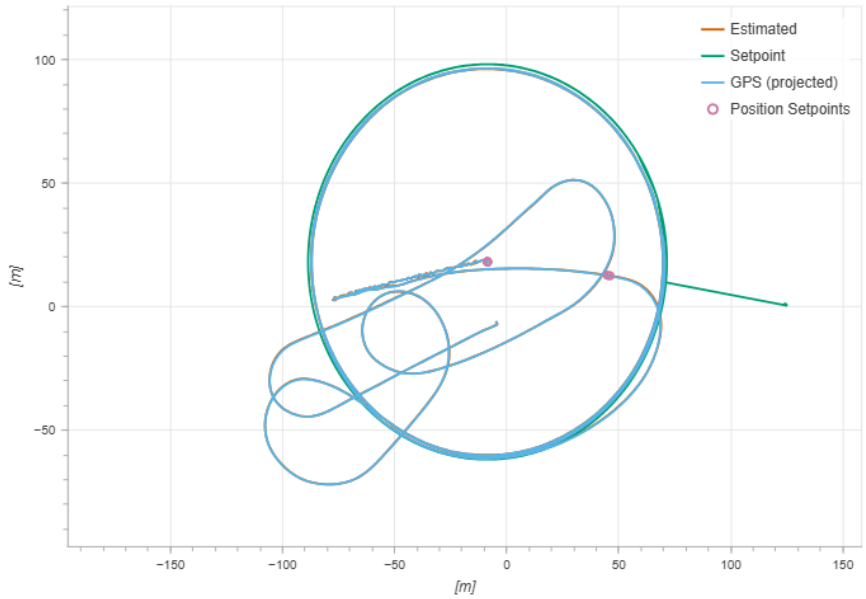

FIGURE 8.6: Lateral and longitudinal distances

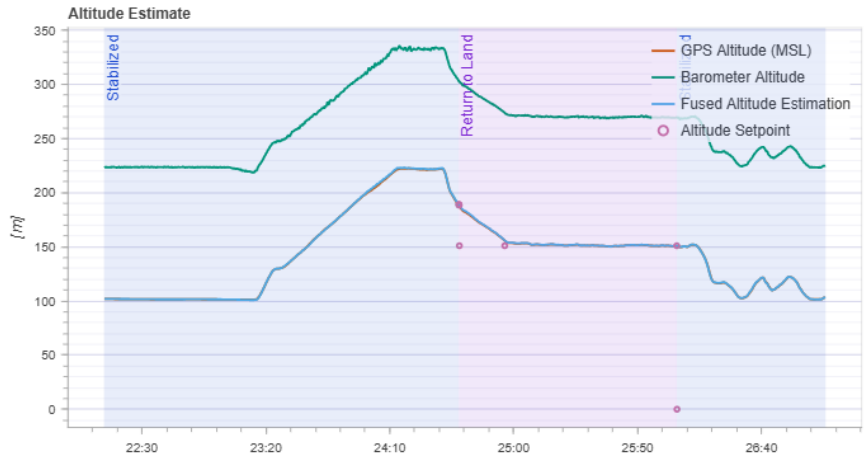

FIGURE 8.7: Altitude Estimate's

8.3.3 Final flight testing from lower altitude

Due to DGCA restrictions on Beyond Visual Line of Sight (BVLOS) operations, we were unable to test our system at the desired altitude and range. Despite these limitations, we conducted a test with our larger UAV by using a hexacopter to ascend it to a suitable altitude. Once the UAV was released from the hexacopter, it successfully detected the release, and the Return to Launch (RTL) mode was triggered as planned. The UAV

navigated back to the overhead position, entered a loitering pattern, and was subsequently landed manually without any issues.

FIGURE 8.8: Final testing setup with Hexacopter

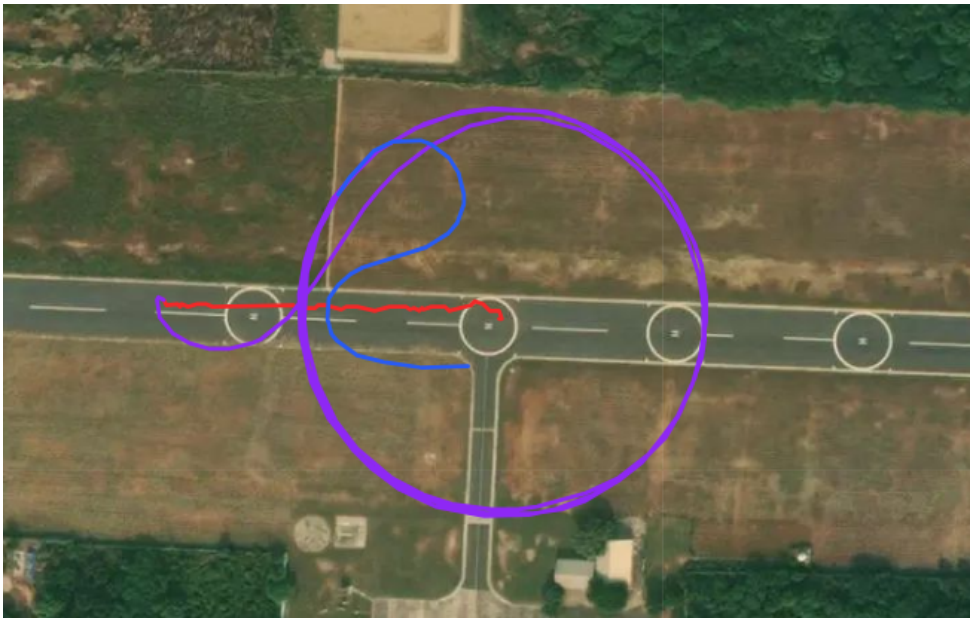

FIGURE 8.9: Flight route over IITK Airstrip

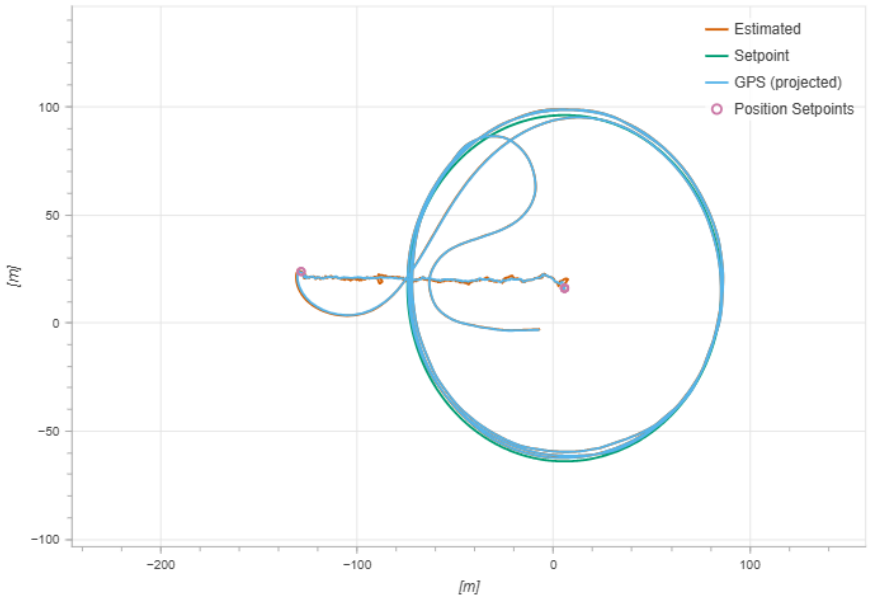

FIGURE 8.10: Lateral and longitudinal distances

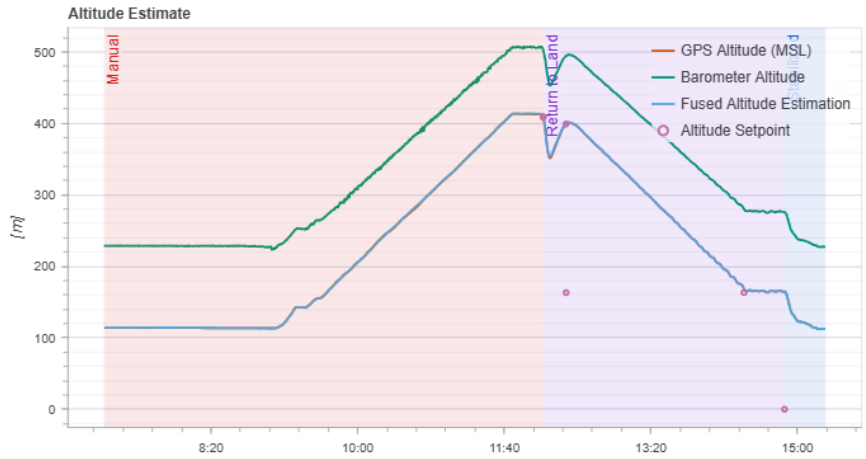

FIGURE 8.11: Altitude Estimate's

TABLE 8.1: Final flight performance parameters

Max Altitude Difference	302 m
Max horizontal speed	23 m/s
Total distance covered	2.35 Km
Maximum ROC	5.6 m/s
Maximum Descent Speed	18.9 m/s

Chapter 9

Conclusions and future work

9.1 Conclusion

This research presents a proof-of-concept for a high-altitude balloon-launched UAV capable of autonomous navigation, sensor retrieval, and stable operation in challenging conditions typical of the Indian subcontinent. A key achievement of the project was developing an effective launch-detection capability, enabling the UAV to identify balloon release and autonomously navigate to a designated home position. Once there, the UAV could loiter above, preparing for a controlled descent. The success of this navigation system, paired with the vehicle's lightweight construction at just 3.2 kg, represents a significant milestone, particularly as reduced weight supports energy efficiency and ease of launch with smaller balloons, addressing weight constraints for high-altitude missions.

Despite these successes, the project encountered regulatory challenges from the Directorate General of Civil Aviation (DGCA), which restricted high-altitude tests, necessitating alternative testing methods. Lower-altitude trials, using hexacopter drops, were designed to simulate high-altitude conditions. These simulations, conducted in real-world environments, confirmed the UAV's performance and mission capabilities, though limitations on altitude prevented full-scale high-altitude trials.

Overall, this UAV platform offers a promising solution for high-altitude data retrieval, aerosol sampling, and meteorological model validation, proving both cost-effective and adaptable for scalable, real-world applications.

9.2 Future Scope

As a proof-of-concept, the UAV presents opportunities for refinement and optimization across several domains:

1. **Enhanced Communication Systems**: Redundant communication links can be implemented to ensure consistent connectivity and control, particularly valuable in high-altitude missions where interference and link stability become challenges. Adding communication frequencies and protocols to the existing setup would enhance reliability.

2. **Thermal Management**: Extreme high-altitude conditions require improved thermal management for onboard electronics, especially batteries and avionics. Future models could integrate advanced thermal control systems to maintain optimal operating temperatures, which will enhance component reliability and increase mission duration.

3. **Testing and Prevention Systems**: Testing each subsystem rigorously, including propulsion, navigation, and control under varied conditions, is essential. Incorporating a prevention mechanism, such as drogue chutes to counter flat-spin tendencies, could improve control upon release, which is especially important for safe descent in turbulent weather.

4. **Scalability and Adaptability**: The UAV's adaptable design lends itself well to scaling for multiple high-altitude applications. Future iterations could be tailored for different meteorological or environmental research areas, such as aerosol sampling or validation of Weather Research and Forecasting (WRF) models. This adaptability allows the UAV to address diverse research needs in atmospheric sciences.

5. **Improved Payload Capacity**: Enhancing payload flexibility could make the UAV suitable for more extensive sensor suites, expanding its capability to capture additional data relevant to atmospheric studies. Future designs could balance payload capacity with energy efficiency, maintaining a lightweight structure while accommodating advanced sensors.

In conclusion, the current UAV system establishes a foundation for versatile high-altitude missions with significant potential to serve the evolving needs of meteorological and environmental research. With targeted refinements in communication, thermal management,

and scalability, this platform could become an essential tool for efficient, cost-effective atmospheric data retrieval in a wide range of global applications.

Bibliography

[1] J. J. Joseph, R. Meenal, F. T. Josh, P. A. Michael, V. K. Krishnamoorthy, G. Chandran, and S. Veerabathran, "Weather observation and forecasting using radiosonde," *Telkomnika (Telecommunication Computing Electronics and Control)*, vol. 20, no. 6, pp. 1376–1383, 2022.

[2] C. A. Wolf, R. P. Hardis, S. D. Woodrum, R. S. Galan, H. S. Wichelt, M. C. Metzger, N. Bezzo, G. C. Lewin, and S. F. de Wekker, "Wind data collection techniques on a multi-rotor platform," in *2017 Systems and Information Engineering Design Symposium (SIEDS)*, pp. 32–37, IEEE, 2017.

[3] M. V. Ratnam, N. Pravallika, S. R. Babu, G. Basha, M. Pramitha, and B. K. Murthy, "Assessment of gps radiosonde descent data," *Atmos. Meas. Tech.*, vol. 7, pp. 1011–1025, 2014.

[4] V. Rastinasab and H. Weidong, "Modeling of the meteorological balloon-cube with lora-based ground station," *Journal of Engineering Sciences*, 2020.

[5] P.-Y. Liu, Y.-W. Huang, C. Kuo, and Y.-H. Chou, "The effective retrieval of the sounding balloon combined with unmanned aerial vehicle," in *2015 IEEE International Conference on Systems, Man, and Cybernetics*, pp. 26–31, IEEE, 2015.

[6] S. Lateran, M. Sedan, A. Harithuddin, and S. Azrad, "Development of unmanned aerial vehicle (uav) based high altitude balloon (hab) platform for active aerosol sampling," in *IOP conference series: materials science and engineering*, vol. 152, p. 012018, IOP Publishing, 2016.

[7] T. J. Schuyler, S. I. Gohari, G. Pundsack, D. Berchoff, and M. I. Guzman, "Using a balloon-launched unmanned glider to validate real-time wrf modeling," *Sensors*, vol. 19, no. 8, p. 1914, 2019.

[8] N. Jones, "High-altitude balloons: A scientists' guide to what's up there and why," Feb 2023.

[9] N. US Department of Commerce, "Collecting meteorological data by radiosonde or weather balloon," 2023. `https://www.weather.gov/rah/virtualtourballoon`, (accessed Febeuary, 2023).

[10] G. Dobson and A. Brewer, "Meteorology and high altitude aviation," *The Aeronautical Journal*, vol. 50, no. 430, pp. 787–810, 1946.

[11] F. A. d'Oliveira, F. C. L. d. Melo, and T. C. Devezas, "High-altitude platforms—present situation and technology trends," *Journal of Aerospace Technology and Management*, vol. 8, no. 3, pp. 249–262, 2016.

[12] D. Zhou, S. Gao, R. Liu, F. Gao, and M. Guizani, "Overview of development and regulatory aspects of high altitude platform system," *Intelligent and converged networks*, vol. 1, no. 1, pp. 58–78, 2020.

[13] W. Smith, U. Bhattarai, D. C. Bingaman, J. L. Mace, and C. V. Rice, "Review of possible very high-altitude platforms for stratospheric aerosol injection," *Environmental Research Communications*, vol. 4, no. 3, p. 031002, 2022.

[14] J. Pelton, "High altitude platform systems (haps) and unmanned aerial vehicles (uav) as an alternative to small satellites," *Handbook of Small Satellites: Technology, Design, Manufacture, Applications, Economics and Regulation*, pp. 1–16, 2020.

[15] S.-I. Higashino, M. Hayashi, S. Nagasaki, S. Umemoto, and M. Nishimura, "A balloon-assisted gliding uav for aerosol observation in antarctica," *Transactions of The Japan Society for Aeronautical and Space Sciences, Aerospace Technology Japan*, vol. 12, no. APISAT-2013, pp. a35–a41, 2014.

[16] M. Schwarzbach, S. Wlach, and M. Laiacker, "Modifying a scientific flight control system for balloon launched uav missions," in *2015 IEEE Aerospace Conference*, pp. 1–10, IEEE, 2015.

[17] J.-C. Lede', R. Parks, and M. Croom, "High altitude drop testing in mars relevant conditions for the ares mars scout mission," in *2nd AIAA" Unmanned Unlimited" Conf. and Workshop & Exhibit*, p. 6609, 2003.

[18] D. Steenari, T. Kuhn, and S. Wlach, "Vexredus: A student high altitude glider project to demonstrate the capabilities of a blended wing body concept," in *Proceedings of*

21st ESA symposium on European rocket & balloon programmes and related research, pp. 225–232, 2013.

[19] D. Raymer, "Aircraft design: A conceptual approach sixth edition," *Aircr. Des. A Concept. Approach, Sixth Ed*, 2018.

[20] M. H. Sadraey, *Design of Unmanned Aerial Systems.* John Wiley & Sons, 2020.

[21] UAVOS and Stratodynamics Inc., "Stratospheric hidron uav," 2019. Accessed: 2024-06-08.

[22] M. Laiacker, S. Wlach, and M. Schwarzbach, "Dlr high altitude balloon launched experimental glider (hableg): system design, control and flight data analysis," in *2015 Workshop on Research, Education and Development of Unmanned Aerial Systems (RED-UAS)*, pp. 360–368, IEEE, 2015.

[23] M. H. Sadraey, *Aircraft design: A systems engineering approach.* John Wiley & Sons, 2012.

[24] O. Schrenk, "A simple approximation method for obtaining the spanwise lift distribution," *The Aeronautical Journal*, vol. 45, no. 370, pp. 331–336, 1941.

[25] I. K. Kapoulas, J. Statharas, A. Hatziefremidis, and A. Baldoukas, "Fast airfoil selection methodology for small unmanned aerial vehicles," *Applied Sciences*, vol. 12, no. 18, p. 9328, 2022.

[26] C. Putra, R. Julistina, M. A. Moelyadi, and T. Mulyanto, "Comparative study between schrenk and cfd analysis for predicting lift distribution along wing span of glider aircraft," *Aerospace Science and 'Technofogy in Indonesia*, 2016.

[27] A. R. Soemaryanto and N. H. Rosid, "Verification of schrenk method for wing loading analysis of small unmanned aircraft using navierstokes based cfd simulation," *Jurnal Teknologi Dirgantara*, vol. 15, no. 2, pp. 161–166, 2018.

[28] N. N. M. Kamal, A. A. Basri, E. I. Basri, I. S. Basri, and M. F. Abas, "Comparison study between schrenk's approximation method and computational fluid dynamics of aerodynamic loading on uav naca 4415 wing," *Journal of Advanced Research in Fluid Mechanics and Thermal Sciences*, vol. 64, no. 2, pp. 283–292, 2019.

[29] J. Winslow, V. Hrishikeshavan, and I. Chopra, "Design methodology for small-scale unmanned quadrotors," *Journal of Aircraft*, vol. 55, no. 3, pp. 1062–1070, 2018.

[30] A. M. Harrington and C. Kroninger, "Characterization of small dc brushed and brushless motors," *ARMY RESEARCH LAB ABERDEEN PROVING GROUND MD VEHICLE TECHNOLOGY DIRECTORATE, Tech. Rep*, 2013.

[31] N. K. Hieu and H. T. Loc, "Airfoil selection for fixed wing of small unmanned aerial vehicles," in *AETA 2015: Recent Advances in Electrical Engineering and Related Sciences*, pp. 881–890, Springer, 2016.